AIAA SciTech Forum
12-16 January 2026, Orlando, FL
AIAA SCITECH 2026 Forum

10.2514/6.2026-1102

Recent Advances in Particle Image Velocimetry for Aerospace Science

Markus Raffel*
Institute of Aerodynamics and Flow Technology, German Aerospace Center, Göttingen

Steven J. Beresh†
Sandia National Laboratories, Albuquerque, New Mexico, U.S.A.

Jenna Eppink ‡
NASA Langley Research Center, Hampton, VA 23681, USA

Fulvio Scarano§
Delft University, The Netherlands

Daniel Schanz¶ and Andreas Schröder‖
Institute of Aerodynamics and Flow Technology, German Aerospace Center, Göttingen

Christian E. Willert**
DLR Institute of Propulsion Technology, German Aerospace Center, Cologne

Recent advances in particle image velocimetry (PIV) have taken it far beyond its original role as a two-dimensional velocity measurement technique. The combination of improved hardware, algorithmic innovations and interdisciplinary synergies positions PIV as a highly flexible and powerful tool supporting modern aerospace science applications. In this article, important current developments will be presented in detail to demonstrate their capabilities for volumetric measurement, time-resolved data sequences, large-scale applications, Lagrangian particle tracking, overcoming optical access restrictions, incorporation of machine-learning technologies, and adoption of emerging camera technologies.

I. Introduction

The quantitative measurement of flow fields continues to be a central challenge in experimental fluid mechanics. Among the various optical measurement techniques, particle image velocimetry (PIV) has established itself as the standard method since the mid-1980s. It enables the simultaneous, areal determination of velocity fields with high spatial and temporal resolution. PIV is characterized by the fact that no probes need to be inserted into the flow field: The flow is simply marked by seeding particles, whose movement serves as a tracer for the local fluid velocity. Using short (usually laser) light pulses and high-resolution, fast digital cameras, sequences of particle images can be captured and analyzed using correlation methods or particle tracking methods, for example, in order to reconstruct velocity (and acceleration) vector fields.

Although the basic principle has remained unchanged for decades, the performance of the method has increased considerably in recent years. This is due in particular to advances in three areas:

- optical systems for illuminating particles, including high-repetition-rate lasers and large-scale illumination
- image acquisition technology, in particular digital CMOS cameras and affordable high-speed cameras
- the combination of digital image processing and numerical flow simulation techniques.

*Head of Department, German Aerospace Center, Göttingen, and Professor, Leibniz University Hannover, Germany, AIAA Associate Fellow, correspondence to Markus.Raffel@dlr.de
†Distinguished Member of the Technical Staff, Engineering Sciences Center, AIAA Fellow.
‡Research Aerospace Engineer, Flow Physics and Control Branch, M.S 170, AIAA Senior Member
§Professor, Delft University, The Netherlands
¶Research Scientist, German Aerospace Center, Göttingen, Germany
‖Research Scientist, German Aerospace Center, Göttingen and Chair of Image Based Measurement Techniques, BTU, Cottbus, Germany
**Research Scientist, German Aerospace Center, Göttingen, Cologne

Modern high-speed cameras enable frame rates in the kilohertz to megahertz range, which allows time-resolved investigation of even very dynamic flow processes. In parallel, developments in light emitting diodes (LEDs) and in laser technology - in particular compact, diode-pumped Nd:YAG and fiber laser systems - have improved energy efficiency and repetition rates. Using a combination of large-scale LED arrays and light-scattering efficient helium-filled soap bubbles (HFSB), it is now also possible to perform particle velocimetry in large volumes, provided the shear forces in the flow are adequately captured by the larger seeding particles. This has opened PIV into new aerodynamic applications in large-scale wind tunnels and even outdoor testing, directly measuring aerodynamic performance of entire bodies rather than measuring sub-scale canonical fluid dynamics. The use of redundant illumination and imagers in the form of clusters or antennae, as well as the calibration between them, allow an unoccluded 3D measurement surrounding complex test objects that are not otherwise amenable to visualization.

At the algorithmic level, significant progress has been made in correlation and reconstruction methods. For example the integration of fluid mechanical equations (e.g. Euler and Navier-Stokes equations) considerably increase the accuracy of the vector fields by iteratively adjusting local displacements to match physically realistic motion. Access to fully three-dimensional velocity data was made possible by tomographic PIV (tomo-PIV) after a seminal paper by Elsinga et al. [1] by making use of multi-camera imaging and volumetric reconstruction methods. More recently, the “Shake-the-Box" (STB) method [2] has established itself offering unprecedented spatial resolution and accuracy in three dimensions. The concepts of Physics Informed Neural Networks (PINNs) applied to tracking data broaden the physical parameters that can be extracted from the measurements. Early applications served fundamental research for fluid dynamics, but in combination with previously mentioned technologies (e.g. helium-filled soap bubbles) have seen application to aerodynamic flows as well.

Time-resolved particle image velocimetry allows the investigation of transient and turbulent flow phenomena, providing new insights into coherent structures, energy transfer mechanisms, and flow resonances. As new technologies have increased the framing rates that can be achieved, measurement of the time component has become successful in high-speed flows including supersonic and shock-driven regimes. This has migrated the technology into entirely new classes of aerospace applications, including external aerodynamics and high-speed propulsion.

The more general integration of data analysis methods based on artificial intelligence is becoming increasingly important. Neural networks and learning-based correlation methods show promising approaches for noise suppression, for filling gaps in incomplete vector fields and for increasing processing speed.

The miniaturization of optical components and unconventional recording concepts also open up new application possibilities in the field of transonic and supersonic flows, as well as for use in wind tunnels – or even turbomachinery rigs – with limited optical accessibility. Lensless PIV applies computational imaging methods to replace conventional lens systems, allowing for velocity measurements in close proximity to surfaces. The technique uses only a thin encoding mask to encode scene information, supporting the development of integrated sensor technologies.

The emerging imaging technology of event-based cameras has led to the development of event-based imaging velocimetry (EBIV). It has the potential to enable flow measurements at high temporal resolution and moderate hardware investment cost.

II. Recent developments in Lagrangian Particle Tracking

A. Introduction and overview

Dense 3D Particle Tracking allows characterizing unsteady and turbulent flows within the Lagrangian and Eulerian frame of reference at high spatial and temporal resolution. The 3D Lagrangian Particle Tracking (LPT) [3] method “Shake-The-Box” (STB) [2] has been continuously developed during the past decade and is able to reliably and efficiently extract particle trajectories at unprecedented numbers from few camera projections in volumetric flow measurements. STB delivers accurate data on particles position, velocity and acceleration (material derivative) along densely distributed tracks. The STB method can be applied as well to short recording sequences, acquired with a multi- or two-pulse technique, allowing investigating high-speed flows at Reynolds numbers relevant for research in aerospace engineering.

Based on large amounts of measured 3D Lagrangian trajectories in many time series highly resolved particle transport- and residence time investigations as well as one- and two particle dispersion statistics can be calculated inside the measurement volume. Furthermore, the temporally fitted particle trajectory data can be used for one- and multi-point statistics of velocity and acceleration in binning procedures delivering grid resolutions down to sub-pixel (typically µm) size. Using the particles’ velocity and acceleration information as input to data assimilation (DA) methods like FlowFit (FF3.0) or Physics Informed Neural Networks (PINN), interpolations of the time-resolved flow fields can be determined.

These deliver the 3D velocity gradient tensor and pressure data at high spatial resolution with minimized deviation to the measurement data, while simultaneously Navier-Stokes-constraints are enforced during the optimization process.

The recent developments have transformed 3D Lagrangian Particle Tracking from a tool to measure averaged (tracer) particle properties in small volumes (a few cubic centimeters) to a fully integrated environment, capable of delivering spatially highly resolved time-series within scalable volumes from a few cubic millimeters up to several cubic meters. The combination of advances both on the software side with the introduction of the Shake-The-Box (STB) method and efficient data assimilation (DA) techniques and the hardware side (high frequency pulsed- LED and laser-illumination, helium-filled soap bubbles (HFSB) seeding, light sensitive high-resolution-, event-based and high-speed cameras) enabled a rapid expanse in flow measurement capabilities within Lagrangian and Eulerian frames of reference and allow for corresponding investigations of (turbulent) flow and transport phenomena.

B. Principles of Lagrangian Particle Tracking

In contrast to the correlation-based ensemble approach of PIV, flow state information can also be gained by assessing the motion of single particles. Most flows of interest show distinct 3D characteristics leading to significant out-of-plane motion in typical light-sheet based PIV setups and therefore short residence times within the illuminated region. In PIV, the problem is mostly mitigated by applying double-frame processing (cross-correlation of image pairs). When tracking single particles, long trajectories are desired to decrease the measurement uncertainty and to gain access to temporal processes like particle dispersion. Due to this reason, the development of particle tracking methods has embraced volumetric approaches from early on ([4], [5]). Most of these 3D methods combine time-resolved multi-camera setups with volumetric illumination. While single-camera alternatives are available (see e.g. [6]), here we will focus on multi-camera techniques, which have seen a rapid development during the last decade. The principle working mechanism has not changed for many years after the pioneering works of Nishino and Maas: Apply a triangulation process [7], [8] to determine 3D positions of tracer particles from their projections on few cameras and connect the reconstructed point cloud for successive time-steps to yield particle trajectories. For an extensive overview, the reader is referred to [9]. Pure triangulation is sensitive to the occurrence of ambiguities (particles being reconstructed on false positions due to arbitrary intersection of line-of-sights from non-matching 2D particle peaks). This problem scales heavily with the number of imaged particles per sensor area, effectively limiting the usable particle image density N_I of early tracking approaches to low values $N_I < 0.01$ ppp ('particles-per-pixel'), which were typically insufficient to resolve instantaneous flow structures. Tomographic PIV [10][11] filled this void by replacing triangulation and temporal connection with a voxel-space reconstruction and subsequent 3D cross correlation. The iterative approach of the applied reconstruction schemes [12] [13] allowed tackling higher particle image densities ($N_I \approx 0.05$ ppp) and thus the visualization of flow structures (e.g. [14]) or even their temporal evolution (e.g. [15]). Tomographic PIV comes with a couple of downsides though. The cross-correlation introduces a spatial low-pass modulation of the velocity gradients, acceleration vector fields are not directly accessible, post-processing methods are limited and the demands on computational power and memory are significant. The transition of particle tracking methods toward high particle densities came with the introduction of iterative particle reconstruction (IPR) [16], [17] and finally the Shake-The-Box technique [18]. IPR constitutes an iterative approach to triangulation. It initially operates on the original camera images, while later iterations use residual images, which are created by subtracting back-projected synthetic images of already reconstructed particle positions.

Intermittently, the positions and intensities of reconstructed particles are optimized using an image matching technique (often referred to as 'shaking' the particles). This process decreases the intensity of ghost particles, most of which can then be discarded by applying an intensity threshold. This original concept allows reconstructing 3D positions from camera images with N_I comparable to Tomo-PIV [16].

By including a number of modifications in the process (e.g. ignoring the (locally) brightest camera, gradually increasing the allowed triangulation error and permutating the camera order upon triangulation), the process becomes more efficient and is able to handle synthetic images above $N_I = 0.1$ ppp [17].

When handling real experimental data, the imaging conditions are typically worse than in synthetic tests, as effects of directional scattering, non-Gaussian particle imaging, interference of the coherent light of close particles and many more can occur. These traits can lead to a significant reduction in reconstruction performance of single–time steps compared to synthetic data. However, additional information is available through the temporal evolution of the particle field, recorded at successive time steps. Each recording represents a slightly different view on the particle distribution, enabling the detection of previously hidden information.

The STB method [18] was designed for such time-resolved data. It not only integrates temporal information into the reconstruction process but also reverses the conventional logic: rather than reconstructing the particle position distribution independently at each time step and subsequently searching for matches with known tracks, the algorithm begins by initializing the current time step with predicted positions of all particles whose tracks are already identified. The predicted positions are then refined using the shaking process from IPR as a corrector scheme. After this step the already know particles are well located and their images can be removed from the original images by creating residual images. The remaining unknown particles are then reconstructed from these residual images, which are less populated and therefore pose a lighter reconstruction problem.

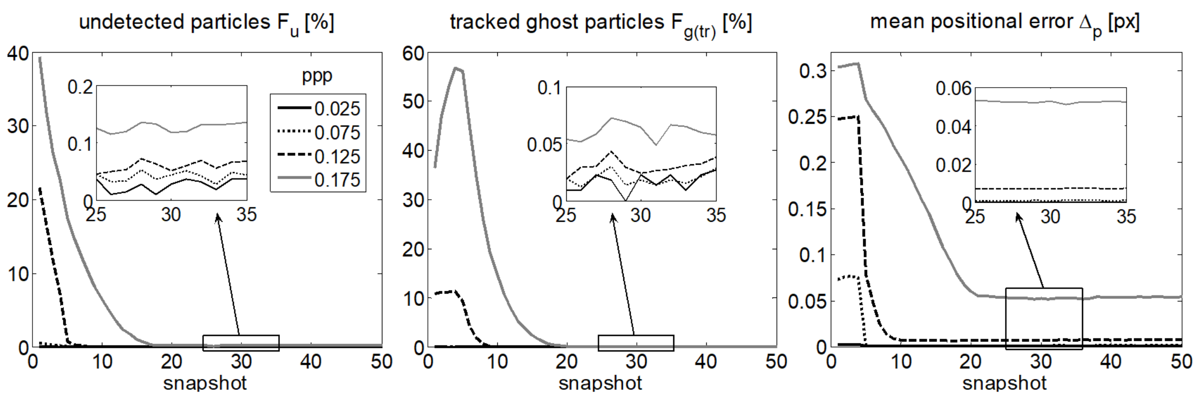

Fig. 1 Temporal development of undetected particles (left), ghosts within the tracked particles (middle) and averaged 3D positional error (right) for STB reconstructions at different particle image densities.

As the number of known particles increases, the formation of ghost particles is progressively reduced; specifically because ghost particles do not feature a long temporal consistency in contrast to true particles, which cannot disappear inside the measurement volume [19]. The algorithm naturally converges toward a self-stabilizing solution, in which primarily only particles entering the measurement domain still need to be identified. This significantly improves the effective seeding density while simultaneously lowering computational cost. Fig. 1 demonstrates the convergence to tracking nearly all particles on a time-series of 50 synthetic images with particles following a turbulent flow field. Even at very high particle image densities of 0.175 ppp, the algorithm converges in less than 20 time-steps to a state, where less than 0.2 % of the particles remain undetected and virtually no ghost particles occur. With the elimination of ghost particles, the position accuracy of the reconstructed particles increases significantly.

C. Application to experimental data

How the theoretical performance on synthetic transfers to experimental conditions is dependent on a number of conditions, as argued above. STB particle tracking at high particle image densities has been applied in a variety of experiments, ranging from investigations of thermal flows in air [20], [21] and water [22], impinging jets in air [23] and water [24], homogeneous turbulence [25], helicopter wakes [26] and turbulent boundary layers (TBL), investigating both the largest [27], as well as the smallest scales [28]. Seeding densities up to $N_I = 0.18$ ppp could be realized with good experimental conditions. A prominent example can be found in the 2020 Gallery of Fluid motion on the flow within a Rayleigh-Bénard convection cell [29]. The experiences gained through all these experiments show that combinations of tracer particles and illumination that avoid interference effects provide the best basis for high-quality reconstruction and tracking. In air, Helium-Filled Soap Bubbles (HFSB) [30, 31], illuminated by LEDs work very well and allow investigating large volumes due to scalability of LED panels. Up to 50 cubic meters of volume have been realized when investigating slow thermal flows that allow for long illumination times [32, 33].

Large-scale setups can also be applied to faster flows. HFSBs have been successfully tracked at up to 58 m/s in a large-scale experiment in the Cottbus large pipe facility, using overpulsed LED illumination [36] at up to 13 kHz. Fig. 2 shows results from an investigation of quadcopter wakes. Five high-speed cameras recorded hovering and flying drones in a volume of approx. 2 m^3. A two-stage scanning setup allows the simultaneous tracking of over 500,000 HFSB [34] with velocities up to around 15 m/s (at 3 kHz repetition rate). For better visibility, only fast bubbles (> 3 m/s) below the quadcopter are visualized. The wakes of the four rotors can be identified that, when impinging on the ground, merge into expanding circular structures. FlowFit3 data assimilation (see Sec. II.E) allows visualizing the individual vortex systems of each rotor and their interaction. For more details, the reader is referred to Wolf et al. [35].

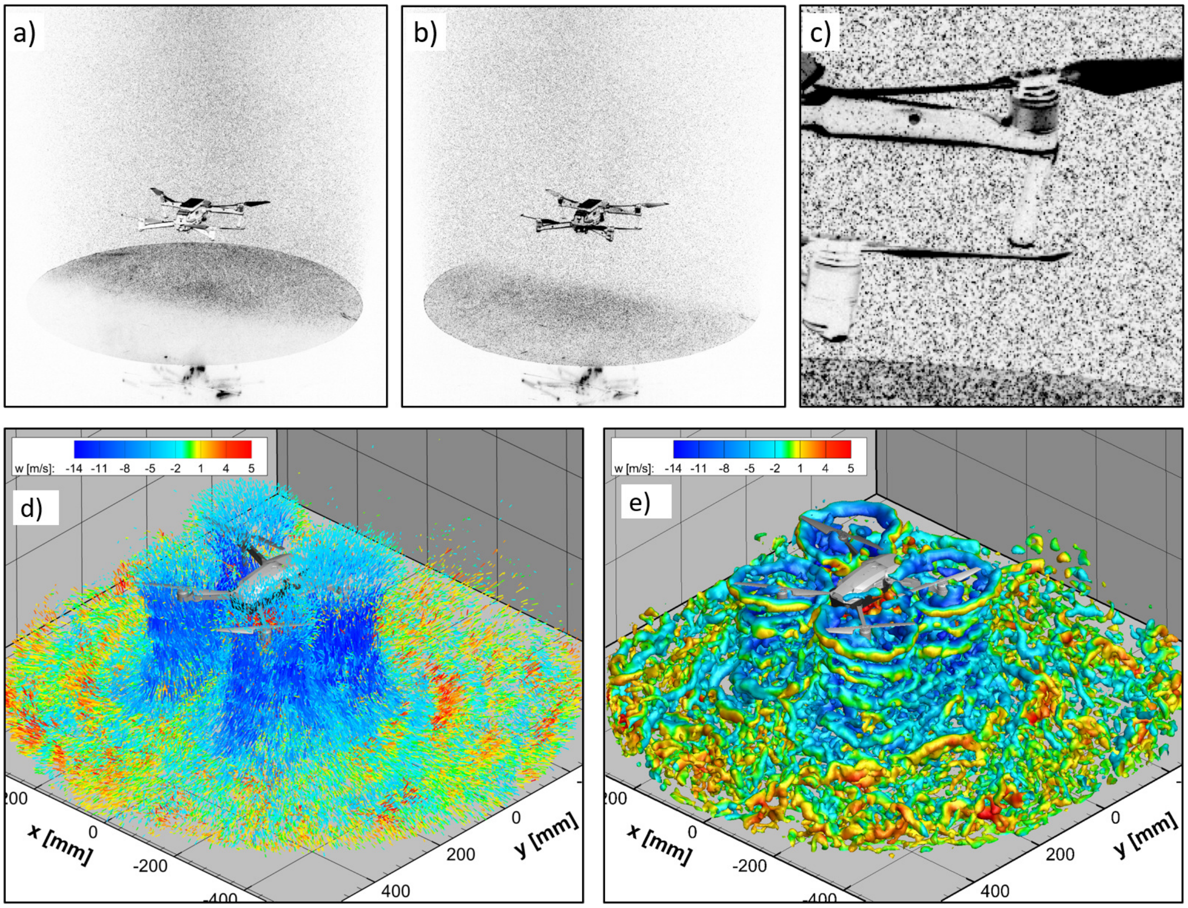

Fig. 2 Experimental investigation of hovering quadcopter in ground effect by scanning 3D-LPT of helium-filled soap bubbles. Two successive images from one out of five cameras with (a) illuminated back and (b) front part of the volume, as well as (c) a detail view on one of the rotors. (d) Combined tracking result of both sub-volumes, showing only particles with velocity larger than 3 m/s and (e) flow structures of the same instance, visualized as iso-surfaces of Q-criterion (Q = 20,000/s^2), gained from FlowFit3 data assimilation. For more information see [34, 35].

Typical wind-tunnel experiments with smaller areas of interest rely on oil-droplet seeding (like Di-Ethyl-Hexyl-Sebacat, DEHS) and illumination by a high speed laser. Though such setups typically offer more challenging imaging conditions, high-density particle can be reliably performed. Figure 3 demonstrates setup and results of a 3D measurement of the near-wall region of a TBL flow in air. Five Phantom V2640 high speed cameras image a volume of 60 x 12 x 2 mm^3 (streamwise x spanwise x wall-normal). By reducing the camera resolution to 2048 x 400 pixels, an acquisition frequency of 30 kHz can be applied over time-series of 115,000 images, allowing simultaneous tracking of approx. 45.000 particles at a free stream velocity of 15 m/s (Re_θ = 4160). Wall vibrations can be determined and corrected with an accuracy better than 1 μm using near-wall particles. Averaging the particle properties in thin (5 μm) wall-parallel bins gains high-resolution profiles of velocity and Reynolds stresses (Fig. 3 e). The gained particle tracks of one or several time-steps can be fed to flow-field reconstruction algorithms (see Sec. II.E). Fig. 3 f) shows a PINN result [37] of an event with high positive wall-shear stress, showing the streamwise velocity in a near-wall plane at y^+ = 3 together with a multitude of overlying flow structures, depicted as iso-surfaces of Q-criterion. Reconstructions with several algorithms applied to a comparable synthetic data-set can be found in Fig. 5.

In water-based experiments, tracer particles that closely match the density of the fluid are required. Plastic particles, e.g made from polyamide, which are available cheaply from color industry, have been used in large-scale water tunnels. An approximately spherical particle shape is desirable, as rotating particles might lead to varying particle image intensity, which can be detrimental to the tracking process. Very good results have been attained using spherical fluorescent

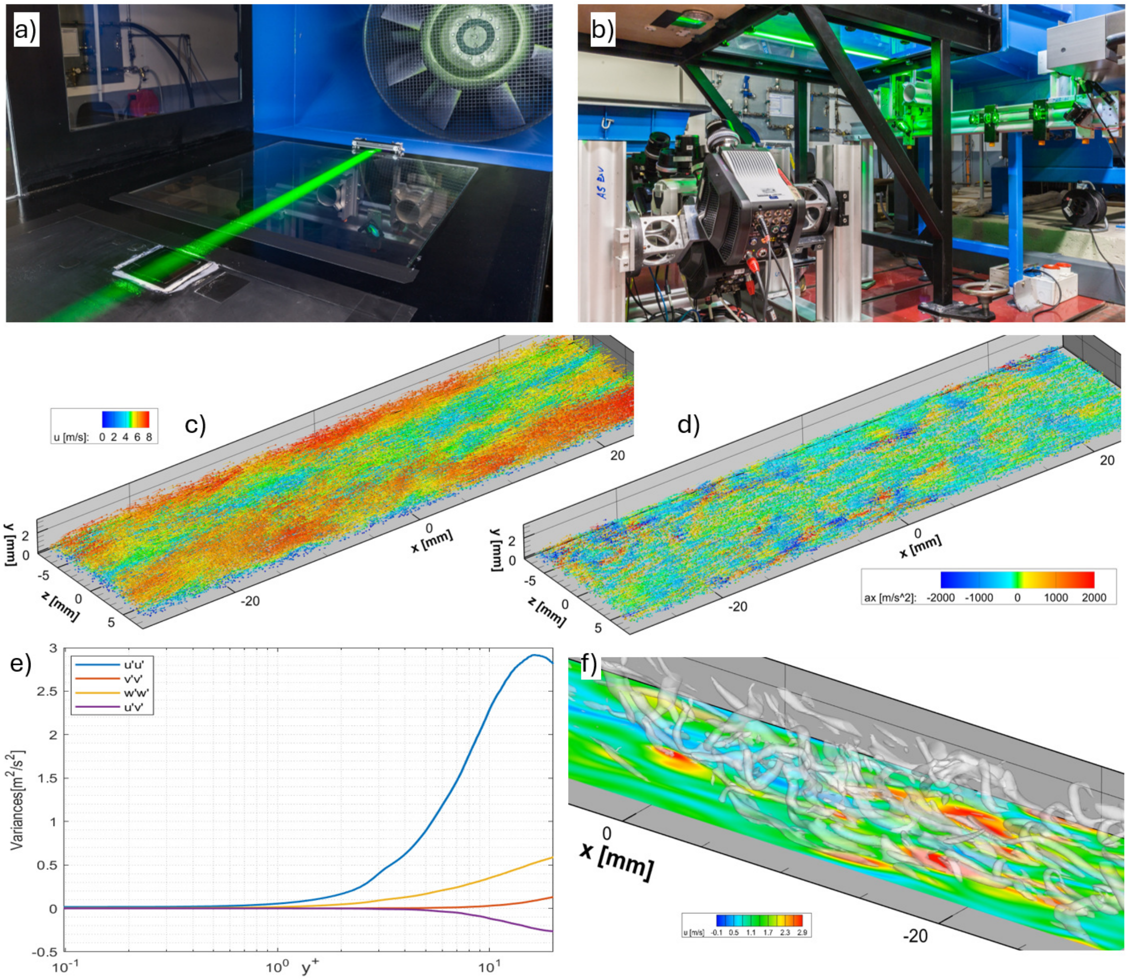

Fig. 3 Experimental setup of near-wall TBL experiment at DLR Göttingen. (a) Laser-illuminated RoI above window in wind-tunnel wall. (b) System of five high-speed cameras viewing the RoI from below. (c) and (d) instantaneous 3D particle with velocity vector colored by streamwise velocity and streamwise acceleration. (e) Profiles of Reynolds stresses gained by bin-averaging. (f) Instantaneous event of high wall-shear stress; 3D velocity field reconstructed by PINN.

particles with the additional benefit that by filtering the exciting light, background intensity can be completely eliminated [22, 38].

D. LPT in high-speed flows

As seen above, high-speed cameras and illumination can nowadays capture flows at several tens of meters per second and are therefore applicable in low speed wind tunnels. However if faster flows are to be investigated or if high camera resolution in combination with a fast repetition rate is required, other approaches have to be pursued.

1. Two-pulse LPT

To tackle such problems, double-frame cameras with very short inter-framing times have been employed in PIV applications for decades [39]. Leveraging this hardware, several approaches of integrating 3D reconstruction and a tracking step for double-pulse measurements have been developed over the last years. Tomographic reconstruction with peak identification [40, 41] or IPR [42] are used to deduce 3D particle locations. The track connection between the gained particle clouds is typically performed using iterative approaches with neighborhood criteria. Even such basic two-pulse tracking approaches can yield data that rivals tomographic PIV in terms of spatial resolution, especially when coupled with data assimilation techniques involving physics constraints [42]. Some features of particle tracking are retained, e.g. in regions with strong shear rates (like close to walls or model surfaces) the smoothing effects of correlation based methods [43] can be avoided using bin averaging techniques [44, 45].

2. Multi-pulse LPT

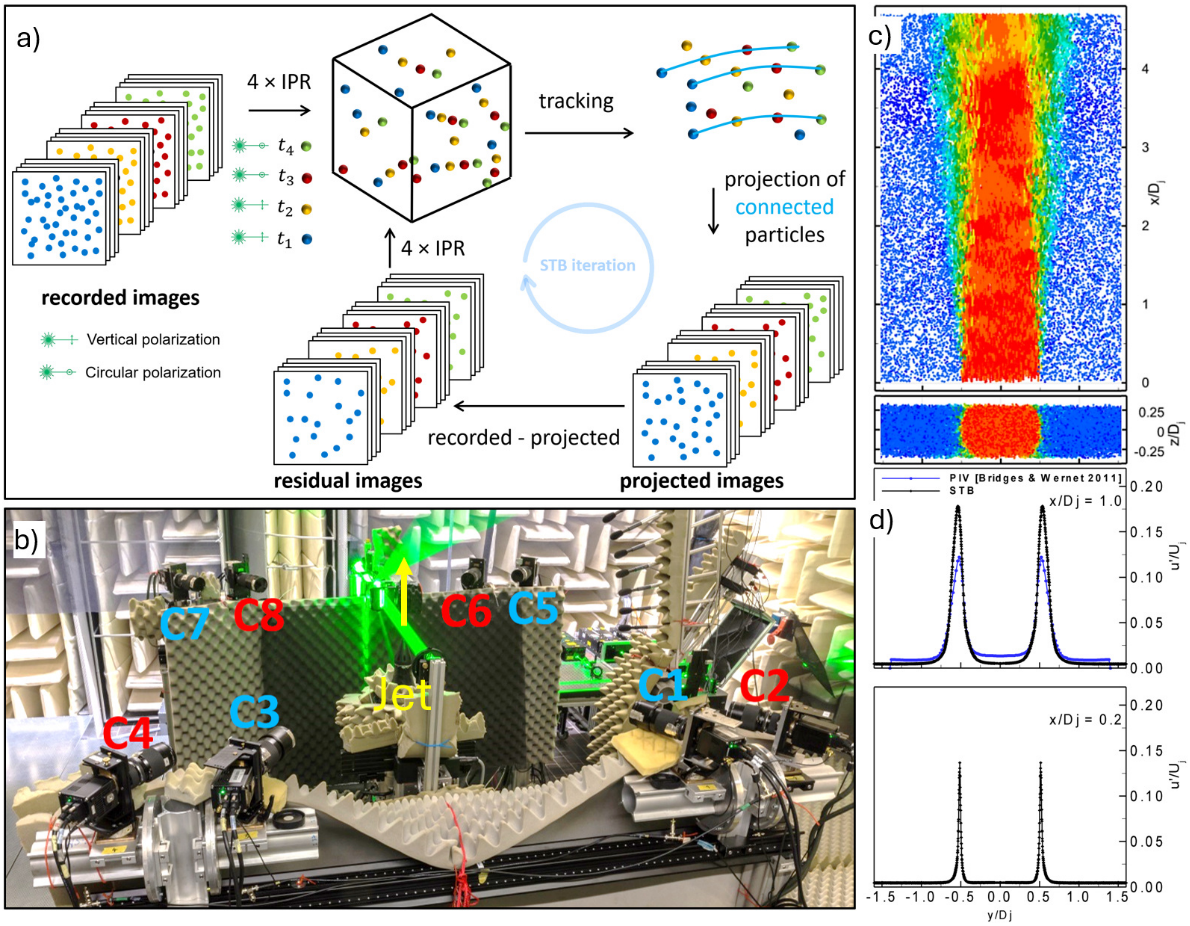

Fig. 4 (a) Scheme of Four-Pulse STB evaluation using polarization strategy. (b) Photograph of experimental setup for Four-Pulse STB investigation of a high-subsonic jet (Mach 0.85, see [46]) with two differently polarized camera systems (blue and red). (c) Around 38,000 four-step tracks, reconstructed from a single realization. Horizontal axis y/D_j is shared with image below. (d) Binning statistics of STB results, compared to PIV evaluations of Bridges and Wernet [47].

One key feature of time-resolved LPT is high positional accuracy due to a long observation time and with it the ability to effortlessly extract Lagrangian acceleration from the particle tracks. These qualities are lost when a track consists of only two time-step observations. In order to still benefit from (some) temporal resolution, methods to record several (typically four) consecutive time-steps on conventional double-frame cameras have been developed. The first iteration of this so-called Multi-Pulse Shake-The-Box (MP-STB) used two individual camera systems that were optically separated from each other using polarization filters [48]. The light from two double-pulse lasers is perpendicularly polarized to match the filters on the cameras, such that one system would only record the light from the respective laser (as long as scattering of the light at particles preserves the state of polarization). This way, four independent recordings of the particle field become possible at arbitrary times and at full resolution of the double-frame cameras. The downsides are the involved experimental setup - requiring double camera and laser systems - and the separation of the systems in terms of calibration and light properties. These considerations spawned an updated approach that relies on a single imaging system with multiple illuminations of each frame [49]. This method proved to be more reliable than the polarization-based one, due to reduced complexity and independence of peculiarities of the Mie scattering properties of polarized light at various tracer particles.

For evaluation, an iterative strategy is applied that reconstructs the four time-steps (either as four independent IPR reconstructions or as two double-fields from the double-exposed frames), searches for matching four-step tracks and discards all reconstructed particles that were not incorporated into a track. The tracked particles are use to create residual images, which build the starting point for another iteration. See Fig. 4 a) for a schematic description of Multi-Pulse STB using the polarization method. An experimental application of this approach is demonstrated on a subsonic jet at Mach 0.85, generated by a nozzle with diameter D_j = 15 mm. Fig. 4 b) shows the experimental setup, employing eight PCO Edge double frame cameras, divided into two subsystems (red and blue for the two states of laser light polarization) and four high-power lasers to capture illuminated DEHS seeding-particles in a volume of 70 x 90 x 10 mm^3. Multi-Pulse STB evaluation yields around 38,000 particle tracks per four-frame image (Fig. 4 c)). Binning statistics on several locations above the nozzle show a clear advantage over PIV-based evaluations, which are not able to fully resolve the sharp peaks of Reynolds stresses. The LPT profiles are able to document high axial accelerations in the shear layer at the jet exit and the progressive thickening of the shear layer along the axial direction. For more details see [46]. While the polarization strategy is employed here, the multi-illumination technique was applied e.g. by Sellapan et al. [50] to measure free and impinging jets at Mach 0.31 and Mach 0.59 with comparable quality.

E. Data Assimilation and Physics Informed Neural Networks

In many fluid dynamics applications, Eulerian fields of velocity, pressure, or related quantities are required in order to compute derivatives, allowing e.g to identify vortical or other coherent structures using the velocity gradient tensor. This creates the challenge of inferring continuous or gridded Eulerian fields from discrete and randomly distributed Lagrangian particle trajectories. The earliest strategies for this task relied on interpolation, using e.g. polynomial interpolation [51] or adaptive Gaussian windowing [52]. While straightforward and efficient, these methods tend to be sensitive to noise and modulation of the data. To address these shortcomings, physics-based constraints have been incorporated into reconstruction schemes, reframing the task as a data assimilation (DA) problem [53].

Prominent interpolation-based DA methods for incompressible flows include the FlowFit framework [54, 55], which employs B-splines, and the Vortex-in-Cell (VIC) methods [56, 57], which use Radial Basis Functions (RBF). More recently, progress in machine learning (ML) has fueled the development of ML-based DA schemes for LPT. Among these, physics-informed neural networks (PINNs) have emerged as a central approach [58–60]. Unlike traditional methods based on fixed basis functions, PINNs approximate the flow using neural networks that directly map space–time coordinates to field values. These models are trained by minimizing a combined data–physics loss function, following the same principles as FlowFit or VIC. Here we will briefly introduce both the latest iteration of the FlowFit algorithm - which excels in computational efficiency - as well as the PINN methodology - which is attractive due to a relatively easy implementation of advanced regularization (like incompressible Navier–Stokes and Euler equations) and its ability to extract higher spatial resolution from the temporal domain of the LPT input data.

FlowFit3 [55] is representing the instantaneous flow field using a 3D uniform B-spline grid of weighting coefficients. B-splines can be efficiently evaluated at arbitrary positions within the reconstructed volume and provide easy access to spatial gradients. To always fulfill continuity, FlowFit3 incorporates a divergence constraint directly into the design of the method by always projecting the current state on the subspace of divergence free solutions. The divergence free projection is based on the Helmholtz-Hodge decomposition of a vector field into an solenoidal (divergence free) part $\vec{u}_{\text{sol}}$ and an irrotational part $\vec{u}_{\text{irrot}}$:

$$\vec{u} = \vec{u}_{\text{sol}} + \vec{u}_{\text{irrot}} = \vec{u}_{\text{sol}} + \nabla\phi, \tag{1}$$

with some yet to be determined potential field ϕ. Taking the divergence of (1) gives a Poisson equation for ϕ since $\nabla \cdot \vec{u}_{\text{sol}} = 0$:

$$\nabla \cdot \vec{u} = \Delta\phi. \tag{2}$$

Once ϕ is known the divergence free part of $\vec{u}$ can be determined:

$$\vec{u}_{\text{sol}} = \vec{u} - \nabla\phi. \tag{3}$$

(2) is solved efficiently under homogeneous Dirichlet boundary conditions using a Discrete Sine Transform (DST). This process then forms an orthogonal projection of a vector field $\vec{u}$ into the divergence free subspace.

In this way the constraint is satisfied at any point in the domain and the optimizer is able to more efficiently reach an optimal solution as it is restricted from even considering infeasible solutions during intermediate steps. Particle acceleration measurements can be used to further improve reconstruction quality as well as to recover pressure fields. The additional data allows for the use of the momentum equation from the incompressible Navier-Stokes equations in addition to the continuity equation.

$$\vec{a} = \frac{\mathrm{D}\vec{u}}{\mathrm{D}t} = \frac{\vec{u}}{t} + \vec{u} \cdot \nabla\vec{u} = -\nabla p + \nu\Delta\vec{u} \tag{4}$$

Accelerations obtained from LPT measurements provide the material derivative of velocity, the left side of the momentum equation. With this method pressure is no longer part of the state of the optimizer (except for boundary conditions) but this approach introduces greater complexity in the implementation of the cost function and especially its gradient. Instead of just back-propagating cost function gradients to the pressure coefficients as in prior FlowFit versions they now need to be calculated further through the pressure reconstruction all the way to the velocity coefficients instead. But again, just as with the divergence constraint, the degrees of freedom for the optimizer are reduced since this way the dependent relationship between velocity and pressure is encoded explicitly.

With the advent of Physics-Informed Neural Networks (PINNs) in the scientific community [58], multiple successful applications of PINNs to LPT data have been reported. Just as with prior versions of FlowFit the incompressible Navier-Stokes equations are used as underlying physics equations. Physics-Informed Neural Networks are deep neural network-based global function approximators that embed governing physical laws by leveraging automatic differentiation of the output components with respect to the input values. The general architecture of a PINN consists of a neural network with trainable parameters, which receives input coordinates and returns the predicted outputs. The loss function comprises terms based on the governing equations and measured data. Given velocity data at specific particle locations extracted from fitted LPT trajectories, the PINN interpolates the velocity field by minimizing the discrepancy between predicted and experimental velocities. While fitting the velocity field, the PINN also enforces physical constraints through the governing equations for incompressible flow: the continuity equation and the incompressible Navier-Stokes equation. Details of the method are given e.g. in [37]. When incorporating further governing equations in the constraints - like the energy equation - also temperature fields can be reconstructed as a hidden variable from 3D LPT data, e.g. in a Rayleigh-Bénard Convection (RBC) flow case [61]).

A direct comparison of the performance of a PINN with classical data assimilation schemes for several turbulent flows is given in [62]. Fig. 5 shows results from this publication for a near-wall region turbulent boundary layer flow between a simple binning-approach with Gaussian weights based on particle distance to the center of the bin [63], the FlowFit3 DA algorithm [54, 55] and the Neural-Implicit Particle Advection (NIPA) PINN approach[59]. While the binning-result shows clear signs of spatial modulation - most of the smaller structures are missing and the larger ones are only partly reconstructed - both more advanced methods are able produce results that closely resemble the ground truth. The inclusion of the governing equations noticeably helps in reconstructing scales that are not fully sampled by the particle field. What sets the spatio-temporal PINN method apart from the single time-step based FlowFit method is an absence of noise - which is notable specifically close to the wall for FlowFit - and a very high temporal coherence which becomes obvious when comparing animations. PINN methods are best able to maintain reconstruction quality when reducing the number of available tracer particles, as shown in [62]. However, depending on the case, PINN reconstructions require a full time-series (here 50 time-steps) in order to gain high-quality reconstructions and one to two orders of magnitude more computational power per time-step compared to FlowFit 3 [62], which in the present implementation,uses only single time-step information of the LPT data.

Benchmark tests can deliver quantitative feedback during development steps and if being freely available on public web-portals they can built-up a competitive driving force for enhancing reconstruction quality of various LPT and DA reconstruction algorithms under development in various groups and companies all over the world. Therefore, an independent benchmark test portal for both tasks has been established (first during the H2020 EU Project HOMER (GA ID: 769237)) at the website https://www.onera.fr/flow-benchmarks. Here, various flow cases based on DNS or LES simulations are used to either create time-series of synthetic particle images based on projections of advected 3D Lagrangian tracks onto four virtual cameras, which can be downloaded together with camera calibration information for the LPT Challenge cases or the 3D tracks are used directly as input data for the respective DA challenge cases. Typical position and image noise is added onto the tracks and images in order to mimic experimental boundary conditions for both benchmark categories. The results of each benchmark test can be uploaded at the portal in a predefined format and an automatic evaluation script is comparing the uploaded reconstruction results with the ground truth tracks or the respective flow field data of the original DNS/LES simulations by using standard error metrics, spectra and flow field volume slices, which are provided to the respective participant. In case the participant agrees the error report is displayed and ranked with respect to other participants at the portal.

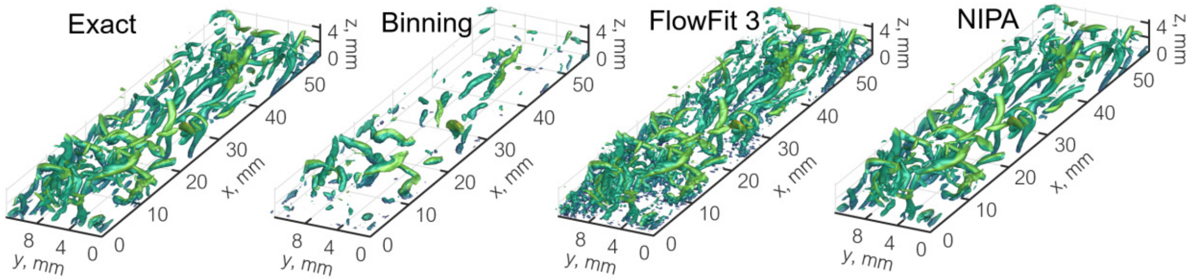

Fig. 5 Comparison of flow-field reconstruction techniques from discrete LPT data [62]. 34,500 particles were advected over 50 time-steps in DNS data of turbulent channel flow ('exact'). The particle data of the central time-step was used for reconstructing the velocity and its gradients on a predefined grid by a Gaussian-weighted binning approach and the FlowFit3 method. The particle information of the full time series is used for the NIPA PINN approach. Visual comparison of the results using iso-surfaces of Q-criterion.

III. Event-based imaging velocimetry

Event-based vision (EBV) is an imaging technology inspired by the eye's retina and falls into the category of neuromorphic sensing. The foundations of EBV were laid in the 1990's by Mahowald and Mead [64, 65] with the introduction of the "silicon retina". Since then, the technology was continuous refined [66, 67], ultimately resulting in CMOS-based detectors featuring arrays of up to 1 Mpixel [68] that can be mass-produced allowing a more wide-spread utilization of the technology [69, 70]. Each pixel of an event-based image sensor acts individually, "firing" a binary signal (= event) only if the intensity measured by the pixel's photo-diode exceeds a certain threshold. While a static scene essentially produces no intensity change events, the data rate increases once objects in the field of view begin to move. As a consequence, the data event-stream is asynchronous by nature – consisting of pixel coordinates, time of event and polarity of the intensity change.

Previous efforts of applying EBV in flow diagnostics by [71–73] were primarily aimed at 3D particle tracking at rather low particle image densities, capturing only a very limited number of tracks simultaneously. Noteworthy, is the work by Rusch and Rösgen [74] who realized an online 3D-PTV system capable of reconstructing 3D flow fields along with statistics in real-time. Contrary to the aforementioned works, the efforts by the author described in the following are aimed at achieving particle image densities comparable to those of conventional 2D-2C PIV relying on off-line processing, foregoing the online processing potential offered by the low-bandwidth of EBV.

A. Concept of EBIV

Much like a conventional image sensor (e.g. CCD or CMOS) each pixel of the event-based sensor array collects photons with a photo-diode inducing a measurable photo-current. The following conversion to a logarithmic voltage already comprises a major departure from conventional imaging and is responsible for the high dynamic range achieved by these sensors (> 120 dB). A thresholding circuit (comparator) is responsible for generating the contrast change event for a given pixel that is signaled to and registered by the readout circuitry on the edges of the pixel array. The read-out and forwarding of the registered events operates on a first-come-first-served principle, resulting in an asynchronous data stream. Both the event generation on the sensor and the subsequent digital readout exhibit delays, resulting in a discrepancy between the actual time of contrast change and the time assigned to it. This quantity is commonly referred to as "latency" and can vary between tens of microseconds up to two milliseconds, depending of light levels and event-rate.

Most of the currently commercially available sensors, such as the Sony IMX636, feature latencies on the order of 100 µs which imposes certain restrictions for applications in flow diagnostics. In practice, the events recorded by a moving particle will exhibit a timing jitter that will average out when fitting a track to the events. This works for particle tracking applications such as those reported in [71, 72, 74]. Initial event-based particle imaging work by the author [75] using denser seeded flows to obtain flow fields rather than individual tracks was challenged in obtaining sufficient events over a given sampling time to sufficiently attenuate the effects of the timing jitter, oftentimes amounting to several milliseconds. In addition, fast moving particles were found to produce fewer events per pixel than slow particles, leading to a biasing of time-averaged turbulent flows toward lower velocities.

As reported in [76], a nearly complete mitigation of the timing jitter effects can be achieved by using pulsed illumination instead of a continuous light source as the instance of the light stimulus on the sensor is precisely defined by light pulse itself. Fig. 6 show pseudo-images for a turbulent water flow at similar fields of view illuminated either with a continuous light source or with a pulsed source. Aside from the discretized nature of the particle tracks of the particle images obtained with pulsed illumination, the images appear very similar. However, the time-vs-event-rate rendition of the respective event-streams presented in Fig. 7 reveals a major difference: With pulsed illumination, events are generated in response to the light pulse (shown in green) and subside once all induced events have been read out (roughly 200 µs). This not only allows a precise temporal alignment of the triggered events using the time of the light pulse, but also removes particle streaking effects – and also captures particles at rest. Time-slicing the event data using the pulsing period provides particle image data that is well suited for both particle tracking and correlation-based (PIV) algorithms. This approach, termed “pulsed EBIV", has been the method of choice for many flow field applications involving EBV highlighted in the following sections.

The velocity range of event-based imaging velocimetry (EBIV) is primarily constrained by the previously mentioned latency of the EBV sensor, namely, the time required to register a detected intensity change, which is of order 100 µs for currently available event cameras. At a magnification of 10 px/mm (field of view (FOV) ≈ 120 mm) and an acceptable particle shift of ≈ 20 pixel results in a maximum flow velocity of order 20 m/s. This prevents the application of EBIV to high-speed flows; frame-straddling strategies as commonly used in conventional PIV cannot be realized. To nonetheless facilitate EBIV measurements in transonic or supersonic aerodynamic flows, a dual-EBV-sensor camera was devised and will be described further in Sec. III.C.

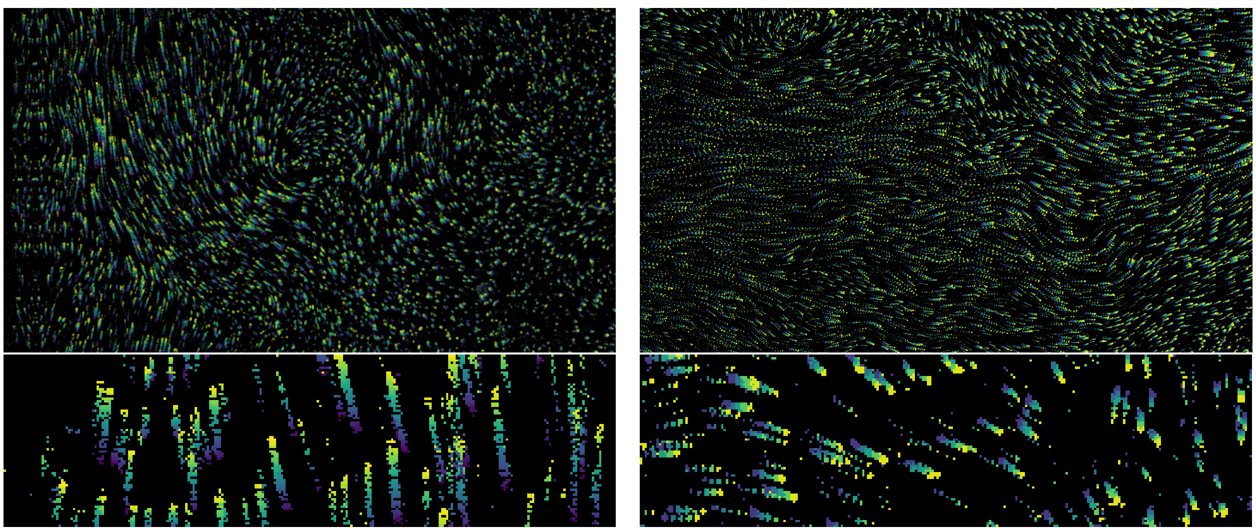

Fig. 6 Reconstructed image of particles in a turbulent water flow illuminated by a continuous light source (left) and with pulsed illumination at 1 kHz **(right). Images are reconstructed from** 25 ms **of events (left) and** 5 ms **(right). Lower row shows details of the images above. Event rate respectively is about** 10×10^6 Ev/s **and** 30×10^6 Ev/s**.**

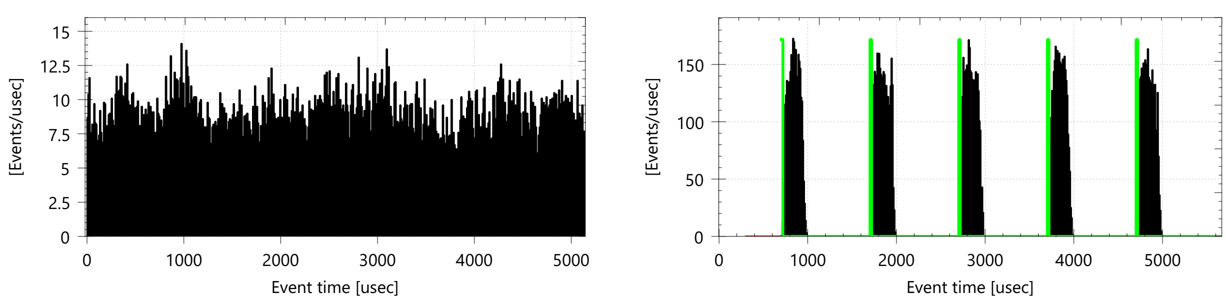

Fig. 7 Event histograms for continuous particle illumination (left) and pulsed illumination (right) for the event image data shown in the sub-figures of Fig. 6. Green trace indicates time of light pulses.

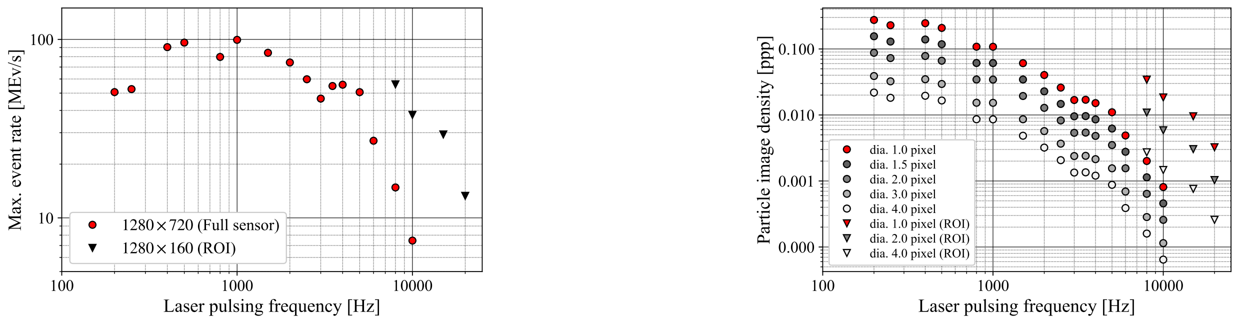

Fig. 8 Maximum sustained event-rates for pulsed illumination (left) and achievable particle image density for different particle image diameters (right). A reduction of the ROI to 1280×160 **increases the effective particle image density at higher pulsing frequencies.**

The latency coupled with bandwidth limitations on sensor readout and transfer to the host system imposes limitations on the number of events that can be reliably captured and has already been subject of several studies [77–79]. For investigations of this type the author chose a rotating disk which is densely covered by small scatterers (retroreflecting microspheres) that is illuminated by pulsed light of varying frequency and intensity [77]. For a given frequency the intensity was increased until the event-stream exhibited drop-out artifacts, typically event-free bands spanning panning the reconstructed pseudo-images (see e.g. Fig. 5 in [79]). This approach provides estimates of the maximum achievable event rates for the Sony IMX636 1280×720 pixel EBV sensor shown in Fig. 8(a), with values peaking a slightly above 100×10^6 Ev/s for light pulsing frequencies up to 1 kHz. At higher frequencies the triggered events cannot be read out fast enough leading to drop-out and a rapid reduction to levels below 10×10^6 Ev/s at 10 kHz. By limiting the active sensor area by reducing the number of active rows, results in more reliable data read-out reaching 40×10^6 Ev/s at 10 kHz.

The maximum data rates can be related to achievable particle image densities for given mean particle image diameters which is presented in Fig. 8(b). For a mean particle image area of 4 pixels and a data rate exceeding 100×10^6 Ev/s allows the capture of $\approx 25 \times 10^6$ particle images per second. At a pseudo-framing rate of 1 kHz this corresponds to roughly 25 000 particles per pulse and frame (0.03 ppp) and approaches (0.1 ppp) at lower frequencies. As these figures directly depend on particle image size any increase of source density (ppp) can only be achieved by focusing particle images to single-pixel size which, of course, will be associated with increased pixel-locking artifacts.

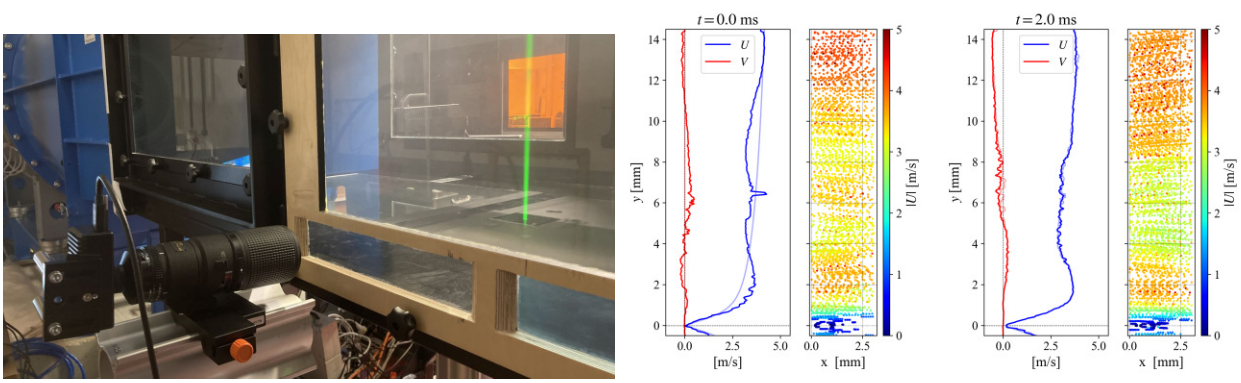

Fig. 9 Left: EBIV setup for measurement of the turbulent boundary layer (TBL) in a wind tunnel. Right: exemplary event-based particle tracking velocimetry (EB-PTV) tracking results acquired at $U_e = 5.2\,\mathrm{m/s}$ ($\mathrm{Re}_\tau = 585$) **and a laser pulsing rate of** 10 kHz**.**

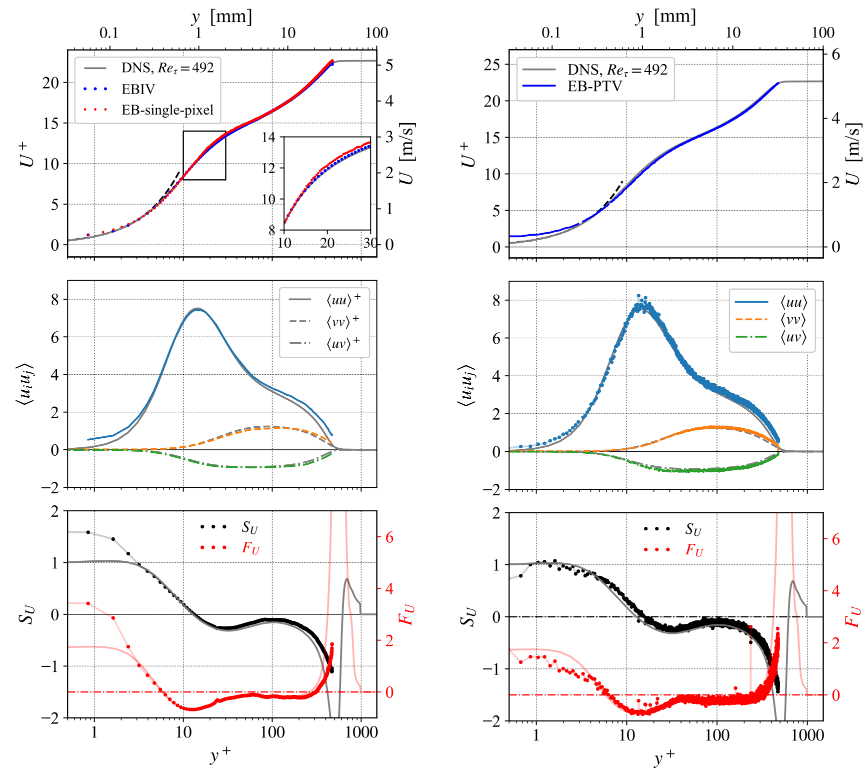

Fig. 10 Velocity profile statistics up to fourth order obtained by processing an event-based recording of 60 s duration with 2d-2c cross-correlation (left) and PTV algorithm (right). PIV interrogation window of 64×8 **pixel** ($12x^+ \times 1.5y^+$)**, vertical bin-size for PTV is** $25\,\mu m$ ($0.37y^+$)**. DNS reference data from [80].**

B. Boundary layer characterization using event-cameras

Both EBIV and event-based particle tracking velocimetry (EB-PTV) have been successfully for the characterization of TBLs. The EBIV setup shown in Fig. 9 follows the same approach as profile-PIV [81] where a narrow laser light sheet is introduced through a small glass window in the tunnel's bottom wall and viewed by a camera placed on the tunnel's side. High framing rates are achieved by reducing the field of view to a high aspect ratio strip. In the present configuration the illumination was provided by a 10 kHz pulsed laser that generated 30×10^{10} events/s on a FOV of 256×1280 pixel (3.1 mm $\times$ 15.3 mm). Multiple records of 10 s and 60 s duration were processed with both a multi-frame cross-correlation algorithm as well as particle tracking velocimetry (PTV), the latter tracking on the order of 1000 particles per time-step (see Fig. 9, right). Velocity profile statistics up to fourth order obtained with either method are presented in Fig. 10 and exhibit only marginal differences and agree well with DNS results at a slightly lower shear Reynolds number.

The sparse event-based imagery, available over long duration, is also very well suited for single-pixel correlation analysis yielding time-averaged velocity information at the pixel resolution. Following the approach of [82, 83] velocity profiles were obtained by processing the raw event-data without any additional pre-processing such as spatial filtering or background removal (see red symbols in Fig. 10a). The mean velocity profile obtained with single-pixel correlation shows only minor deviation from the DNS and conventional correlation-based estimate, most pronounced in the buffer region of the TBL, highlighted by the insert in Fig. 10(a). The feasibility of retrieving higher velocity moments from single-pixel data has been demonstrated for conventional PIV [83, 84] and should be readily applicable to event-based imagery.

In another application, a photogrammetric setup consisting of three event cameras placed underneath the tunnel captured the near wall flow of the same TBL (see Fig. 11). By bringing in a well-collimated light sheet from the tunnel side only a very thin, wall-parallel volume of 200–300 µm thickness is illuminated thereby capturing the particle motion within the viscous sub-layer of the TBL [85]. To achieve an accurate match of the individual streams, the three cameras were synchronized with a common external clock. In addition, reference markers placed into the data streams permitted

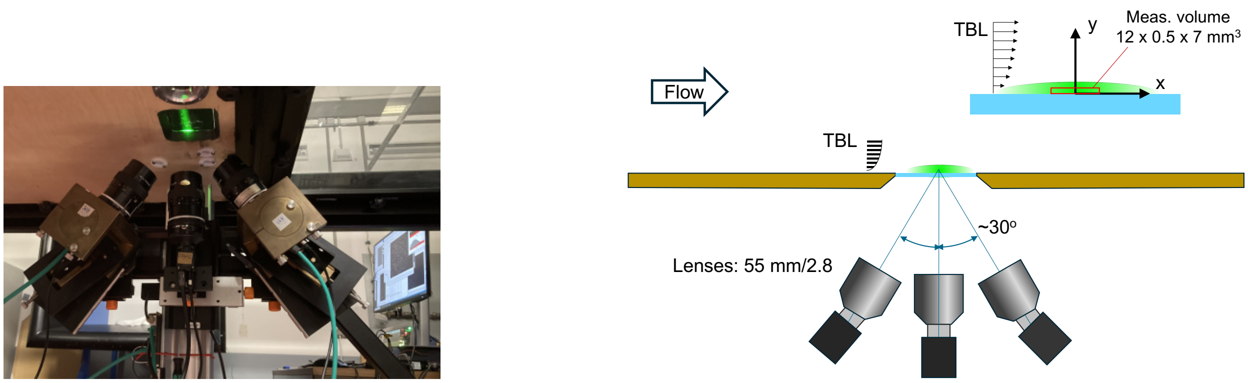

Fig. 11 Three event-cameras in a photogrammetric arrangement for near-wall particle tracking.

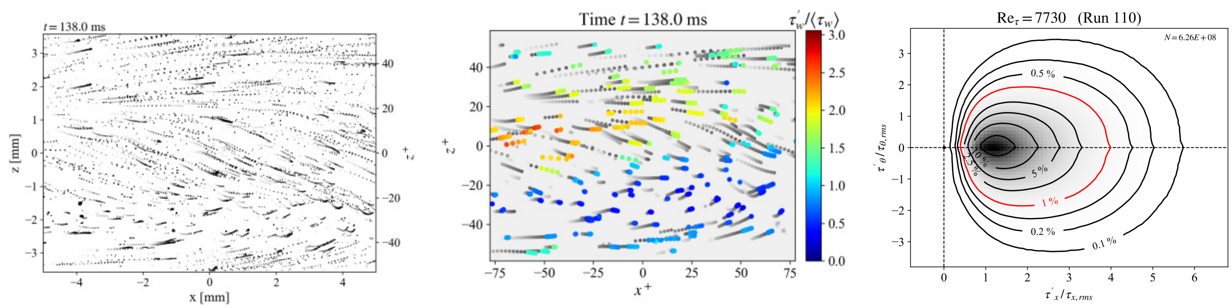

Fig. 12 Event-data for time-slices of 5 ms (left), reconstructed particle tracks color-coded with estimated wall shear-stress (middle), wall shear-stress probability distribution (right).

a posteriori temporal alignment of the particle image data. PTV provided 2D-2C tracks for each camera view that were reconstructed in 3d space using the epipolar geometry of the camera arrangement taking into account the slightly tilted plane of the wall itself. Fig. 12 provides an impression of the raw event-data, a sample of reconstructed near-wall particle tracks and post-processed data in the form of a two-dimensional probability distribution of both wall shear-stress components. Further information on this application can be found in [85].

C. Event-based velocimetry for high-speed flows

As pointed out in Sec. III.A the inherent latency of currently available event-based detectors (e.g. SONY IMX636) is on the order of 100 µs and thereby imposes a limit on resolving temporally closely spaced events. To extend the applicability of EBIV to high-speed flows an approach of image channel separation was chosen making use of orthogonal polarized light. Small (micrometer sized) aerosol particles in the Mie scattering regime preserve the polarization of the incident light such that a polarizing beamsplitter cube placed in front of the camera separates the scattered light depending on its polarization. Fig. 13, left, shows the initial proof-of-concept that was demonstrated on a high-speed jet (Ma = 0.5, U_0 = 180 m/s) with pulse delays down to Δt = 100 ns [86]. A more robust implementation was made possible through the recent availability of compact board-level sensor-modules that could be directly mounted on an optical cage containing an adjustable 25 mm polarizing beamsplitter cube (Fig. 13, right). The compact assembly is suited to be operated in environments unsuited or inaccessible for high-speed cameras; a pair of high-speed USB connections to a host computer is sufficient for operation.

D. Real-time event-based velocimetry

The sparse data stream of event-cameras, typically below 100 MB/s, allows for continuous data streaming and additionally opens the possibility of the real-time data processing. Previous work on 3D EB-PTV by Rusch & Rösgen [74] already demonstrated real-time reconstruction of mean flow fields by continuous tracking on O(100–200) LED-illuminated HFSB tracers in wind tunnel configurations at flow speeds of up to 50 m/s. In the context of EBIV

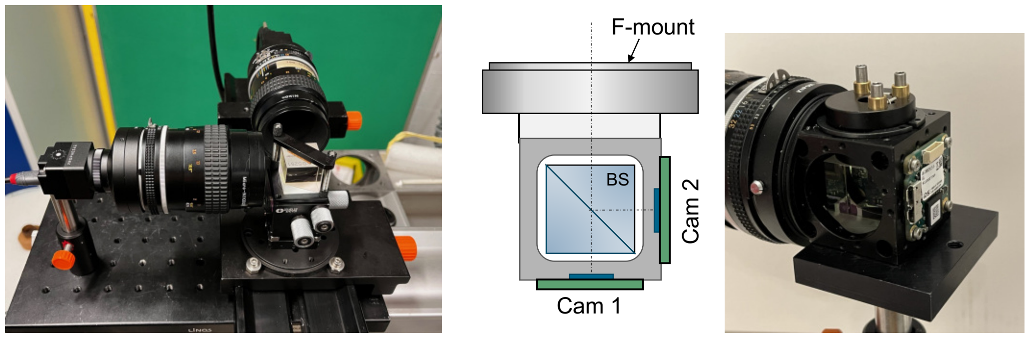

Fig. 13 Dual event-camera setups for the measurement of high-speed flows; right: proof-of-principle using two cameras with individual lenses and a beamsplitter cube; middle, left: prototype using board-level sensor modules directly mounted on an optical cage containing an adjustable beamsplitter cube (BS).

the aim is to reconstruct dense (2D) flow fields with minimal latency as an input to active control configurations as outlined in Fig. 14a. Whereas frame-based imaging always is delayed by the frame readout interval, the pseudo-frames of an event-camera are immediately available at the completion of the framing interval which reduces the overall system latency (see fig. 14b) and can be dynamically adjusted in terms of framing time. Depending on the processing algorithm and required spatial resolution data rates well beyond 100 fields/s are readily achieved using conventional CPU architectures and can exceed 1 kHz for a reduced number of sampling points [77]. This corresponds to response times in the range of 1 ms to 10 ms which matches the time-scales of many "real-world" applications. Implementations of the real-time event-based imaging velocimetry (RT-EBIV) concept were recently demonstrated in both open-loop and closed-loop configurations [87].

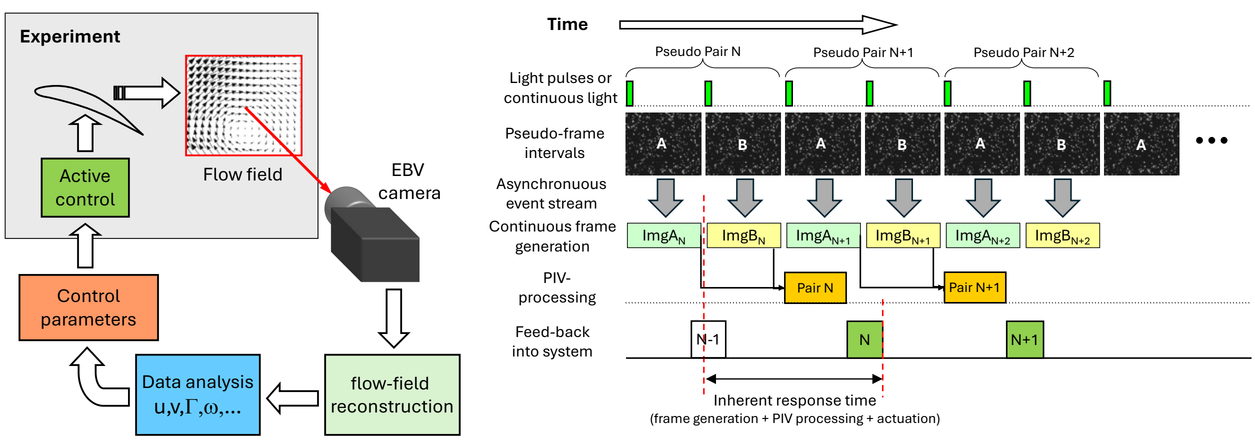

Fig. 14 Real-time EBIV for active flow control applications (left) and timing sequence (right).

E. Summary and further development potentials of EBIV

As demonstrated in the previous sections, EBIV can capture dense velocity field data at framing rates in the 10 kHz range employing hardware at a fraction of the cost of an equivalent PIV system. A camera based on the novel event-imaging concept is more than an order of magnitude cheaper than a comparable high-speed framing camera, moreover, the high sensitivity of EBV sensors with a dynamic response of >120 dB reduces the power requirements of the high-speed laser system. The compact size of EBV cameras (typically a cube of about 30 mm side length, without lens) allows placement in configurations typically inaccessible or deemed too risky for bulky and expensive high-speed cameras. Along with their low power consumption (≈ 1 W) embedded or in-flight applications similar to those employing "action cameras" are considered feasible.

Among the further development potentials to be explored is the direct use of the asynchronous event-stream rather than via the pseudo-framing approach currently employed by both EBIV as well as many other applications involving EBV. Ongoing research efforts in the EBV community are directed at directly processing the asynchronous data, often in conjunction with (trained) neural networks. The 3D-PTV implementation by [74] already featured event-by-event processing, albeit at a reduced number of simultaneously tracked particles.

Next generation EBV detectors may feature a reduced latency, ideally in the 1 µs range, and possibly also larger array sizes, respectively increasing temporal and spatial resolution of EBIV. Along this path an EBV-sensor architecture with a contrast change threshold of order 1 % was recently demonstrated [88, 89] with further advancements to be expected. In summary, the combination of compressed imaging provided by EBV along with the associated reduced data stream holds considerable potential for long term (unsupervised) measurements of flow fields. At the same time the technology directly provides contrast enhanced imagery that in itself comprises a powerful tool for flow visualization. A minimal investment cost along with reduced demands on light sources makes the technology readily accessible in educational environments.

IV. Unconventional imaging configurations

A. Lensless PIV

Lensless imaging eliminates traditional optical lenses and instead uses computational methods to reconstruct images directly from recorded diffraction or interference patterns [90, 91]. When applied to PIV, this rapidly advancing technology, combined with ongoing miniaturization efforts, could enable the development of embedded sensors capable of making measurements in previously inaccessible locations. Additionally, the encoded image contains three-dimensional information about the scene, making it possible to obtain 3D velocity vectors from a single sensor.

The motivation for lensless PIV stems from some of the limitations of traditional PIV, specifically when it comes to making near-surface measurements with long working distances, or acquiring data in cases with limited optical access. Lensless PIV is not meant to replace traditional PIV in cases where that approach works well, but is meant to enable measurements that are not feasible with traditional lensed systems. When the large lens can be replaced by a thin mask, it becomes possible to create a small embedded sensor that could capture both 2D and 3D near-surface velocity data, enabling embedded sensors within wind tunnel models or even a flight vehicle. Lensless PIV represents an emerging approach to address these challenges, though the field remains in early development stages with primarily benchtop, proof-of-concept experimental data.

1. Basic Principles

Lensless imaging began with the pinhole camera, but modern computational lensless imaging employs a variety of coded apertures or phase masks to encode light information onto the sensor [92]. Unlike traditional imaging systems that result in recognizable images being focused onto the sensor plane, lensless imaging systems produce unrecognizable encoded patterns that require computational algorithms to extract meaningful scene information. With knowledge of the point-spread function (PSF) of a particular mask and sensor combination, the scene can then be reconstructed using computational algorithms. The relationship between the scene and the recorded image can be expressed as a forward model, where the measured image results from the convolution (or more complex interaction) of the scene with the system PSF. Different mask designs, including random diffusers, coded apertures, and structured phase plates, create distinct PSF patterns, with mask parameters optimizable for specific applications such as depth sensing or spatial resolution [93]. Reconstruction algorithms leverage these PSF characteristics to determine particle positions. Sample PSFs for different diffuser-type masks are shown in Fig. 15.

In the context of PIV, the PSF essentially represents the signature of a single particle on the sensor (in practice, the PSF is simulated by illuminating a pin hole). If the particle shifts in the in-plane direction, the PSF will simply shift by a number of pixels proportional to the spatial shift of the particle and defined by the magnification of the system (determined by the relative spacing of the mask-to-sensor and image plane-to-mask distances). If the particle shifts out of plane, the PSF pattern projected on the sensor will either expand or contract. When multiple particles are present, multiple PSFs appear on the sensor and superpose to create an image such as that shown in Fig. **??**.

2. Reconstruction Approaches

Over small in-plane regions, many lensless systems can be modeled as shift-invariant, which means that the PSF pattern does not change substantially as the point source location is changed. Often, an aperture is added in front

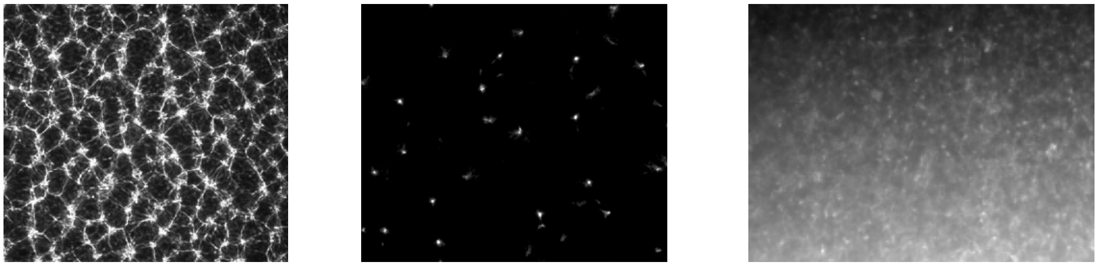

Fig. 15 Point spread functions from two different diffuser masks showing distinct encoding patterns (left and middle and example raw lensless image showing superposed PSF patterns from multiple particles present in the measurement volume (right).

of the mask to create an approximately shift-invariant system, but this reduces the spatial field-of-view that can be reconstructed. In the simplest form, for a shift-invariant system, the image reconstruction is, essentially, a deconvolution of the encoded image with the PSF. In this case, the forward model is simply a convolution of the scene with a single PSF. By knowing the characteristic PSF response, deconvolution algorithms can recover the original scene information from the encoded measurements. However, this straightforward approach is limited to shift-invariant systems and faces significant challenges in practice, including noise amplification, ill-conditioning of the inverse problem, and the need for accurate PSF knowledge. These limitations have led to the development of more sophisticated reconstruction methods incorporating regularization techniques, sparsity parameters, and iterative algorithms, as well as the incorporation of shift-variant PSFs.

Common reconstruction approaches include iterative optimization methods such as the Alternating Direction Method of Multipliers (ADMM), with more recent approaches utilizing deep learning-based methods [94]. The reconstruction method used in the initial work [95] involved performing Lucy-Richardson deconvolution over smaller image windows, with results then stitched together. This helped to account for the shift-varying PSF. However, this method proved time-consuming. Given the availability of ground-truth data, subsequent experiments focused on developing a deep-learning algorithm to enable faster image reconstruction.

The deep-learning reconstruction method used in the most recent lensless PIV experiments is based on the framework of Yanny et al. [96], in which an initial deconvolution step is performed using a learnable Wiener filter, followed by a UNet denoiser module to produce the reconstructed images. The model was initially trained solely on synthetic particle images with particles generated at various depths in order to account for the finite thickness of the laser sheet, enabling 3D reconstruction. However, this model resulted in low precision of 50-75%, depending on the noise conditions applied during training. Therefore, a finetuning step was added to train the model on real lensless particle images. Unfortunately, with the current setup, the finetuning step could only be performed on 2D images, since the lensed (ground-truth) images that were acquired contained only 2D data. To enable this, the 3D reconstruction produced by the model was collapsed into a 2D particle image, which was then fed into the alignment layer that scales and shifts the reconstructed images for direct comparison with ground truth data. This algorithm achieved reconstruction speeds of 0.03 seconds, approximately 2000 times faster than the previous Lucy-Richardson based method.

3. Experimental Setup, Procedures and Results

The benchtop experimental setup utilized for the proof-of-concept demonstration is illustrated in Fig. 16. Existing PIV equipment was utilized, including time-resolved PIV cameras, which were chosen primarily due to the flexibility with placement of the mask relative to the recessed sensor, though the high-speed capabilities of the camera were not required for this application. A lensed and lensless camera were positioned to image the same plane simultaneously, providing ground-truth data for comparison. A small table-top wind tunnel created consistent airflow. In some cases, a plate was placed partially covering the exit of the blowdown tunnel to create unsteady non-uniform flow fields and to demonstrate a more challenging flow field reconstruction. The experimental geometry used 14 mm for both laser-to-mask and mask-to-sensor distances (1:1 magnification) to match the lensed system's magnification, resulting in a final resolution of 103 pixels/mm. Seeding was provided via a small oil-based fog machine. Details of initial experiments with different optical configurations can be found in [95].

Two different masks were tested during the development process. The mask used in earlier experiments (left PSF in Fig. 15) was a piece of thin plastic that created a caustic pattern with a fairly large depth of focus, meaning that the caustic pattern remained relatively well focused for a large range of distances from the sensor. While functional, this mask's non-sparse nature led to sensor saturation issues. The mask employed in the results presented here (right PSF in Fig.15) was fabricated using a copper plate hammered randomly with 8-mm diameter steel balls as a mold for the optical epoxy mask. This mask acts as a low-cost random microlens array with a much narrower depth of focus, where 8 mm was chosen as the appropriate lens diameter for the desired focal length and optical setup.

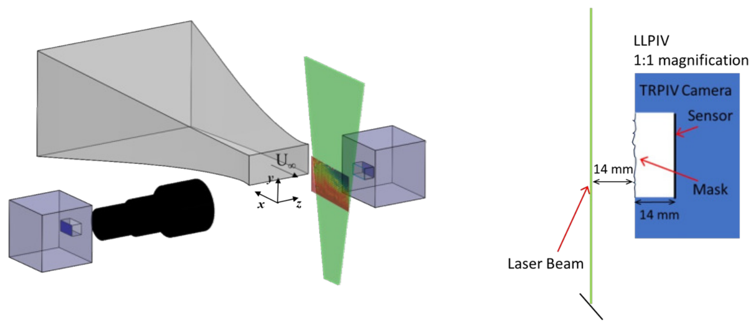

Fig. 16 Left: Experimental Benchtop Lensless PIV Setup. Right: Side view of the camera showing sensor and mask displacement. Adapted from [95].

The original experiment [95] suffered from several limitations: inconsistent seeding, sensor saturation with relatively low particle density (due to the non-sparse nature of the mask PSF), and rudimentary reconstruction techniques. Despite these limitations, it was sufficient for demonstrating the feasibility of using lensless imaging for PIV measurements. For the subsequent work described here, adjustments were made to the experimental setup (new sparser mask, larger magnification) to improve upon previous results. Additionally, a deep-learning algorithm was developed, as described briefly in section IV.A.2.

4. Particle Reconstruction Results

The deep learning reconstruction model was trained on synthetic data with various noise conditions and then fine-tuned on real experimental images. While the particle reconstruction recall remains limited at approximately 16%, the fine-tuning step significantly improved precision from 50% to over 90%. The algorithm performs well on brighter particles but struggles with weaker, dimmer particles - a limitation that may be addressable through improved training strategies. The metrics used here include recall (the fraction of true particles detected by the reconstruction algorithm) and precision (the fraction of reconstructed particle detections that correspond to real particles in the ground truth). Figure 17 shows example particle reconstructions before and after finetuning of the model.

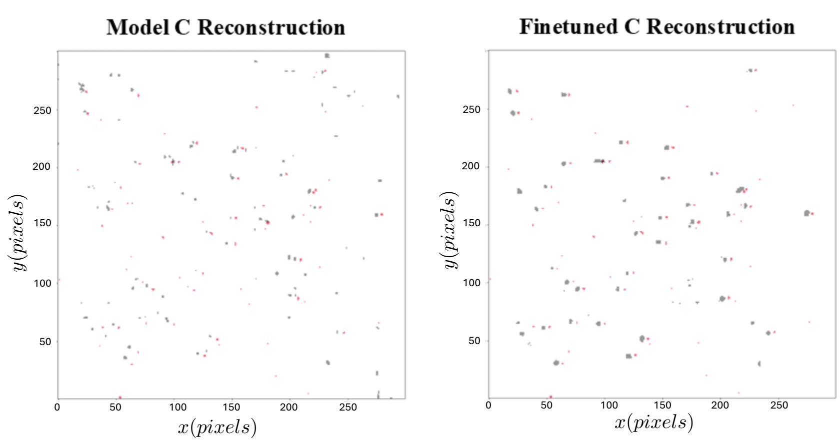

Fig. 17 Comparison of reconstructed particle images (grey) overlaid with the corresponding lensed particles (red). The images are offset slightly along the x-axis for easier comparison.

5. PIV Results

While the number of reconstructed particles with the current algorithm is not ideal for PIV processing, we can compensate by using a relatively large window size. Although this approach sacrifices spatial resolution, it is quite adequate for comparing overall flow features and obtaining an initial measurement of the accuracy of the reconstruction approach. For the results presented in this section, 1100 PIV images were processed using a window size of 256x256 pixels, with 75% overlap. This window size typically gave an adequate number of particles (approximately 10) per window in the reconstructed images. This processing was completed for a steady, uniform flow and an unsteady flow dataset.

The steady flow case consisted of uniform flow in the x-direction with an average velocity of 1.2 m/s and relatively low fluctuation levels (average standard deviation of 1.8% of the mean velocity). The results indicate relatively good agreement between the lensless and lensed PIV methods, with flow direction and magnitude being captured well by the reconstructed images. Error metrics are computed by comparing lensless with lensed PIV results (treated as ground truth) and normalizing by the corresponding lensed velocity magnitudes. For errors computed on the ensemble-averaged fields, the mean normalized error of the time-averaged velocity field is 0.03, while the error increases to 0.06 when error statistics are computed over each individual vector field and then averaged together, and the root-mean-square error (RMSE) is 0.075. The lensless PIV resulted in an overall increase in fluctuation level, with an average standard deviation of 3.17%. While this represents a 76% increase in fluctuation levels compared to the lensed measurements, the absolute noise level remains manageable and demonstrates the feasibility of lensless PIV for steady flow applications.

Results from the unsteady flow field are presented in Fig. 18. The top row illustrates that the overall flow patterns and the flow vectors are qualitatively captured well by the lensless approach; however, there are clear differences in velocity magnitude and fluctuation levels. For errors computed on the ensemble-averaged fields, the mean normalized error of the time-averaged velocity field is 0.093, while the mean normalized error of the standard deviation is 0.164. In contrast, when error statistics are computed over each individual vector field, the mean error is significantly higher at 0.29, and the RMSE is 0.38. It has been found that an instantaneous velocity field, the lensless method captures the primary flow structure and velocity gradients, with good agreement in the lower shear region and some discrepancies in areas of higher velocity gradients.

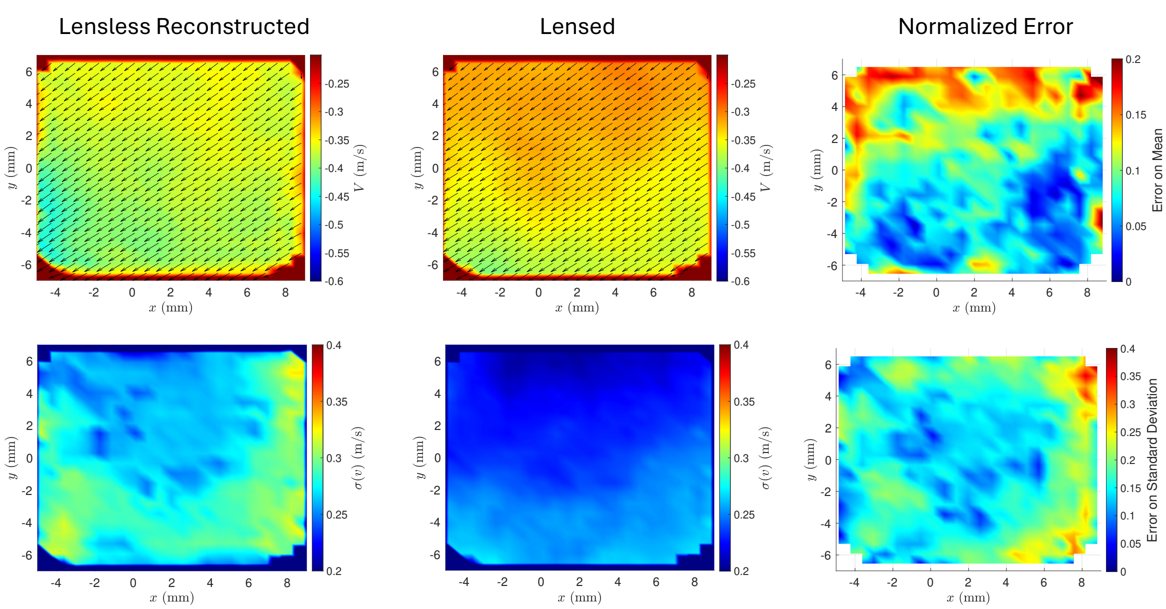

Fig. 18 PIV results for the unsteady flow field. Top row: time-averaged flow field with velocity vectors overlaid; bottom row: standard deviation. Color contours in the left and middle columns show the V-component of velocity (top) and standard deviation of V-component fluctuations (bottom). The rightmost column shows normalized velocity error computed over both velocity components for the respective statistical quantities.

6. Summary and Future Developments of lensless PIV

Lensless PIV, though still in the early stages of development, shows promise in its ability to capture the primary flow structures in an unsteady shear layer. However, the current lensless PIV approach faces several key limitations that must be addressed for practical implementation. The most significant challenge is inadequate particle reconstruction rates, as current algorithms struggle to detect and reconstruct the weaker particles. It remains to be seen whether this is a fundamental limitation of lensless PIV, or rather specific to the particular reconstruction algorithm used. For instance, the training data may not have included enough dense particle scenes. Up to this point, the effort and analysis has been focused on using this approach with PIV algorithms, but in the end, lensless imaging may turn out to be more well-suited for particle tracking, if the ability of the algorithms to reconstruct weaker particles turns out to be an inherent limitation. Additionally, unlike traditional PIV, where particles are immediately visible in the raw images, lensless PIV requires image reconstruction before particles can be observed, necessitating fast algorithms such as the deep-learning approach presented here for real-time or near-real-time feedback. Near-term improvements should focus on optimizing both mask design and reconstruction algorithms to address these fundamental issues.

In addition to the improvements listed above, future work will investigate more transformative advances through bypassing particle reconstruction entirely via direct computation of velocity vectors [97], which could eliminate current reconstruction limitations. Additionally, we plan to explore three-dimensional algorithms combined with stereo velocity data from conventional lensed systems, which could provide enhanced spatial information within the current reconstruction framework. Practical implementation challenges, such as viewing through curved glass surfaces in wind tunnel or flight applications, will also be addressed. Such optical complications can likely be overcome through appropriate PSF calibration methods, but may also impact the algorithm choice. Although lensless PIV has fundamental limitations including small working distance requirements and potentially limited accuracy, it fills an important gap by enabling measurements in locations that are otherwise inaccessible to traditional PIV methods.

B. In-line PIV

Since the obtained particle image intensity and the contrast of PIV recordings is directly proportional to the intensity of the scattered light, it is often more effective and economical to increase the image intensity by properly choosing the scattering particles instead of increasing the laser power. In general, the light scattered by small particles is a function of the particle's size, shape, orientation and the ratio of the refractive indices of the particles and the surrounding medium. Furthermore, the light scattering depends on polarization and observation angle. For spherical particles with diameters larger than the wavelength of the incident light, Mie's scattering theory can be applied. A detailed description and discussion are given in the literature [39, 98, 99]. The following section demonstrates the feasibility of an in-line imaging configuration and the subsequent evaluation. When the camera is placed in-line, the effective measurement volume depth in the direction of the line of sight is not limited by the well-defined edges of a laser light sheet or volume, but by the depth of focus (DoF) of the camera/lens combination and extends on parallel work introduced in [100]. The most commonly used optical in-line measurement technique in aerodynamics is schlieren or shadow photography [101]. The optical setup of Toepler's schlieren method consists of spherical mirrors or lenses and a light trap, often in the form of a half aperture, e.g., a knife edge. It captures variations in light intensity proportional to the first derivative of the fluid density [102]. In [100] it was shown that setups used for schlieren photography can also be used for in-line PIV. A setup very similar to Toepler's schlieren method was implemented within this study and is described further below.

1. In-line PIV with schlieren mirrors

Figure 19 depicts an example of an improved in-line PIV set up using two schlieren mirrors. The laser light is focused by two large focusing mirrors onto a light trap, which is located in front of a distant imaging lens. With the exception of smaller quantities due to lens imperfections and scatterers on the lens and mirror surfaces (e.g. dust and scratches), the majority of the emitted light is hindered from reaching the imaging sensor. Compared to the previously described configuration, this configuration allows for a wider field of view, with a constant illumination diameter along the measurement volume. In the current sample case, the ejector nozzle (D = 100 mm) of a seeding generator was placed in the measurement volume, with the generator providing both flow tracers and a constant low-speed airflow crossing the field of view in upward direction.

As mentioned above, in contrast to conventional light-sheet based PIV, in-line PIV is expected to have an increased image background intensity level caused by lens imperfections, lens contamination and out-of-focus tracer particles. The light scattered by particles within the depth of field of the imaging lens is well concentrated on a few pixels and can therefore be enhanced by digital image filtering. In case of the experiment described next, the light of a low-cost

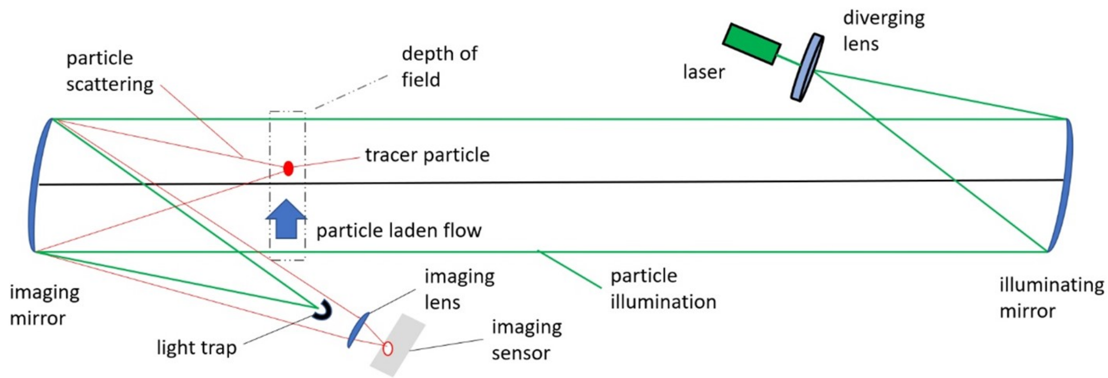

Fig. 19 Example setup for in-line PIV recording with schlieren mirrors and light trap between the receiving imaging mirror and the imaging lens[103].

diode-pumped solid-state laser (Spectra Physics Excelsior, λ = 532 nm, $P_{\text{cont.}}$ = 250 mW) is expanded to about 400 mm over a distance of 4 m using a set of two biconcave lenses. The illuminated volume is imaged by a high-speed CMOS camera (PCO.Dimax S4) with an acquisition rate of 1.2 kHz, an image exposure time 19 µs, and a resolution of 2016 × 2016 pixel. It has been fitted with an f = 300 mm macro lens (Nikon AF-S Nikkor 55–300 mm 1:5.6). The working distance of the imaging lens is 2015 mm between the lens and the imaging mirror plus an additional 2000 mm between the mirror and the plane of focus. With the lens aperture set to $f/\#$ = 5.6, the Depth of Field DoF is estimated at 25 mm. A sequence of 500 images was recorded within 0.41 seconds.

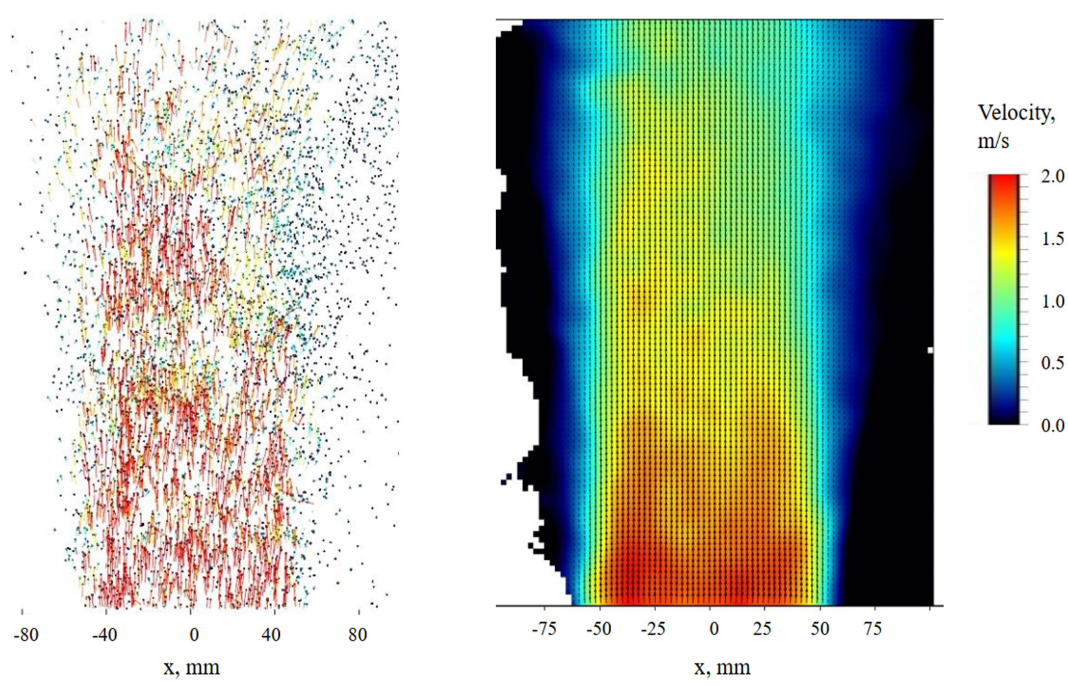

Fig. 20 Instantaneous flow field represented by particle tracks (left), and averaged flow field (right) [103].

The raw image data was filtered and evaluated with commercial PIV software. In order to differentiate between stationary images of dust particles, laser diffraction patterns and moving tracer particles, a temporal high-pass filter was used, which subtracted a sliding average signal over 50 images However, many different filter options contained in the aforementioned software package yield very similar results.

To retrieve quantitative velocity data, particle tracking was applied to the filtered image data. The detected particle images had an average brightness > 85 counts, with some exceptional bright particles having 500–1000 counts. The particle fit used Gaussian windows of 5×5 pixel. The tracking routine found about 5000 active particle tracks in each recording of an individual time step. The sample result in Fig. 20), left, depicts Lagrangian tracks consisting of 5 subsequent time steps. The color coding shows velocities between 0 m/s and 2 m/s. The flow direction is bottom to top, and the tracks reveal turbulent structures in the instantaneous flow field. Entrainment effects introduce small velocities in the surrounding of the jet. A time-averaged result was computed over the series of 500 images by binning the PTV data to a regular grid, window size 64×64 pixel with 75% overlap, see Fig. 20, right. Despite the short time interval, the average result reveals a more or less homogeneous velocity distribution over the jet's cross-section. In downstream (here: upward) direction, the shear layer between the jet and the external flow thickens, whereas the maximum velocity in the jet core decreases.

The in-line PIV configurations set up utilizing schlieren mirrors showed the feasibility to obtain larger fields of view of up to 0.2 m width. The technique worked best with high particle concentrations in the regime of the focal plane, but low particle concentrations outside of the measurement domain. Acceptable results could also be obtained in the wind tunnel with a low-power pulsed laser. Although this configuration has the disadvantage of a blind spot in the middle of the observation area, it allows a considerably increased observation area without the need of large aperture mirrors.

Based on the authors' experience several commonalities can be summarized: Tracer seeding within the imaging path, which are out of focus, will significantly reduce image contrast. Similarly, intermediate surfaces such as windows, mirrors and lenses should be kept clean and should preferably be of high quality. A combination of long focal length with large aperture and a considerable working distance can achieve a depth of the measurement domain in the millimeter range. For highly three-dimensional flows a limited depth of field requires the reduction of the separation time between both exposures to prevent loss of particle image pairing, just as in conventional PIV where the light sheet thickness defines the depth of the measurement domain. The in-line imaging arrangements have a relatively high background intensity level on which brighter particle images can be detected. Ideally this background is constant in time such that it can be removed through subtraction.

The use of forward scattering has a significant influence on the required pulse energy of the light source used. Typically, sufficient illumination is achieved with about 1% of the pulse energy that would normally be used for a conventional orthogonal PIV arrangement employing a laser light sheet. It should be noted that the present work does not cover all possible configurations, nor have all aspects of this interesting technique been fully explored. Nonetheless, it can be concluded that for some experimental setups interesting variations of the recording arrangement and along with reductions in the required light power can be achieved.

C. Retro-reflective PIV

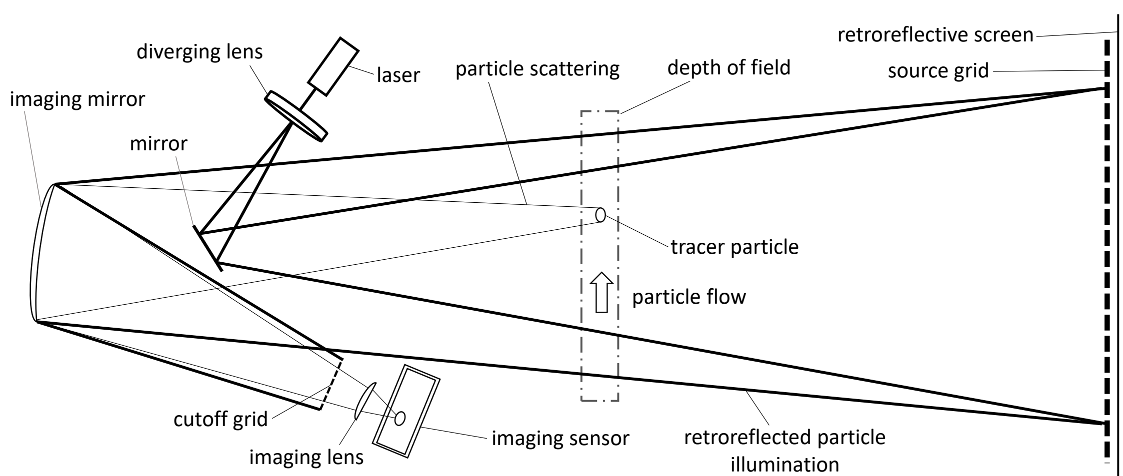

Fig. 21 Schematic representation of a retro-reflective PIV setup with laser illumination via a deflection mirror in front of the imaging mirror.

The disadvantage of the in-line PIV setup described above is that the size of the measurement volume is limited by the size of the lenses used. A cost-effective and significant increase in this volume can be achieved by using a retro-reflecting film, as shown in the following schematic diagram. The direct light beam that is not refracted by tracer particles is shaded by combining a positive grid ("source grid", in the background) with a negative grid ("cutoff grid", close to the camera). The combination of the two grids forms a beam trap, which is overcome when the light beams between the two grids are deflected by tracer particles. Here, too, all particles located in the focal plane of the imaging lens are sharply imaged on the image sensor. The grids can consist of lines, a checkerboard, or dot patterns.

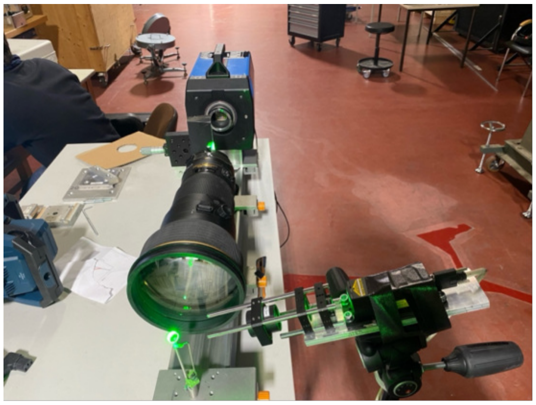

Fig. 22 Retro-reflective PIV setup with laser illumination (from the left) and the light trap behind the imaging lens (in the foreground on the right). A half aperture between camera and imaging lens serves as 'cutoff grid'.

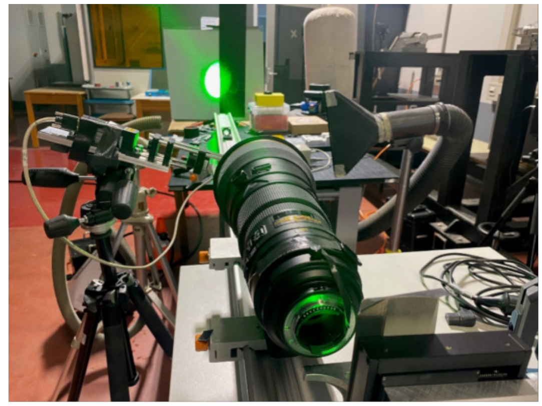

Fig. 23 Example of a retro-reflective PIV recording photographed in viewing direction from the camera to the retro-reflective background. A dark upright board serves as 'source grid'.

The setup shown in Figs. 22 and 23 was used to demonstrate the feasibility of the proposed imaging configuration. In this case no imaging mirror has been used, but just an imaging lens. The light source-mounted on a tripod on the left was a laser with a continuous power of only 250 mW. The imaging lens – at the front of the image – was a standard 400 mm Nikon telephoto lens while the camera featured a sensor with 2016 × 2016 pixels. The tracer particles with a nominal size of approximately 2 – 3, µm were generated with a specialized particle generator (CTS1000, Seika Digital Imaging).

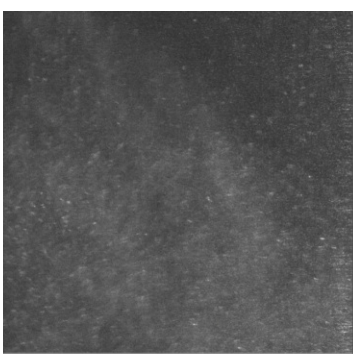

Fig. 24 Raw image of a retro-reflective PIV image.

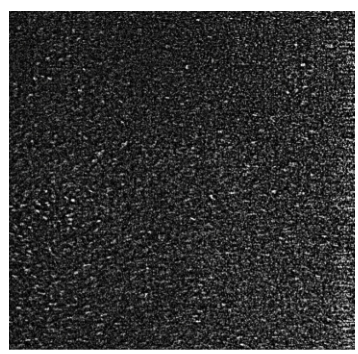

Fig. 25 High-pass filtered retro-reflective PIV image.

Figure 24 shows a typical result of a retro-reflective PIV image acquired with the above-mentioned setup. It can be seen that the image is dominated by residual light caused by lens imperfections and lens contamination, as well as by light scattered from out-of-focus particles. By applying a digital high-pass filter, the background intensity can be reduced making the traces of the focused particle illumination clearly visible (Fig. 25).

Similar to self-aligned focusing schlieren (SAFS) (see, for example, [104]), a retro-reflective PIV setup can also be modified so that the light source projects a pattern onto a background and, at the same time, the same pattern is used as an aperture. The advantages of this setup are that the alignment depends only on the adjustment of the Rochon prism and no additional pattern is required on the background. This makes the entire setup less sensitive to external disturbances, as vibrations can be absorbed, for example, by mounting the optical setup more easily on a rigid body.

1. Potential applications of in-line and retro-reflective PIV configurations

- One application would be for primarily two-dimensional flows with limited optical access, for example in a transonic wind tunnel with the aid of a pulsed laser. Otherwise, a probe would have to be placed downstream in the flow, which would require a great deal of effort.
- An event camera will be able to cope with the strong background signal. This would allow time-resolved measurements to be carried out at a frame rate of up to approximately 1 kHz (Δt = 1 ms) and, with pulsed light, even up to approximately 10 kHz (Δt = 100 µs) [76].
- A configuration of 2-3 crossed in-line systems will make three-dimensional flow fields accessible [105].

V. Time-Resolved PIV for High-Speed Flows

TR-PIV has become so prevalent that it may soon become more common than conventional PIV. Even in high-speed flows (transonic and above), the commercial availability of suitable lasers and cameras has regularized TR-PIV. Common and affordable lasers provide sufficient energy at fast repetition rates (approximately 10–100 kHz) and high-speed cameras can match these speeds and still retain adequate image quality and pixel count. The use of a pulse-burst laser can raise repetition rates to MHz levels and, importantly, provide high energy in each pulse. A full review of TR-PIV, including modern equipment and algorithms, is provided by Beresh [106].

A. Continuously Pulsed Lasers

Nd:YLF lasers remain a staple of TR-PIV experiments but a new generation of Nd:YAG designs is better able to combine large pulse energies with repetition rates well past 10 kHz. Meanwhile, the economy of scale for high-speed cameras has created a more rapid acceleration of technology resulting in faster cameras with more pixels and better signal to noise – though not necessarily lower cost.

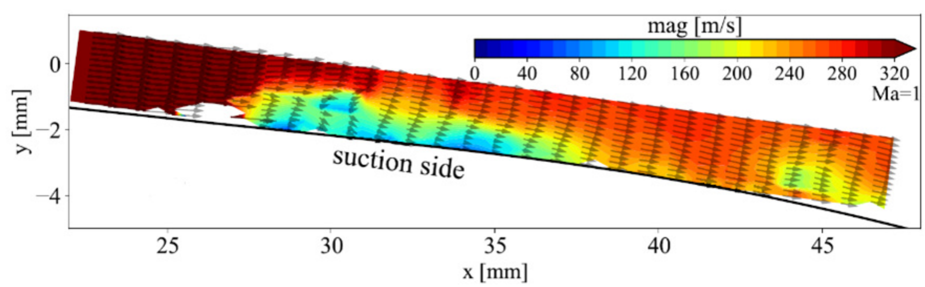

Fig. 26 Single velocity field of a sequence captured at 35 kHz along the surface of a compressor blade.[107].

Application to transonic turbomachinery seems to have been popular in recent years and serves as a good exemplar for modern capability. Klinner et al. [107, 108] have acquired TR-PIV data inside a transonic compressor blade cascade, which adds to the high-speed challenge the additional burden of obtaining optical access within the restricted access between adjacent compressor blades. The laser sheet was counter-propagated in the streamwise direction from downstream into a narrow field of view measuring no larger than 27 mm × 3 mm to concentrate the laser energy just above the surface of a compressor blade. They acquired velocity field sequences at rates up to 50 kHz, with Fig. 26 showing an example at 35 kHz. Although the shock foot scarcely moves during this time because the buffet frequencies are much lower, the separation shear layer is highly unsteady and vortices alter shape quickly as they convect along the blade surface.

The power of TR-PIV is its ability to reveal spectral content within the velocity field to complement what surface sensors can detect. Spectral content from a streamline just above the blade surface is shown in Fig. 27, with spectrograms in (a) showing the evolution of the shock-induced unsteadiness along the streamline and extracted plots in (b) at two locations providing detail. Prominent energetic frequencies are revealed at 1.7 and 3.4 kHz in both velocity components in the spectrograms but the higher frequency is weak in the wall-normal direction and difficult to detect in the extracted PSDs. These resonance frequencies, one a harmonic of the other, are generated by the dominant shock buffet motion. An additional frequency is found only in the wall-normal component at 170 Hz amidst an elevated region of broadband, low-frequency content; this is attributed to unsteady motion of the shock foot and its amplitude diminishes further downstream from the mean shock foot location at position 1. Klinner et al. used these velocity field measurements to

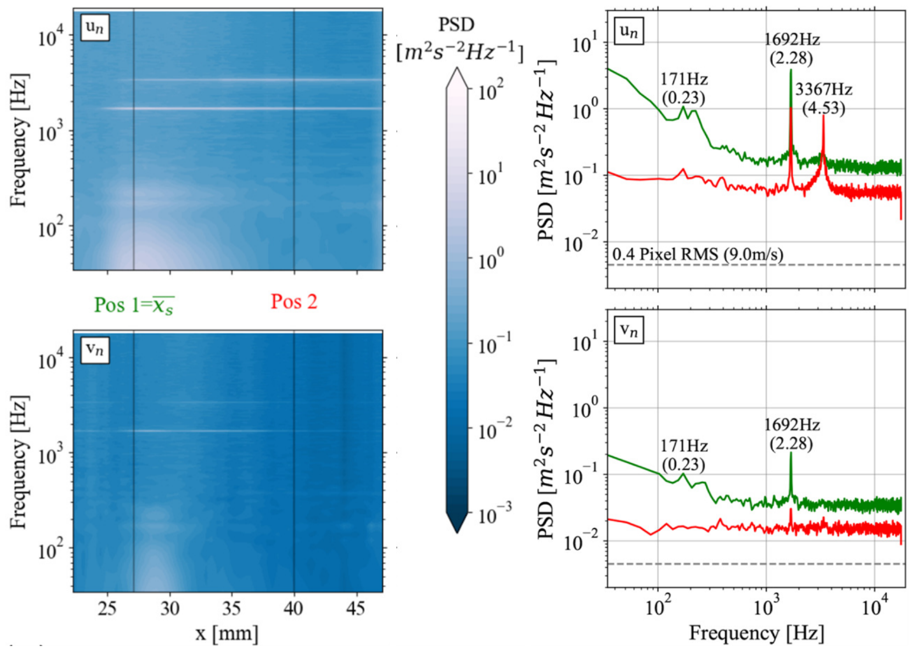

Fig. 27 (a) Spectrograms computed along a streamline near the compressor blade surface through velocity sequences like Fig. 26; (b) power spectral density plots extracted from the spectrograms as positions 1 and 2. From [107].

test theories about acoustic feedback as a source of shock motion that could not be accomplished by either conventional PIV or surface sensors traditionally used in turbomachinery tests.

More detailed analysis of data sets of this type was conducted by Klinner et al. [108] by employing spectral proper orthogonal decomposition (SPOD) [109, 110], which is a more recently developed spectral analysis technique that is adept at locating spatial distributions associated with various resonance modes contained within the time sequences. The spatiotemporal formulation locates coherent flow structures associated with specific frequencies present within the TR-PIV vector field sequences. Its potential is only beginning to find its way into TR-PIV analysis.

B. Pulse-Burst Lasers

The state of the art of TR-PIV in high-speed flows has been enabled by the advent of the pulse-burst laser (sometimes termed burst-mode lasers). This laser design is quite different than the traditional oscillator/amplifier design in PIV lasers, though the Nd:YAG medium still is used. A continuously pulsed diode-pumped solid-state laser is the light source but with very low pulse energy. The pulses are then repeatedly amplified through several stages of Q-switched Nd:YAG rods powered by either diode lamps or xenon flashlamps. This architecture is known as master oscillator power amplifier (MOPA) and has proven to be both versatile for a variety of applications and amenable to reaching very high pulse energies (10's to 100's of mJ at 532 nm) simultaneous with very high repetition rates (10's of kHz to MHz), usually constrained by financial resources rather than technology limitations. The primary drawback is a very low duty cycle wherein pulse sequences can last for only 10 ms every 8–12 seconds. This can produce a practical limitation when combined with the blowdown test facilities common in high-speed flows, therefore drastically curtailing data collection and statistical convergence. The design and use of pulse-burst lasers has been reviewed initially by Thurow et al. [111] and more recently by Slipchenko et al. [112]; much technical progression occurred in the only eight years between those reviews.

The formative work establishing pulse-burst PIV in high-speed flows was conducted at Sandia National Labs [114], often with the goal of collecting spectral content. The PIV system employed a pulse-burst laser (Quasimodo by Spectral Energies, LLC) to produce pulse pairs at 25–50 kHz and typically 20–50 mJ per pulse at 532 nm. Experiments captured light using two side-by-side cameras for a wider field of view (Photron SA-X2) producing frame-straddled pairs at 25 kHz, later graduating to a faster model (Photron SA-Z) to nearly double the readout rate. Seeding was accomplished using the same technology that had been established 15 years earlier for conventional PIV, in which particles were

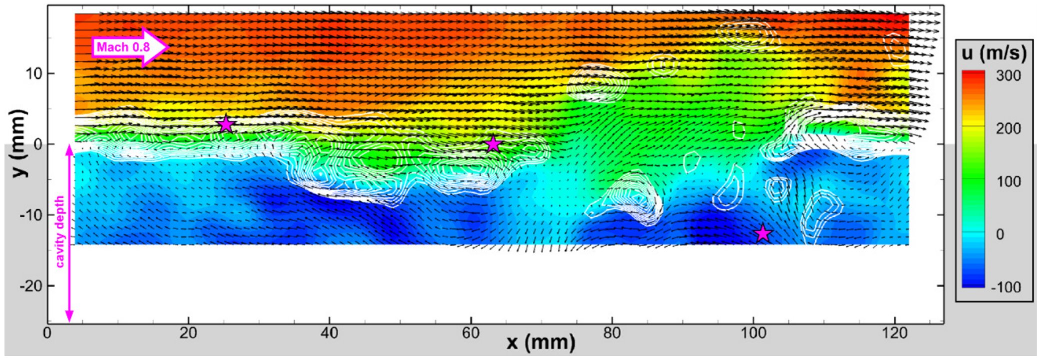

Fig. 28 A single velocity field extracted from a 10.2 ms pulse-burst PIV movie of transonic cavity dynamics acquired at 37.5 kHz. Color contours are streamwise velocity and white contours are vorticity. Stars indicate locations of data sampled in Fig. 29. From [113]

generated from a thermal smoke generator (Corona Vi-Count 5000) and ducted into the wind tunnel stagnation chamber through a manifold of injector tubes. In situ measurement determined a particle diameter of 0.7–0.8 μm, yielding a Stokes number estimate for most applications of no more than 0.05, which predicts negligible error due to particle lag.

One of the applications were initially used to develop the pulse-burst PIV system was the aeroacoustic environment of a rectangular cavity in transonic flow [113, 115], which is summarized here. A finite-width rectangular cavity was installed into one wall of Sandia's Trisonic Wind Tunnel (TWT) and the freestream flow was passed over it at Mach 0.8. The shear layer and recirculation dynamics form a feedback mechanism with aeroacoustic confinement within the cavity walls, creating intense resonance tones and high sound-pressure levels.

The pulse-burst PIV system was operated at 37.5 kHz and collected 386 velocity fields in 10.2 ms bursts. Pulse pairs were generated at this repetition rate with a time separation of 3.4 μs then frame-straddled onto successive images of each camera. The laser sheet was oriented in the streamwise/wall-normal direction and placed at the centerplane of the cavity. The cameras were angled to peer over the sidewall into most of the depth of the cavity. The mildly oblique view of the laser sheet creates a bias error in one velocity component but this does not hinder detection of the cavity resonances. Frame-straddled image pairs were interrogated no differently than for conventional PIV; here, an initial pass used 64×64 pixel interrogation windows, followed by two iterations of 24×24 pixel interrogation windows with a 50% overlap. Whereas previous conventional PIV measurements established the mean flow structure and its turbulent intensity distribution, the TR-PIV was used to spatially locate the resonance modes within the cavity.

An example of a single frame of the velocity field sequence is shown in Fig. 28. The full movie is available as supplemental media in [113]. The outline of the cavity is shaded gray and is coincident with the plot axes. Vectors show in-plane velocity fluctuations superposed on color contours of the streamwise velocity component. White line contours show vorticity to visualize large-scale turbulent structures at the shear layer interfaces. The strong dynamics of the shear layer and recirculation are evident, but signatures of resonance are not visually apparent in the movie sequences. The frequency content of the velocity fluctuations was found by extracting the time sequence of velocities at any vector location and calculating its power spectrum from the 250-burst data set. Three points in the flow were selected to represent different flowfield features and are indicated by the stars in Fig. 28.

The resulting power spectra are shown in Fig. 29 and are compared to a spectrum derived from pressure fluctuations recorded by a fast-response pressure sensor installed in the cavity's aft wall. Four acoustic tones are seen in the pressure spectrum, of which three are present in the shear layer velocity spectra and none in the velocity spectrum from the recirculation region. These differences are attributable to spatial variations in the presence of the resonant tones; these spatial maps are found in [113]. Modes 2–4 are concentrated in the shear layer and hence visible in two of the three velocity spectra. Mode 1 is associated with the recirculation region and therefore not found in the vectors extracted from shear layer. But neither is it apparent in the spectrum from the recirculation region; this region is dominated by intense turbulent motion, which subsumes the mode 1 tone found here. Also of note, the velocity peaks are broader than the pressure peaks because the limited PIV burst duration of 10.2 ms restricts the frequency resolution of the spectral transformation to 100 Hz, whereas the much longer record length of the pressure data allows a resolution of 10 Hz. This example analysis demonstrates the additional information available in both spatial and frequency domains by obtaining spectral content from TR-PIV data.

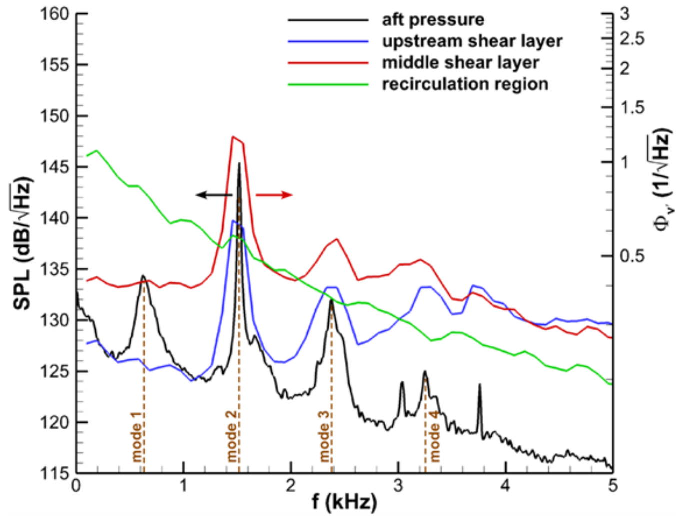

Fig. 29 Power spectra of velocity fluctuations (right axis) compared with spectrum from a pressure sensor (left axis) for the transonic cavity flow. Locations as per the star symbols in Fig. 28. From [113].

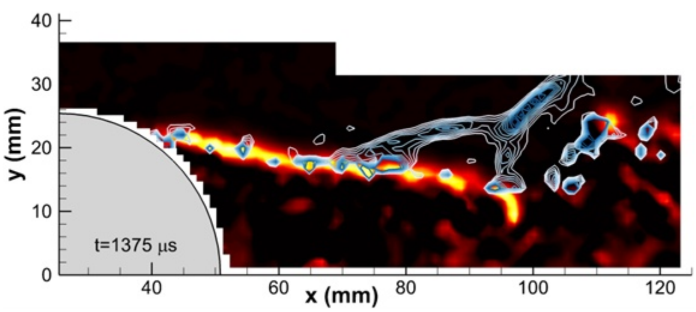

Fig. 30 A single velocity field extracted from a 40 kHz pulse-burst PIV movie of the unsteady wake of a wall-mounted hemisphere at Mach 2. Red-yellow contours show the shear layer via the vorticity field and blue-white contours show shock waves via negative values of divergence. From [116].

A subsequent experiment by the Sandia team pushed the pulse-burst PIV capability into the supersonic regime. Other groups have used pulse-burst laser technology to apply TR-PIV to the supersonic regime as well, including a shock/boundary-layer interaction at Mach 2 [117, 118], measurements inside a rotating detonation engine [119], and an extraordinary 5 MHz measurement of the flow behind a blast wave [120]. Pulse-burst PIV also have been implemented in shock tubes, measuring the dynamics of an impulsively-started wake of a cylinder [121] the passage of a shock wave through a dense field of large particles [122], and across a Richtmeyer-Meshkov instability [123, 124].

At Sandia, the turbulent wake of a hemisphere mounted on one wall of the TWT was measured at Mach 1.5 and 2.0 using the same pulse-burst PIV system with the goal of measuring the dynamics of the unsteady shear layer it sheds and the shock waves found there [116]. The laser and cameras were configured similarly to the cavity experiment except operated at 40 kHz and with time separation in pulse pairs of 1.8 μs. The side-by-side camera placement was used again but here no downward inclination angle was required for a view of the flow field. The laser sheet again was oriented streamwise/wall-normal along the centerline and images were interrogated in the same manner. A key difference from the cavity flow experiment is that only 26 bursts of vector fields were acquired, which impacts convergence of statistics and illustrates the drawback of the pulse-burst duty cycle.

A post-processed velocity field from one of the velocity movies is shown in Fig. 30; the entire movie is found as supplemental material in [116]. Rather than showing velocity vectors, the data use the vorticity field to visualize the shear layer (red-yellow flood contours) and negative divergence contours to identify shocks via compression of the flow (blue-white line contours). In the full movie, the shear layer flapping can be observed and the shock waves emanating from turbulent structures in the shear layer propagate downstream while the bifurcated shock feet repeatedly coalesce and break apart.

To examine the dynamics of the shock motion, the divergence field was sampled at the most common shock location over the data set. The power spectral density was found from this signal for both the Mach 1.5 and Mach 2.0 cases and is shown in Fig. 31. The results show that while there is much broadband content, the shock motion has a preferred frequency. When normalized, the peaks for each Mach number correspond to the same Strouhal number of 0.32. This discovery allowed characteristic shock motions to be formed using time-correlated conditional ensemble averages from the full data set, which revealed that counter-rotating vortex pairs from large-scale structures in the shear layer traveled with the shock motion and that a weak periodicity could be found in the shock and vortex behavior.

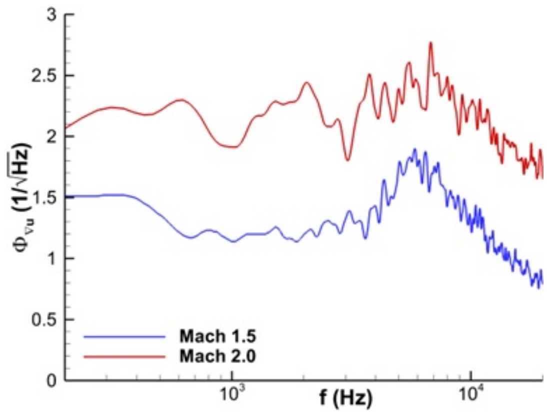

Fig. 31 Power spectra of the shock motion using the divergence field from TR PIV sequences such as Fig. 30. From [116].

C. High-Frequency Spectral Content

The expanding technical capability for TR-PIV in high-speed flows also is allowing it to move into application space previously served by hot-wire anemometers and Laser Doppler Velocimetry. By shrinking the field of view, the pulse energy available at high repetition rates is concentrated to provide sufficient scattered light to illuminate a small portion of the camera array operating at the highest possible framing rate. This essentially creates an “optical hot wire.”

In [125], the laser repetition rate was increased to 400 kHz and operated in a continuously pulsed (or time series) mode in which correlations were made between each successive frame rather than correlating the uniquely-paired pulses of frame-straddled mode. The much higher repetition rate required a substantial reduction in laser energy per pulse, to about 8 mJ at 532 nm. Meanwhile, the same Photron SA-Z camera used in the previous applications could be sped up to 400 kHz by windowing the camera array to only 128×120 pixels and a 11×11 vector field. This also meant the laser sheet could be reduced in size to concentrate the limited available energy. Sequences exceeded 4000 images in the available 10.2 ms burst duration. The very small size of the field of view and resulting vector field is not helpful for describing the flow spatially, as in most PIV applications, but it greatly increased the spectral content that can be acquired.

Tests of this very-high-frequency TR-PIV system were conducted for a supersonic jet exhausting into a Mach 0.8 crossflow in the TWT. The resulting power spectrum is given in Fig. 32, detecting both a -1 power-law slope for turbulent decay attributable to the scales of dominant turbulent eddies as the jet mixes with the crossflow, and also the onset of the well-known $-5/3$ slope of wavenumber spectral theory in the inertial subrange. The maximum detectable frequency is limited by the Nyquist criterion to 200 kHz, but in practice, this measurement did not exceed 120 kHz before encountering the noise floor. As a result, the $-5/3$ slope is poorly described.

To accurately measure the highest frequencies that can be delivered by pulse-burst PIV and to study the turbulent phenomena that motivate the technique, the framing rate was boosted to nearly MHz rates (990 kHz) [126]. Increasing the repetition rate of the pulse-burst laser was straightforward and the concomitant loss of energy was alleviated via alterations in the beam focus and duration through the second-harmonic generator, yielding 5.5 mJ/pulse. A faster camera newly available at that time (IX Cameras model 726) allowed MHz framing rates with pixel counts similar to the earlier use of the Photron SA-Z, though with some image artifacts that were found to be tolerable.

The increased TR-PIV framing rate provided oversampled data and enabled use of five-frame pyramid correlation to interrogate the image sequences, which dramatically lowered the noise floor. Figure 8 shows the MHz-rate spectrum analyzed using both conventional two-frame correlations and the pyramid correlation. With the greatly reduced interference from the noise floor, a region of roughly constant slope emerges beginning at about 80 kHz and extending to perhaps 250–300 kHz where the slope diminishes yet again. This latter effect appears to be the point at which spatial filtering due to the size of the interrogation window begins to impact the data, creating an effective frequency response of approximately 240 kHz.

The MHz-rate spectral content of Fig. 32 suggests that the high-frequency turbulent decay law is steeper than the theoretical $-5/3$, possibly because the isotropy and homogeneity assumptions underpinning the theory have not been achieved. This discovery would seem to justify the effort of acquiring MHz-rate data. However, a careful examination of the performance of multi-frame interrogation algorithms in spectral space suggested that they predominantly provide low-pass filtering of the correlation noise and only modestly increase the measurement bandwidth [127]. Similar filtering effects can be imposed on the temporal response by inadequate spatial resolution (e.g., [106]). Manovski et al. [128] rigorously analyzed the spectral response of 80-kHz TR-PIV and also showed that spectral features in space-time can become distorted due to instrument characteristics. Distinguishing legitimate physics from filtering effects in either the spatial or temporal domains can pose a challenge and employing more sophisticated algorithms is not an assured solution – they can create ambiguities rather than reveal physical insight. This is an active area of research and should motivate practitioners of high-frequency TR-PIV.

A pulse-burst laser is not necessary to measure very-high-frequency content in velocity fields. Spectral content at such high frequencies also has been achieved by experimental configurations employing high-repetition-rate continuously pulsed lasers, though in lower-speed flow regimes. Similarly to the pulse-burst experiments, such optical configurations also concentrated energy in a narrow sheet but the more benign flow environments allowed cameras to be placed closer to the laser sheet to collect more scattered light. Willert [129] was a pioneer in this regard, whose work was achieved concurrently with the Beresh et al. pulse-burst experiments. He measured turbulent fluctuations in a free jet at 30 m/s with only 20 μJ/pulse at 420 kHz. The resulting spectra distinctly revealed a power law very close to $-5/3$ over about two decades of frequency. Spectral response in a turbulent jet also was measured by Geschwindner et al. [130] at 400 kHz using a continuously pulsed fiber laser that delivered about 120 μJ/pulse. Continuously pulsed lasers can acquire a lot of data quickly whereas a pulse-burst laser is restricted by its low duty cycle, which can make an experiment labor-intensive to generate well-converged spectra.

Nonetheless, the steady growth in high-speed camera capabilities coupled with the versatility of pulse-burst lasers promises that soon high-frequency spectral content can be derived from TR-PIV measurements without undue loss of spatial extent, even in compressible flows. The potential for PIV to explore high-frequency spectral content has only begun to be realized.

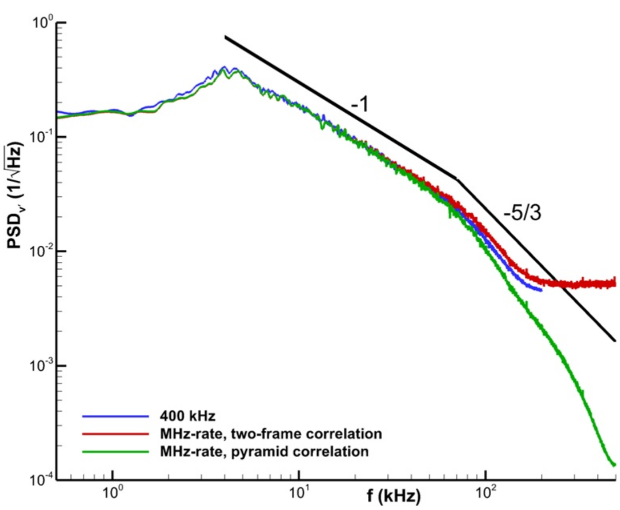

Fig. 32 Power spectra of velocity fluctuations in a supersonic jet exhausting into a transonic crossflow. MHz-rate measurements are compared to 400-kHz measurements, including use of the pyramid correlation on the MHz-rate data. From[125, 126].

VI. Adapting PIV from Supersonic to Hypersonic Flows

PIV has been successfully implemented in high-speed and supersonic flows for many decades, as detailed in several review articles that include a survey of applications of PIV to supersonic flows [131–133]. The challenges of applying PIV to hypersonics are the same as applying it to supersonic flows, except that the requirements become more stringent and difficult to meet. Nonetheless, a significant number of hypersonic applications can be found in the literature though often containing some deficiencies. Commonly, mean velocity fields distant from shock waves are successfully measured, but the particle time response is inadequate to measure turbulence or instabilities without inducing bias errors. Unsurprisingly, most hypersonic applications of PIV are conducted at Mach 5 or nearly so, which meets the generally accepted definition of this flow regime, and moreover are performed in cold-flow test facilities. However, many of the most important modern research problems to be solved involve higher Mach numbers and high-enthalpy effects. Few PIV applications are found for such flows and the prospects for implementation are uncertain.

A. Particle Response

The literature on particle response for PIV measurements is voluminous. It is not meant to be replicated here, but instead, this section offers an explanation of how hypersonic conditions exacerbate the challenges of particle seeding until they become intractable. Complete treatments of particle response for PIV data quality can be found in, for example, Raffel et al. [134] and Smith and Neal [135], or in seminal works by Samimy and Lele [136] and Melling [137].

The primary concern regarding particle seeding is particle response time, or particle lag. Of course, this must be considered in nearly every PIV application and is hardly unique to the hypersonic regime. The Stokes number, Sk, is a measure of the particle response time $\tau_p$to the characteristic flow time, τ_f and serves as a measure of how well the particles track the flow. The choice of an acceptable threshold for Sk is subjective and dependent upon what error levels are tolerable, but $Sk < 0.1$ is generally understood [136]. This should offer errors within approximately 1%, which is commensurate with the uncertainty found in PIV image interrogation. Others recommend a more conservative $Sk < 0.05$ to ensure less than 1% error (e.g., [135]).

Although τ_p can be estimated from particle characteristics, the effective particle diameter generally is not known well enough due to agglomeration in the seeding apparatus, nonspherical shapes, or overly optimistic manufacturer's characteristics; therefore, it must be measured *in situ*. This ordinarily is accomplished by measuring the particle response time across a shock wave via the exponential decay of its velocity, which is a simple experiment to conduct in a supersonic facility using the same PIV system intended for the actual experiment. A good description of this procedure is found in [138]. A more recent reassessment by Williams et al. [139] suggests that particle lag in the low-density environment of supersonic and hypersonic flows may be underestimated by the usual particle response measurement across a shock wave and therefore have even greater challenges than usually understood. This would mean that τ_p likely is larger than what is measured in a shock response experiment and therefore the Stokes number is larger.

An appropriate characteristic flow time, τ_f, must be estimated as well. This ordinarily is chosen by identifying a relevant length scale and a velocity difference over that distance, but there is no commonly accepted definition. Each PIV user must determine a time scale individualized to each flow. A boundary layer experiment might use the freestream velocity and boundary layer thickness, or a free shear layer experiment could choose the freestream velocity difference and shear layer thickness. In practice, most users opt for large-scale mean flow characteristics such as these because they are easily estimated when the experiment is being planned long before any PIV data are acquired.

But Beresh [106] cautions that this usual assessment of τ_f may mask the true particle lag. Even when the mean flow field is desired, PIV does not measure the mean flow. It measures instantaneous motion and then the mean is assembled from these samples. Therefore, to measure the flow field accurately, the particle response must capture these instantaneous motions, which invariably have more demanding requirements, and failure to do so filters out some of the energy contributing to even the large scales of the flow.

Beresh [106] provides an example of a cavity shear layer at Mach 2.5 in which the instantaneous turbulent time scales, even those at large scale, are an order of magnitude shorter than those estimated using the mean flow characteristics of the shear layer. Therefore, the true Stokes number actually is an order of magnitude higher. This example is replicated in Fig. 33. The velocity gradients found from the large scales of the mean flow field are estimated as 36,000 Hz, or a $\tau_f \approx 30\ \mu$s. Instantaneous velocity gradients are directly measured a posteriori from the flow itself as 350,000 Hz, or $\tau_f \approx 3\ \mu$s. From [136], this corresponds to approximately an order-of-magnitude increase in particle lag error. In practice, flows with a symmetric probability distribution of velocity fluctuations will not find their mean velocity field altered by a filtration of higher-frequency events. Conversely, turbulent stresses and the turbulent kinetic energy will be artificially suppressed.

All of these factors accumulate to suggest that the Stokes number required for a hypersonic experiment is harder to achieve than routine analysis would indicate, and that apparently successful measurements may harbor greater errors than recognized.

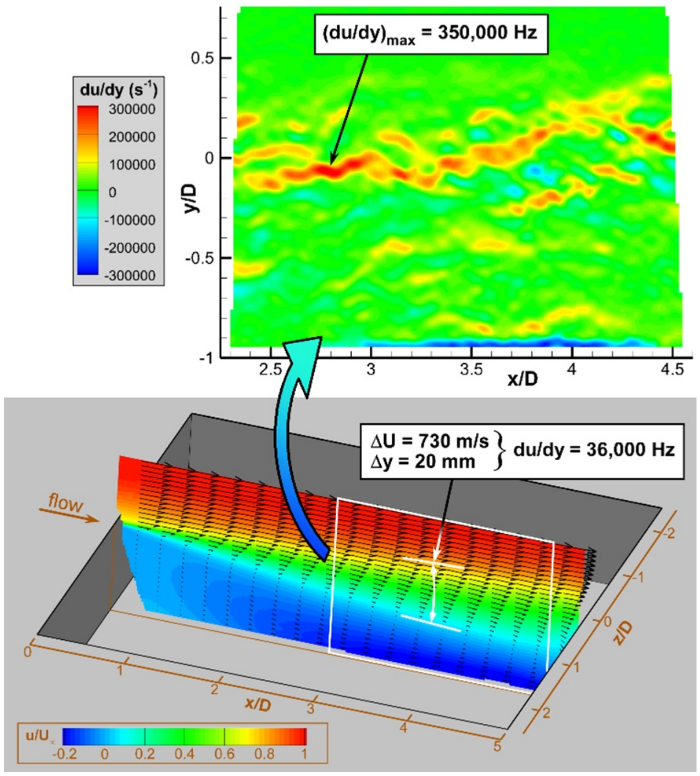

Fig. 33 Illustration of characteristic flow frequencies in a Mach 2.5 cavity shear layer; determination from the mean velocity field (bottom) and from an instantaneous vector field (top). From [106].

B. Particle Seeding

Other considerations regarding particle seeding also become more troublesome in the hypersonic regime. First, a prodigious quantity of particles must be delivered to a blowdown wind tunnel. The expansion of the flow through the wind tunnel nozzle disperses the particles. The density in the test section is 2–3 orders of magnitude lower than in the stagnation chamber, which intensifies the requirements placed on the seeder for delivery where hardware will not perturb the flow. This raises the cost and complexity of the hardware to achieve a reasonable particle density coupled with apparatus to reduce agglomeration (e.g., agitation of a fluidized bed and/or a cyclone separator stage). In practice, a hypersonic PIV experiment is likely to operate with a sub-optimal particle density.

Hypersonic blowdown wind tunnels require significant mechanical and electrical components to operate, which may not be tolerant of the presence of particles for PIV. At-risk hardware includes downstream valves and pumps, remote-actuated pitching struts, in-line electrical heaters, and delicate surface sensors on a test article. The continued health of a facility and model is a greater risk for operators of hypersonic wind tunnels than their low-speed or low-supersonic counterparts.

Many descriptions of the hardware for particle seeding already are available in the literature, including means of reducing agglomeration to minimize the particle size (e.g., [134, 137, 138, 140]). Most high-Mach-number facilities have opted for powders, either silicon dioxide (SiO_2) or titanium dioxide (TiO_2). Although oil-based particles are effective in transonic and low-supersonic facilities, they do not translate well to hypersonic facilities because they are difficult to inject into high-pressure stagnation chambers and they may be flammable at the high temperatures found there [141].

Nonintuitively, short-duration shock tunnels or Ludwig tubes are easier to seed than blowdown wind tunnels. Particles are seeded into the quiescent test gas before the facility operates, which can occur at a leisurely rate and does not require seeding apparatus of large capacity. A modest air current while awaiting shock tunnel operation can help keep particles suspended and dispersed, then turned off just prior to running the facility. Although this solves problems regarding the complexity of seeding hardware, the limitations of the particle response time and flow expansion through a nozzle are no different than in a blowdown wind tunnel.

Seeder designs for supersonic and hypersonic flows have emphasized reduction in particle size through a variety of approaches. Ragni et al. [138] surveyed common particles used for PIV in high-speed facilities, a list that has not appreciably changed in the intervening 15 years. They found that commonly used powders and seeding generators ordinarily did not produce a particle response time much below 2 μs. But with more heroic efforts, they pulled the response time down to 0.36 μs. However, the filtering and dehydration and cycloning may be too intensive for routine operation in larger testing facilities.

Ghaemi et al. [142] made the first identified attempt to introduce nanoparticles into a wind tunnel, but they achieved a time response of 0.27 μs, which is only a little lower than the best efforts found in Ragni et al's survey. However, the particle quantity was suboptimal even in this small wind tunnel and it did not show promise for scalability. A different nanoparticle approach has been developed by several groups in China using dehydrated TiO_2 particles via a fluidized bed generator [143, 144]. The originating effort by Zhao et al. [143] claims in situ particle diameters of 42 nm and response times of 66 ns, but subsequent efforts measured 1–2 μs response times [144, 145]. The resulting velocity data sets are intriguing but warrant further confirmation [145–147].

The ideal particle may be something hollow, porous, or spiny, any of which would raise the light scattering cross-section and the drag while reducing its mass and therefore inertia. However, such shapes may result in a more abrasive particle that would be more prone to damaging or impairing downstream machinery. These same irregular shapes may make them more prone to agglomeration or difficult to move through seeding apparatus. Producing them in large volume and affordably adds to the engineering challenge. The present authors are unaware of any serious efforts to develop a better particle on the scale needed for implementation in a hypersonic wind tunnel.

All of these practical considerations may prove daunting for PIV practitioners and hypersonic wind tunnel operators, thereby motivating investment into more tractable diagnostics. This is particularly the case if programmatic motivations demand a Mach number well in excess of the hypersonic threshold of Mach 5. The return on investment for PIV ultimately is limited by the particle response.

C. Examples and Limitations of Hypersonic PIV

Despite all the hurdles to surmount, several researchers have successfully gathered PIV data in hypersonic flows, though perhaps with limitations. A first test of PIV in hypersonic conditions was conducted by Humphreys et al. [148] in 1993, seeding Al_2O_3 particles into a Mach 6 blowdown wind tunnel and obtaining five images on film of particles traversing an oblique shock. This effort was little more than a demonstration of particle response. Havermann et al. [149] later made several tests in a shock tunnel using Al_2O_3 particles at Mach numbers of 4.5 and 6, culminating in measurements through the bow shock generated by a sphere.

The first unambiguously hypersonic PIV application to investigate flow physics rather than just demonstrate particle response probably is Schrijer et al. [150], in which they measured the flow over two different biconic geometries at Mach 7 in a Ludwieg tube. The flow was seeded prior to operating the facility by introducing TiO_2 particles through a cyclone into the storage tube, which remained suspended by the time the facility was fired. Particle response across a shock wave indicated a response time of 2.5 μs but images suggested significant centrifuging occurring in the separation region downstream of the shock interaction. Nonetheless, average velocity fields such as the one shown in Fig. 34 were a good match for the shock shapes found in schlieren images, including quantitative comparisons of shock angles. PIV even has been implemented in a large-scale shock tunnel in a high-temperature Mach 6 flow using naturally occurring dust particles, though the particle response was not defined [151].

A series of experiments [152–154] in the Princeton Mach 7.2 wind tunnel took on the greater challenge of measuring turbulence statistics; their results have returned valuable data despite acknowledged particle response errors. The wind tunnel was seeded with dehydrated TiO_2 particles, which from shock-response data were found to have an agglomerated diameter of 2 μm and a response time not better than 10 μs. Considering local flow conditions throughout a boundary layer, the Stokes number was estimated to be as high as 1.2 even in the outer layer [153]. Despite the filtering effect that must result from such large particle lag, mean velocities were shown to agree well with accepted log-law and law-of-the-wake fits. Turbulent stresses were a different matter, as reproduced in Fig. 35. Streamwise turbulent stresses formed a surprisingly good match with a DNS simulation and an incompressible reference, and three different experimental Reynolds numbers revealed plausible trends. Conversely, magnitudes of the wall-normal turbulent stress

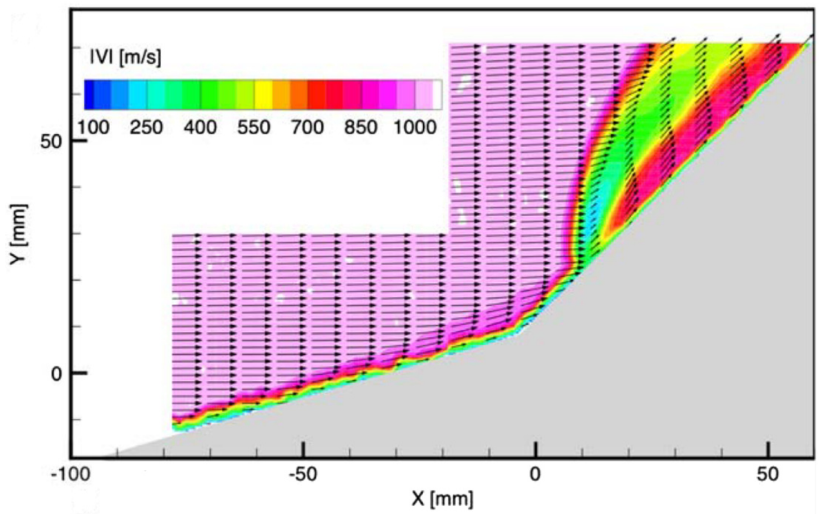

Fig. 34 PIV velocity field in a Mach 7 Ludwieg tube over a biconic geometry with a compression angle of 30 deg. From [150].

and the turbulent shear stress were greatly suppressed in comparison to the DNS and incompressible experiment and distinctions between Reynolds numbers were undetected. Similarly, measurements of a shock/boundary-layer interaction using the same PIV system in the same wind tunnel also showed that particle lag impacted the wall-normal turbulence statistics far more than the streamwise component [154]. Neeb et al. [155] conducted Mach 6 boundary layer measurements on a sharp cone in a different facility, also using TiO_2 as particles and a Stokes number as large as 1, and they found suppression not just in the wall-normal turbulent stress but also the streamwise direction.

Thus far, the definition of "hypersonic PIV" has been based on the freestream Mach number. But it is worthy to recognize that many propulsion experiments for hypersonic flight are conducted at lower Mach numbers reflective of the flow velocities within a representative scramjet duct in what are known as "direct connect" wind tunnels. The high-temperature environment in such facilities adds a challenge for particle seeding and successful imaging that offsets the reduction in particle response requirements. Examples of such experiments include Tuttle et al. [156] and Rice et al. [157].

Summarizing this brief survey of hypersonic PIV applications, sufficient examples exist to demonstrate its feasibility despite the lack of a novel particle that eliminates response issues. Mean velocity data have been shown to be reasonable but turbulent statistics are clearly flawed due to the suppression of measured velocity fluctuation magnitudes owing to the particle lag.

D. Alternative Velocimetry Techniques

Given that hypersonic PIV has proven limited due to particle response and that no viable solution appears imminent, researchers have been developing alternatives for decades that are not based on particle tracking. Historically, some interest existed for Filtered Rayleigh Scattering, also known in various implementations as Planar Doppler Velocimetry or Doppler Global Velocimetry, but recent momentum is centered around Molecular Tagging Velocimetry (MTV) techniques, specifically Femtosecond Laser Electronic Excitation Tagging (FLEET) and Krypton Tagging Velocimetry (KTV).

A brief note is warranted about "schlieren imaging velocimetry" and related techniques. These employ double-frame or time-sequence schlieren imaging and correlate upon motion between successive frames. The same approach can be achieved using Background-Oriented Schlieren (BOS). While this appears to be a useful shortcut to obtain flow velocities, in practice this returns convection velocities of structures within the flow rather than the local flow velocities that PIV would measure [158]. See Raffel [159] for a more complete discussion.

MTV encompasses a broad class of diagnostics that serve applications from low-speed liquid flows to hypersonics and many examples in between. Their commonality lies in an ability to use a laser to write a point or a line or a grid into the flow with a finite duration that can be tracked in time, typically using a molecular excitation that will lead to fluorescence. A good summary pertaining to hypersonics is given by Danehy et al. [133]. Historical examples

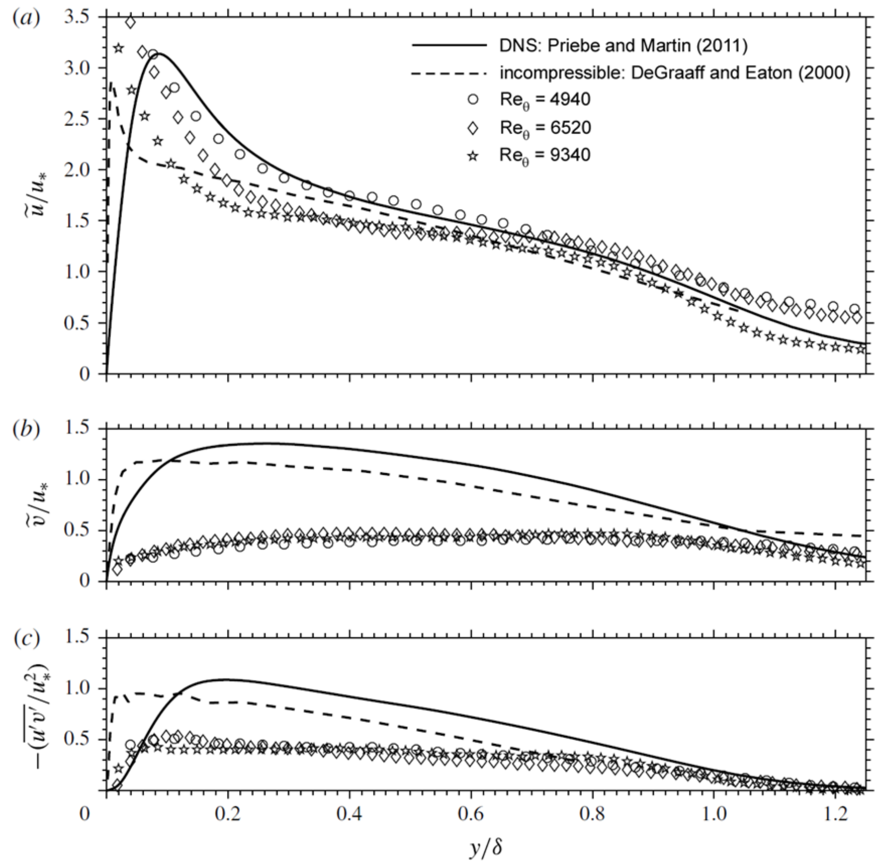

Fig. 35 Turbulent stresses from PIV in a Mach 7.2 boundary layer; (a) streamwise turbulent stress; (b) wall-normal turbulent stress; (c) turbulent shear stress. From [153].

in hypersonics involved a great deal of complexity and expensive equipment, but the recent development of FLEET provides a path towards a production measurement in widespread use. By leveraging the properties of femtosecond time-scale lasers, the complexity of the measurement is greatly reduced. The commercialization of femtosecond lasers has made their use almost as straightforward as the lasers routinely used for PIV. FLEET requires only a single laser, a single camera and intensifier (though multiple camera angles are beneficial), and no seeding of toxic gases into the wind tunnel – and no risk of particle lag. By the time of the present article, it has spread to at least half a dozen hypersonic facilities. A thorough review of the technique is provided by Danehy et al. [160].

Perhaps the best marker of FLEET's utility for hypersonics is provided by Dogariu et al. [161, 162], who successfully measured mean boundary layer profiles at Mach 10, 14, and 18 in the AEDC Hypervelocity Wind Tunnel 9 in White Oak, MD, a large-scale production wind tunnel with a test section diameter of 1.5 m. More recent experiments in Sandia's Hypersonic Wind Tunnel by Senior et al. [163] further demonstrate the capability of FLEET to measure hypersonic boundary layer turbulence. They showed the mean streamwise velocity and the streamwise turbulent stress in the boundary layer of a sharp cone at Mach 8 sweeping Reynolds numbers from laminar conditions through transitional cases and finishing at fully turbulent conditions.

A different MTV technique with some recent use in hypersonics is Krypton Tagging Velocimetry (KTV). The principle of the method is much like FLEET but instead the fluorescence is generated by seeding a small amount of krypton gas (about 1% mole fraction) into the flow and illuminating it with ultraviolet light from a Nd:YAG-pumped dye laser or optical parametric oscillator. First demonstrated by Parziale et al. [164], once again the utility of KTV is well confirmed by demonstrations in Tunnel 9 [165, 166], among others. Also of note is a revival of NO MTV in a high-enthalpy shock tunnel in which the Nitric Oxide is naturally present at high temperature rather than requiring seeding [167] and a new implementation simplifying the laser and optical configuration [168].

VII. Omnidirectional PIV

A. Abstract

Aerodynamic problems mostly deal with the interaction of an object with a fluid stream and the disturbance to the flow is often concentrated at the object proximity. This section describes methods intended to overcome the challenge of measuring three-dimensional (3D) flow fields around complex geometries, or when the object position is along with the experiments. An innovative approach for 3D PIV is proposed that combines several illuminators, whereby shadows are practically eliminated. Similarly, a multitude of imagers (typically 6 to 12) provide simultaneous 3D particle detection in the flow domain "tuttotondo" (i.e. all around the object). Such layout is referred to as Omnidirectional PIV (Omni-PIV). The main principles of this technique are discussed, which include Object Registration, Camera Coverage Rank (Rc) and Object Aware Lagrangian Particle Tracking (OA-LPT). A modular, scalable system comprises cameras arranged over pre-calibrated structures, denoted as "antennas", enabling flexible re-configuration and comprehensive optical coverage. Experiments are conducted around a scaled cyclist model. Results demonstrate the capability of Omni-PIV to provide a complete 3D velocity field around and in proximity of the object, even in the presence of significant occlusions to each of the illumination and imaging devices.

B. Introduction

In the visual art of sculpture, tuttotondo indicates a full three-dimensional realization, as opposed to a relief portraying only a side of the scene. Transposed to the domain of flow diagnostics, tuttotondo signifies the visualization of flow behaviour (by streamlines, velocity or pressure) around a specific object. The latter is of use in many practical applications of aerodynamics, notably for aircraft, ground vehicles, wind engineering, sports and bio-aerodynamics, among others. Full 3D measurements around an object are useful to the thorough understanding of the flow topology, but also to extract loads and forces by integrating, momentum, pressure and skin friction.

Particle Image Velocimetry in its stereoscopic layout [169] has been largely used for flow measurements where the 3D domain is sampled at discrete planes [170]. Instantaneous 3D-PIV measurements have been practiced with tomographic-PIV (Tomo-PIV, [171]), yet at a limited scale, due to the measurement volumes size constraints from tracers, illumination and imaging systems. Measurements over a larger measurement volume, in the cubic meter scale, were made possible with the introduction of Helium Filled Soap Bubbles (HFSB, [172]). Furthermore, advanced particle reconstruction and tracking methods such as the Iterative Particle Reconstruction (IPR, [173]) and Shake-the-Box (STB, [174]) have paved the way to the current state-of-the-art in terms of 3D velocimetry.

When imaging is hampered by the presence of optical occlusions. In the latter case a naïve solution is that of increasing the number of imagers, yet the particle detection algorithm logics is challenged by partial camera line-of-sight blockage as discussed in detail in the work of [175].

The coaxial volumetric velocimeter maximises the overlap between illuminated and imaged domain [176]. Coupled with a robotic arm [177] the method has proven capable to represent the flow field around complex objects at tuttotondo. The complete 3D flow field around the object is mapped by the movement of an articulated arm holding the optical head of the co-axial velocimeter. As a result, versatility is achieved, at expenses of the instantaneous capture of the velocity field.

Recently, [178] proposed an extension of 3D particle detection by including in the triangulation algorithm knowledge of the lines of sight blocked by the object. The latter requires precise information on the 3D object shape, size and position within the measurement volume, which is achieved with procedures of object registration [179]. Combination of the above has led to the object-aware Lagrangian particle tracking technique (OA-LPT), which solves the paradox "more cameras == less spatial coverage". Using OA-LPT the ray-tracing algorithm maps the regions covered by specific cameras over the measurement volume and incorporates the information for the particle triangulation logics, effectively dealing with the measurement volume erosion problem reported in the work by [175].

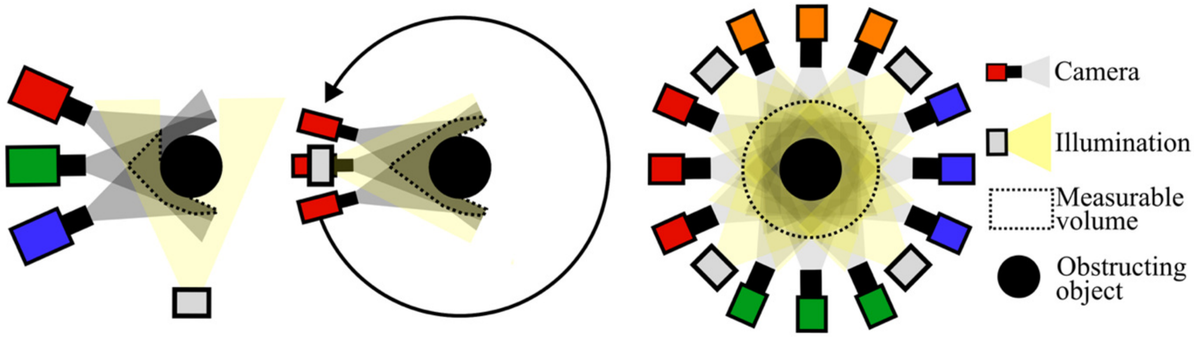

Fig. 36 3D PIV illumination and imaging around an object. Conventional system (left), co-axial configuration (aka robotic volumetric PIV, middle) and Omni-PIV layout (right).

Using OA-LPT, an omni-directional (from all directions) approach for measuring the flow field around 3D geometries using 3D-PIV is proposed here (Figure 1-right). Different from robotic-PIV, the optical coverage around a complex or moving object is achieved through increasing the number of simultaneous imaging and illumination directions, to the point where a single layout can deal with a multitude of geometrical conditions. The following paragraphs describe the realization of an Omni-PIV system and discusses the principles of operation, from the hardware assembly to the calibration and operations in aerodynamic wind tunnels. Results from aerodynamic experiments are described to illustrate both the principles of operation as well as to illustrate the type of databases produced with this technique.

C. Working principles

The hardware layout of an Omni-PIV system remains static during the measurements. Furthermore, it does not intrude the flow field compared to the robotic velocimeter. The large tomographic aperture results in isotropic sensitivity and spatial resolution. Achieving global optical coverage of the measurement volume around a complex object requires the deployment imagers in the order of 10-20 with 2-4 illumination directions. The goal of an Omni-PIV setup is to provide redundancy in both the number of imaging and illumination directions such that 3D particle tracking measurements can be performed around arbitrary geometries.

1. System calibration

A modular imaging system operates ten cameras clustered into "antennas" comprising 5 cameras each. Such antennas are pre-calibrated and can be regarded as 3D imagers. Intrinsic calibration for each antenna yields the field of view and the imaging magnification field. Such calibration is obtained simultaneous to the 3D calibration of antenna (by reference object or plate). The 3D calibration returns the object-to-image relation for the antenna. Antennas coupling is needed as each antenna can be freely placed around the scene to capture optimally the flow field around the object. This operation turns the system from partitioned into a monolithic [179] systems, based on antennas that are coupled as to work as a single ten camera system. The approach provides the flexibility to change the relative position of antennas or add additional ones either to increase coverage or to extend the domain of interest. Finally, once in operation, any residual disparity between the lines of sight is accounted for using the volume self-calibration technique [173]. A description of the hardware and its implementation into two independent antennas is provided in the section describing the experiments.

2. Object detection and reconstruction logics

Object detection techniques have been discussed in the recent work of [179], whereby an object of known shape and size (e.g. by means of a CAD model) is marked and recognized with a point-cloud correlation algorithm. Detection of markerless objects requires instead their illumination by a laser pointer, effectively producing the point-cloud in a sequence of images. Once that the object position is assessed in the measurement domain, a ray tracing algorithm determines the interruption of the views due to optical blockage from the object. This technique avoids that the strict logics of "no particle image ⇒ no 3D particle reconstruction" hampers the reconstruction of tracers in regions partly obstructed to a subset of views. The algorithm has been efficiently implemented in the Shake-the-Box method [174] and named object-aware reconstruction (OA-STB, [178]).

3. Seeding, illumination and imaging

The flow is seeded with flow tracers. In aerodynamic experiments, volumetric measurement conditions are reached by use of helium filled soap bubbles inserted in the settling chamber of the wind tunnel. Such systems require a multitude of bubble generators to achieve production rate in the order of 10^8 bubbles/s. For experiments in water flows, the tracers are commonly circulated within the closed-loop facility. Illumination is commonly provided by LED arrays from at least two directions (37-left). The illuminated tracers must be in view by three or more cameras for 3D triangulation. to minimize the occurrence of false triangulations (ghost particles, [180]). Additionally, the tomographic aperture (i.e. the angle subtended by the lines of sight) should be kept above 40 degrees for triangulation accuracy [181]. Figure 1-left illustrates the typical layout for 3D PIV measurements, the measurement domain is significantly smaller than the individually illuminated and imaged components. The co-axial approach (37-middle) does yield a larger overlap of illumination and imaging, at the cost, however of lower aperture, in turn depth precision [176]. The Omnidirectional system (37-right), multiplies the illuminators and imagers, potentially returning a global coverage of the flow field around the object.

D. Experimental setup and procedures

Current experiments are performed using an Omnidirectional PIV system organised with two antennas, comprising 5 cameras each. The measurements are conducted around 3D geometries at the low-speed aerodynamic wind tunnel (W-tunnel) of the Delft University of Technology. The hardware and design of antennas, illumination, calibration procedure and objects features are described below. Data acquisition, image pre-processing and interrogation follow.

Fig. 37 Antenna consisting of five cameras in a cross configuration and Test objects: wall mounted GCM.

1. Antenna calibration and coupling

A prototype omni-PIV setup is designed in the form of two antennas consisting of five cameras each. The cameras with 1628 ×1236 pixel resolution are LaVision Imager LX have making use of a CCD sensor with 4.4 μm pixel pitch. The five cameras with 25mm lenses are forming a single 3D-PIV antenna are oriented in a cross configuration with width and height of 1 m as depicted on the right of Figure 5-right. The cameras are installed on a cross-like metal structure, in turn mounted on a tripod as shown in Figure 37 and ran at 8 Hz double frame rate. The cameras are pointed to intersect at an operating distance of approximately 1.6 m. No use is made of Scheimpflug adapters, given a focal depth exceeding 1 m.

The tomographic aperture of in a single antenna is approximately 35°. With the 25 mm focal length lenses, a single antenna captures particle tracers in a measurement volume of approximately $40(X) \times 30(Y) \times 40(Z)\,\mathrm{cm}^3$. Even though the relative angles and positions between cameras in an antenna are fixed, the tripod mounts allow for change of the overall orientation of the antenna through two rotational degrees of freedom of the structure onto which the cameras are mounted.

Calibration of camera sets is an essential part of any 3D-PIV experiment. The calibration describes the lines-of-sight in 3D space traced out by each individual pixel on any of the cameras in the imaging setup, relating image space to the 3D object. The pinhole model [182] is defined by a set of intrinsic and extrinsic parameters. Intrinsic parameters describe the geometry of the camera + lens combination as they include information on the focal length, shape of pixels and center point of the image sensor. Extrinsic parameters, define the location and orientation of each camera with respect to the world reference system and therefore include three translation and three rotation parameters. Determining such parameters is performed by presenting a pattern with known shape and spacing to each of the cameras, commonly involving a planar plate with a markers. The plate is imaged at different positions and orientations throughout the measurement volume, simultaneously in view by multiple (not necessarily all) cameras.

For omnidirectional imaging, establishing a single view for all cameras might be unfeasible due to wide aperture of the overall system or due to the presence of an obstructing object. To circumvent this limitation, the calibration procedure is split into two stages: 1) individual antennas are 3D calibrated with the reference plate; 2) a sequence of images each containing a single dot is acquired, by use of a micro-LED, which produce the same 3D cloud pattern in the different antennas. The latter are coupled (i.e. a relative transformation of their coordinate reference systems) by matching such point cloud with a correlation technique. The obtained calibration one for individual antenna is illustrated in Figure 38. Furthermore the point cloud seen from the two antennas is shown from As the antennas are calibrated independently however, both calibrations define the cameras in a different coordinate system in which the relative position of other antennas are unknown. To combine the calibrations and allow for antennas to operate as a single 3D-PIV system a coupling step is performed.

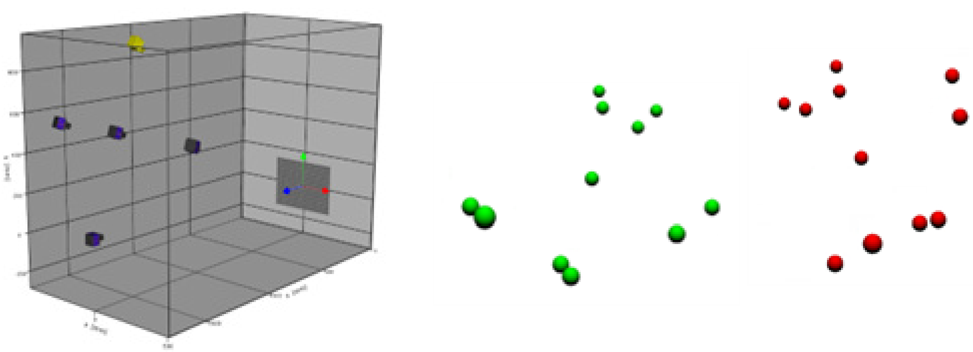

Fig. 38 (Left) result of one antenna calibration and (right) point clouds from the two antennas.

A small light source (micro-LED) is moved across the measurement volume and images are acquired simultaneously with both antennas. The position of the light dot is obtained for each antenna using the IPR algorithm [173]. The choice of a single dot in the scene is made to avoid any ambiguity in the identification of the triangulated LED position between antennas whilst also allowing to relax triangulation parameters. Furthermore a single marker is reconstructed with no risk of ghost formation, even when imaged by only two cameras.

The point clouds reconstructed from each antenna are displayed in Figure 38-right. The known correspondences between the triangulations is used to find the rigid spatial transformation (4×4 matrix including three translations and rotations) between the two sets in a least squares sense using the Singular Value Decomposition technique. After this procedure, the antennas are coupled and the system operates as monolithic.

2. Test object

Two test object is considered in the present experiment is a 1:8 scaled (22 cm length) generic cyclist model (GCM, [183]), as shown in Figure **??**. The generic cyclist model is produced with stereolithography (SLA) 3D printing. Both objects are painted matte-black as to reduce the intensity of reflections from the LED illumination.

3. Experimental setup

Experiments are performed in a low-speed open jet wind-tunnel, featuring a $60 \times 60\,\text{cm}^2$ cross-section. A top view of the experimental setup is shown in Figure 39. A 120 cm long flat plate, with elliptical leading edge is installed at the exit. The flow over the plate is forced into turbulent with a tripping device. In the center of the plate, at a distance of 50 cm, a 40 cm circular insert hosts the test object allowing a yaw rotation. The PIV antennas, are positioned at opposite sides of the wind tunnel aiming at the object at operating distance of approximately 1.6 m. The achieved measurement volume is approximately $40 \times 30 \times 40\,\text{cm}^3$. The measurement volume is illuminated from four sides using four LaVision flashlight-300 LED arrays. Helium Filled Soap Bubbles (HFSB) of 0.4 mm mean diameter are used as flow traces. They are introduced in the settling chamber by a 200 nozzle seeding rake illustrated in Figure **??** (second from left). At a free stream velocity of 10 m/s, the spatial concentration of HFSB is approximately 0.5 bubbles/cm^3.

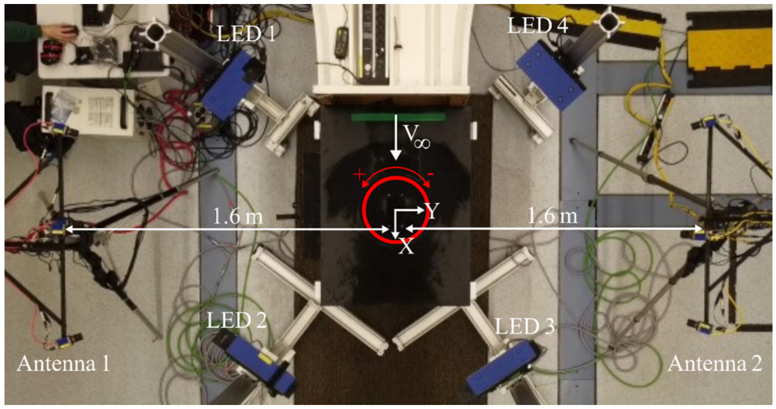

Fig. 39 Experimental setup (top view), with the two PIV antennas, four LED arrays and the flat plate with rotating insert hosting the test object.

4. Measurement conditions and procedures

Measurements are performed at a free-stream velocity of 8 m/s, yielding Reynold's numbers of 50,000 respectively, baased on cyclist torso length of 90 mm. Recordings are collected at a rate of 8 Hz in double-frame mode and analysed with the two-pulse STB algorithm [181] available from the DaVis 11 software. The LED illumination features pulse duration of 25 µs and the time separation between the two exposures is set to 250 µs, resulting in 10 pixels particle image displacement in the free stream. Each measurements comprises 5,000 recordings. The the GCM is set at a yaw $\beta \in [-20^\circ - 20^\circ]$.

Fig. 40 Triangulated dots from the GCM surface optical marking (left); matched digital (CAD) model (right).

Prior to each velocity measurement a set of images is acquired for the purpose to accurately determine the object position and orientation (object registration). In a dark environment, the object is marked with a pattern of laser dots and 50 single frame images are recorded. Details of the procedure are discussed in [179]. An example of the acquired surface measurements and an object registration of the cyclist model are shown in Figure 40. The digital object representation allows for 3D mapping of the optical camera coverage within the measurement volume. This is used in the OA-STB interrogation of the recordings [178]. Using OA particle tracking, an average of 25,000 particles is detected at each snapshot.

E. Results

First the achieved optical coverage is illustrated and discussed. The 3D (time average) flow field around the cube is visualized as to demonstrate the measurement coverage stemming from the omnidirectional approach.

1. Camera coverage

The goal of an omni-PIV setup is to provide sufficient coverage from multiple directions of illumination and imaging as to extend the measurable volume around possibly complex 3D geometries. As shown and discussed in section 2; for a part of the volume around the object to be considered suited for 3D particle tracking measurements, it needs to be in view by a minimum of 2 cameras and be illuminated from at least one direction. In order to visualize to what extent the volume surrounding the objects of interest are covered sufficiently for 3D-LPT, individually measured particles have been colored by the number of cameras that were involved in their triangulation. For this, OA-PTV is used in which the number of cameras considered for particle tracking is adjusted dynamically depending on the known lines of sight with respect to the object within the measurement volume. This is crucial for an omni-PIV setup as it avoids the erosion of the measurable volume by a stiff logics for particle detection in combination with object induced partial camera occlusion [178].

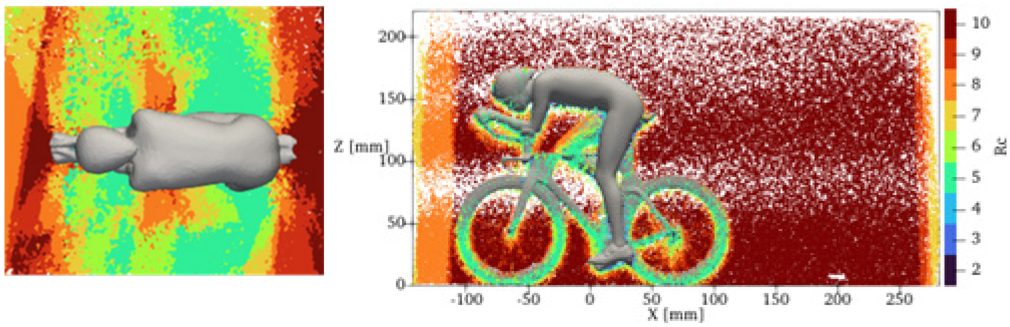

Fig. 41 Camera coverage rank (R_c) of triangulated flow tracers around GCM at 0 and 20 degrees of yaw. Top view (left) and side view from a 25 mm thick slab of the domain.

In Figure 41 the distribution of R_c for the GCM geometry at $\beta = 0°$ and $\beta = 20°$ is shown. Triangulated particles over 100 timesteps are accumulated and visualized in a 25 mm thick slab (yellow highlight). The number of cameras participating the triangulation is referred to as the camera coverage rank and denoted by R_c. Upstream and downstream of the object particles are triangulated by most cameras, while on the sides R_c reduces to half the number. Especially on the right of Figure 40 it is visible how the thin frame of the bike and the wheels create an outline of the bike in which the camera coverage rank drops abruptly from 10 to 5. From below the torso up until the chest surface, the coverage somewhat gradually decreases from 10 down to 3, given the intricate geometry of the cyclist and the bicycle, leading to small regions where a minimum is attained ($R_c = 2$). Varying the yaw angle does not introduce major differences in the coverage rank, indicating that the two-antenna system compensates the geometrical differences with sufficient redundancy not to introduce additional gaps when the object is rotated. The latter is a marked advancement compared to the situation discussed by [175], where the rotation of the object progressively degrades the domain coverage.

2. Velocity field

As shown in the previous section, the achieved optical coverage around the wall-mounted cube object allows for particle tracking measurements in a 3D volume extending up to the object solid surface. Accumulation of tracked particles over the full 5000 snapshots is used for a 3D binning to yield the time-averaged 3D velocity field. For the binning, the ensemble averaging approach as described by [184] is used. Cubic bins with a size of approximately 10 mm are used with an overlap ratio of 75%. A second order polynomial is used to fit the velocity measurements within each bin.

Figure 42-left illustrates the streamwise velocity distribution at the mid plane ($Y = 0$ mm) by colour contours. Stagnation is visible at the rider's hands and helmet. The flow accelerates past the helmet and forms a small pocket of recirculating flow between the back of the neck. No visible separation is observed until it the flow reaches far down the lower back of the cyclist where the largest reverse flow region is visi-ble. The vortical structures visualized in the 3D iso-surface 42-right provide insight of the com-plex flow arrangement around the athlete. Two counter rotating vortices extend from neck towards the back as reported in [183], and referred to as helmet vortices. The largest counter rotating structures extend from underneath the cyclist torso towards the lower back and reported as hip vortices. Minor systems of vortices are produced at several appendices of the body, tibia, ankle and foot. A comparable description of the complex flow field around this articulated geometry had required in the past the use of robotic PIV ([177]) by means

of 400 independent repositioning of the robot and is here reproduced with the omnidirectional PIV arrangement of cameras and illuminators.

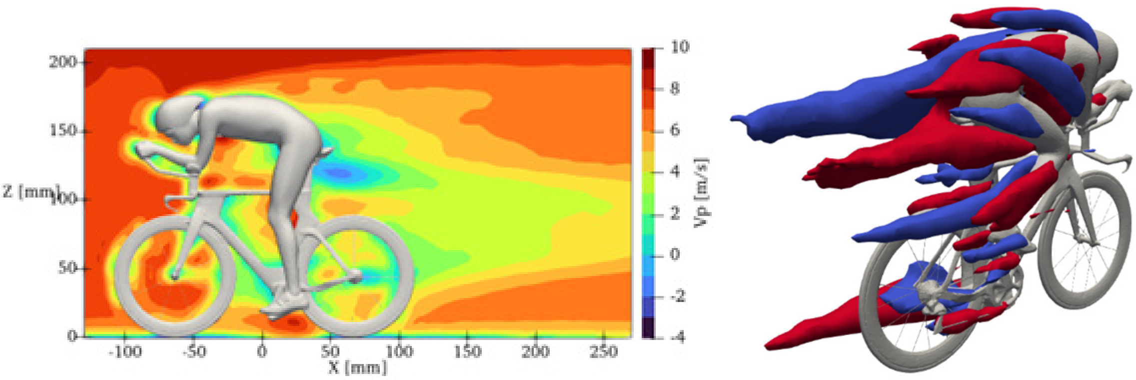

Fig. 42 Omni-PIV 3D flow measurements around the generic cyclist model at $\beta = 0°$. Visualized in a centered X-Z plane (left) as well as 3D vorticity iso-contours (right). Plane colored by free stream parallel velocity component and iso-contours shown at free stream parallel vorticity.

F. Conclusion

PIV measurements around large-scale, complex 3D objects require a multiplication of illumination and imaging directions, which drastically increases the complexity of the experimental setup. Addition-ally, if not properly accounted for, the optical occlusions due to the presence of the object in the scene might have the counter-intuitive effect of measurement volume erosion when the number of views is increased. The novel concept of omnidirectional Particle Image Velocimetry (omni-PIV) is introduced with the purpose to render 3D PIV measurements more resilient to the presence of the object and for the general treatment of arbitrarily complex geometries. The method combines the recent concepts of object registration and Object Aware Lagrangian Particle tracking (OA-LPT) with that of PIV-antennas. A prototype system is devised consisting of ten PIV cameras arranged onto two independently functioning antennas, each hosting five cameras. The calibration is split into two steps, whereby each antenna is calibrated prior to the experiment, followed by a coupling procedure based on a single mi-cro-LED waved in the measurement domain, yielding a monolithic three-dimensional measurement system. Experiments of the 3D flow field around a scaled cyclist model show that the amount of viewing directions provide already sufficient optical coverage for reliable particle reconstruction ($R_c \sim 5$) in the majority of the domain. Rotation of the object does not require adjustment of the illumination, neither of the imagers, indicating robustness to dynamical experimental conditions. The time-average flow field reconstruction enables the analysis of the physical behaviour, capturing most relevant features such as flow stagnation and separation lines, vortices and reverse flow.

Acknowledgments

Sandia National Laboratories is a multimission laboratory managed and operated by National Technology & Engineering Solutions of Sandia, LLC, a wholly owned subsidiary of Honeywell International Inc., for the U.S. Department of Energy's National Nuclear Security Administration under contract DE-NA0003525. The contributions on Recent developments in Lagrangian Particle Tracking as described in Sec. II include contributions from present and former colleagues as well as from guest scientists and external collaborators of the DLR Department of Experimental Methods (AS-EXV) which are kindly acknowledged: Philipp Godbersen, Matteo Novara, Sebastian Gesemann, Tobias Jahn, Hyungmin Shin, Reinhard Geisler, Johannes Bosbach, Ke Zhou (Penn State Uni), Sam Grauer (Penn State Uni) and Peter Manovski (Uni Melbourne). The contributions on Omnidirectional PIV as described in Sec. VII deals from work from a team of colleagues from TU Delft – Aerospace Engineering and NLR that is kindly acknowledged: Luuk Hendriksen, Adrian Grille Guerra, Andrea Sciacchitano, Constantin Jux and Ilda Hysa. Contributions of Markus Krebs, Christian Wolf, Alexander Heintz und Johannes Braukmann to the Experiments at DLR are highly appreciated. The lensless PIV research described in Sec. IV.A represents a collaborative effort. The authors gratefully acknowledge the significant contributions of Hogan Choi, Nicholas Antipa, and Chung-Sheng Yao to this work.

References

[1] Elsinga, G., Scarano, F., Wieneke, B., and van Oudheusden, B. W., "Tomographic particle image velocimetry," *Exp. Fluids*, Vol. 41, 2005. https://doi.org/10.1007/s00348-006-0212-z.

[2] Schanz, D., Gesemann, S., and Schröder, A., "Shake-The-Box: Lagrangian particle tracking at high particle image densities," *Exp. Fluids*, Vol. 57, 2016. https://doi.org/10.1007/s00348-016-2157-1.

[3] Schröder, A., and Schanz, D., "3D Lagrangian Particle Tracking in Fluid Mechanics," *Annual Review of Fluid Mechanics*, Vol. 55, No. Volume 55, 2023, 2023, pp. 511–540. https://doi.org/https://doi.org/10.1146/annurev-fluid-031822-041721, URL https://www.annualreviews.org/content/journals/10.1146/annurev-fluid-031822-041721.

[4] Nishino, K., Kasagi, N., and Hirata, M., "Three-Dimensional Particle Tracking Velocimetry Based on Automated Digital Image Processing," *Journal of Fluids Engineering*, Vol. 111, No. 4, 1989, pp. 384–391. https://doi.org/10.1115/1.3243657, URL https://doi.org/10.1115/1.3243657.

[5] Maas, H. G., Gruen, A., and Papantoniou, D., "Particle tracking velocimetry in three-dimensional flows," *Experiments in Fluids*, Vol. 15, No. 2, 1993, pp. 133–146. https://doi.org/10.1007/BF00190953, URL https://doi.org/10.1007/BF00190953.

[6] Barnkob, R., Kähler, C. J., and Rossi, M., "General defocusing particle tracking," *Lab on a Chip*, Vol. 15, No. 17, 2015, pp. 3556–3560. https://doi.org/10.1039/c5lc00562k.

[7] Longuet-Higgins, H. C., "A computer algorithm for reconstructing a scene from two projections," *Nature*, Vol. 293, 1981, pp. 133–135. URL https://api.semanticscholar.org/CorpusID:4327732.

[8] Hartley, R. I., and Sturm, P., "Triangulation," *Computer vision and image understanding*, Vol. 68, No. 2, 1997, pp. 146–157. URL https://www.sciencedirect.com/science/article/pii/S1077314297905476.

[9] Dabiri, D., and Pecora, C., *Particle Tracking Velocimetry*, IOP Publishing, 2019. URL https://iopscience.iop.org/book/mono/978-0-7503-2203-4.

[10] Elsinga, G. E., Scarano, F., Wieneke, B., and van Oudheusden, B. W., "Tomographic particle image velocimetry," *Experiments in Fluids*, Vol. 41, No. 6, 2006, pp. 933–947. https://doi.org/10.1007/s00348-006-0212-z, URL https://doi.org/10.1007/s00348-006-0212-z.

[11] Scarano, F., "Tomographic PIV: principles and practice," *Measurement Science and Technology*, Vol. 24, No. 1, 2012, p. 012001. https://doi.org/10.1088/0957-0233/24/1/012001, URL https://dx.doi.org/10.1088/0957-0233/24/1/012001.

[12] Herman, G. T., and Lent, A., "Iterative reconstruction algorithms," *Computers in Biology and Medicine*, Vol. 6, No. 4, 1976, pp. 273–294. https://doi.org/10.1016/0010-4825(76)90066-4, URL https://www.sciencedirect.com/science/article/pii/0010482576900664.

[13] Atkinson, C., and Soria, J., "An efficient simultaneous reconstruction technique for tomographic particle image velocimetry," *Experiments in Fluids*, Vol. 47, No. 4, 2009, pp. 553–568. https://doi.org/10.1007/s00348-009-0728-0, URL https://doi.org/10.1007/s00348-009-0728-0.

[14] Scarano, F., and Poelma, C., "Three-dimensional vorticity patterns of cylinder wakes," *Experiments in fluids*, Vol. 47, No. 1, 2009, pp. 69–83. https://doi.org/10.1007/s00348-009-0629-2.

[15] Schröder, A., Geisler, R., Staack, K., Elsinga, G. E., Scarano, F., Wieneke, B., Henning, A., Poelma, C., and Westerweel, J., "Eulerian and Lagrangian views of a turbulent boundary layer flow using time-resolved tomographic PIV," *Experiments in Fluids*, Vol. 50, No. 4, 2011, pp. 1071–1091. https://doi.org/10.1007/s00348-010-1014-x, URL https://doi.org/10.1007/s00348-010-1014-x.

[16] Wieneke, B., "Iterative reconstruction of volumetric particle distribution," *Measurement Science and Technology*, Vol. 24, No. 2, 2012, p. 024008. https://doi.org/10.1088/0957-0233/24/2/024008, URL https://dx.doi.org/10.1088/0957-0233/24/2/024008.

[17] Jahn, T., Schanz, D., and Schröder, A., "Advanced iterative particle reconstruction for Lagrangian particle tracking," *Experiments in Fluids*, Vol. 62, No. 8, 2021, p. 179. https://doi.org/10.1007/s00348-021-03276-7, URL https://doi.org/10.1007/s00348-021-03276-7.

[18] Schanz, D., Gesemann, S., and Schröder, A., "Shake-The-Box: Lagrangian particle tracking at high particle image densities," *Exp. Fluids*, Vol. 57, 2016. https://doi.org/10.1007/s00348-016-2157-1.

[19] Elsinga, G., Westerweel, J., Scarano, F., and Novara, M., "On the velocity of ghost particles and the bias errors in Tomographic-PIV," *Experiments in fluids*, Vol. 50, No. 4, 2011, pp. 825–838.

[20] Huhn, F., Schanz, D., Gesemann, S., Dierksheide, U., van de Meerendonk, R., and Schröder, A., "Large-scale volumetric flow measurement in a pure thermal plume by dense tracking of helium-filled soap bubbles," *Experiments in Fluids*, Vol. 58, No. 9, 2017, p. 116. https://doi.org/10.1007/s00348-017-2390-2, URL https://doi.org/10.1007/s00348-017-2390-2.

[21] Bosbach, J., Schanz, D., Godbersen, P., and Schröder, A., "Spatially and temporally resolved measurements of turbulent Rayleigh-Bénard convection by Lagrangian particle tracking of long-lived helium-filled soap bubbles," *14th International Symposium on Particle Image Velocimetry*, Vol. 1, No. 1, 2021. https://doi.org/10.18409/ispiv.v1i1.208, URL https://ispiv21.library.iit.edu/index.php/ISPIV/article/view/208.

[22] Weiss, S., Schanz, D., Erdogdu, A. O., Schröder, A., and Bosbach, J., "Investigation of turbulent superstructures in Rayleigh–Bénard convection by Lagrangian particle tracking of fluorescent microspheres," *Experiments in Fluids*, Vol. 64, No. 4, 2023, p. 82. https://doi.org/10.1007/s00348-023-03624-9, URL https://doi.org/10.1007/s00348-023-03624-9.

[23] Huhn, F., Schanz, D., Manovski, P., Gesemann, S., and Schröder, A., "Time-resolved large-scale volumetric pressure fields of an impinging jet from dense Lagrangian particle tracking," *Experiments in Fluids*, Vol. 59, No. 5, 2018, p. 81. https://doi.org/10.1007/s00348-018-2533-0, URL https://doi.org/10.1007/s00348-018-2533-0.

[24] Kim, M., Schanz, D., Novara, M., Godbersen, P., Yeom, E., and Schröder, A., "Experimental study on flow and turbulence characteristics of jet impinging on cylinder using three-dimensional Lagrangian particle tracking velocimetry," *Scientific Reports*, Vol. 13, No. 1, 2023, p. 10929. https://doi.org/10.1038/s41598-023-37970-9, URL https://www.nature.com/articles/s41598-023-37970-9.

[25] Schröder, A., Schanz, D., Bosbach, J., Novara, M., Geisler, R., Agocs, J., and Kohl, A., "Large-scale volumetric flow studies on transport of aerosol particles using a breathing human model with and without face protections," *Physics of Fluids*, Vol. 34, No. 3, 2022, p. 035133. https://doi.org/10.1063/5.0086383, URL https://doi.org/10.1063/5.0086383.

[26] Wolf, C. C., Schwarz, C., Kaufmann, K., Gardner, A. D., Michaelis, D., Bosbach, J., Schanz, D., and Schröder, A., "Experimental study of secondary vortex structures in a rotor wake," *Experiments in Fluids*, Vol. 60, No. 11, 2019, p. 175. https://doi.org/10.1007/s00348-019-2807-1, URL https://doi.org/10.1007/s00348-019-2807-1.

[27] Bross, M., Schanz, D., Novara, M., Eich, F., Schröder, A., and Kähler, C. J., "Turbulent superstructure statistics in a turbulent boundary layer with pressure gradients," *European Journal of Mechanics - B/Fluids*, Vol. 101, 2023, pp. 209–218. https://doi.org/10.1016/j.euromechflu.2023.05.010, URL https://www.sciencedirect.com/science/article/pii/S0997754623000778.

[28] Schröder, A., Schanz, D., Geisler, R., Godbersen, P., Agocs, J., and Simhan, A. R., "Near-wall flow features in ZPG-TBL at various Reynolds numbers usingdense 3D Lagrangian Particle Tracking," *21st Int. Symp on Appl. Laser Techniques to Fluid Mechanics*, Lisbon, Portugal, 2024.

[29] Godbersen, P., Bosbach, J., Schanz, D., and Schröder, A., "Beauty of turbulent convection: A particle tracking endeavor," *Physical Review Fluids*, Vol. 6, No. 11, 2021, p. 110509. https://doi.org/10.1103/PhysRevFluids.6.110509, URL https://link.aps.org/doi/10.1103/PhysRevFluids.6.110509.

[30] Bosbach, J., Kühn, M., and Wagner, C., "Large scale particle image velocimetry with helium filled soap bubbles," *Experiments in Fluids*, Vol. 46, No. 3, 2009, pp. 539–547. https://doi.org/10.1007/s00348-008-0579-0, URL https://doi.org/10.1007/s00348-008-0579-0.

[31] Scarano, F., Ghaemi, S., Caridi, G. C. A., Bosbach, J., Dierksheide, U., and Sciacchitano, A., "On the use of helium-filled soap bubbles for large-scale tomographic PIV in wind tunnel experiments," *Experiments in Fluids*, Vol. 56, No. 2, 2015, p. 42. https://doi.org/10.1007/s00348-015-1909-7, URL https://doi.org/10.1007/s00348-015-1909-7.

[32] Schröder, A., Schanz, D., Gesemann, S., Huhn, F., Garaboa-Paz, D., and Bodenschatz, E., "Measurements of the energy dissipation rate in homogeneous turbulence using dense 3D Lagrangian Particle Tracking and FlowFit," *Proceedings of the 20th International Symposium on the Application of Laser and Imaging Techniques to Fluid Mechanics*, 2022, pp. 2300–2319. https://doi.org/10.55037/lxlaser.20th.216.

[33] Schröder, A., Weiss, S., Schanz, D., Lemarechal, J., Bosbach, J., and Strübing, T., "Large scale 3D particle tracking for the study of airborne transmission of pathogens in realistic class room settings," *21st International Symposium on Flow Visualization ISFV 2025*, 2025, pp. 1–2.

[34] Schanz, D., Schröder, A., Bosbach, J., Strübing, T., Wolf, C. C., Schwarz, C., and Heintz, A., "Scanning Lagrangian Particle Tracking To Measure 3D Large Scale Aerodynamics Of Quadcopter Flight," *Proceedings of the International Symposium on the Application of Laser and Imaging Techniques to Fluid Mechanics*, Vol. 21, 2024, p. 15. https://doi.org/10.55037/lxlaser.21st.215.

[35] Wolf, C. C., Schanz, D., Schwarz, C., Heintz, A., Bosbach, J., Strübing, T., and Schröder, A., "Volumetric wake investigation of a free-flying quadcopter using Shake-The-Box Lagrangian particle tracking," *Experiments in Fluids*, Vol. 65, No. 10, 2024, p. 152. https://doi.org/10.1007/s00348-024-03880-3, URL https://doi.org/10.1007/s00348-024-03880-3.

[36] Schanz, D., Novara, M., Zanoun, E.-S., Egbers, C., and Schröder, A., "Large-scale measurements in turbulent pipe flow using 3D Lagrangian Particle Tracking," *15th International Symposium on Particle Image Velocimetry (ISPIV 2023)*, The California State University (ScholarWorks), 2023, pp. 1–2.

[37] Shin, H., and Schröder, A., "Robust Flow Field Reconstruction Using PINN for 3D Lagrangian Particle Tracking," *16th International Symposium on Particle Image Velocimetry – ISPIV 2025*, Tokio, Japan, 2025, pp. 1–12. URL https://www.ispiv2025.org/index.html.

[38] Kim, D., Schanz, D., Novara, M., Seo, H., Kim, Y., Schröder, A., and Kim, K. C., "Experimental study of turbulent bubbly jet. Part 1. Simultaneous measurement of three-dimensional velocity fields of bubbles and water," *Journal of Fluid Mechanics*, Vol. 941, 2022, p. A42. https://doi.org/10.1017/jfm.2022.301, URL https://www.cambridge.org/core/journals/journal-of-fluid-mechanics/article/experimental-study-of-turbulent-bubbly-jet-part-1-simultaneous-measurement-of-threedimensional-velocity-fields-of-bubbles-and-water/CE37CD2C44D7C5B5F141DED3CFEB8D32.

[39] Raffel, M., Willert, C. E., Scarano, F., Kähler, C. J., Wereley, S. T., and Kompenhans, J., "Particle image velocimetry: a practical guide, 3rd ed." *Particle image velocimetry: a practical guide, 3rd ed.*, edited by M. Raffel, C. E. Willert, F. Scarano, C. J. Kähler, S. T. Wereley, and J. Kompenhans, Springer International Publishing, Cham, 2018, pp. 285–307. https://doi.org/10.1007/978-3-319-68852-7_8, URL https://doi.org/10.1007/978-3-319-68852-7_8.

[40] Fuchs, T., Hain, R., and Kähler, C. J., "Double-frame 3D-PTV using a tomographic predictor," *Experiments in Fluids*, Vol. 57, No. 11, 2016, p. 174. https://doi.org/10.1007/s00348-016-2247-0, URL https://doi.org/10.1007/s00348-016-2247-0.

[41] Cornic, P., Leclaire, B., Champagnat, F., Le Besnerais, G., Cheminet, A., Illoul, C., and Losfeld, G., "Double-frame tomographic PTV at high seeding densities," *Experiments in Fluids*, Vol. 61, No. 2, 2020, p. 23. https://doi.org/10.1007/s00348-019-2859-2, URL https://doi.org/10.1007/s00348-019-2859-2.

[42] Novara, M., Schanz, D., and Schröder, A., "Two-Pulse 3D particle tracking with Shake-The-Box," *Experiments in Fluids*, Vol. 64, No. 5, 2023, p. 93. https://doi.org/10.1007/s00348-023-03634-7, URL https://doi.org/10.1007/s00348-023-03634-7.

[43] Kähler, C. J., Scharnowski, S., and Cierpka, C., "On the uncertainty of digital PIV and PTV near walls," *Experiments in Fluids*, Vol. 52, No. 6, 2012, pp. 1641–1656. https://doi.org/10.1007/s00348-012-1307-3, URL https://doi.org/10.1007/s00348-012-1307-3.

[44] Raiola, M., Lopez-Nuñez, E., Cafiero, G., and Discetti, S., "Adaptive ensemble PTV," *Measurement Science and Technology*, Vol. 31, No. 8, 2020, p. 085301. https://doi.org/10.1088/1361-6501/ab82bf, URL https://dx.doi.org/10.1088/1361-6501/ab82bf.

[45] Godbersen, P., and Schröder, A., "Functional binning: improving convergence of Eulerian statistics from Lagrangian particle tracking," *Measurement Science and Technology*, Vol. 31, No. 9, 2020, p. 095304. https://doi.org/10.1088/1361-6501/ab8b84, URL https://dx.doi.org/10.1088/1361-6501/ab8b84.

[46] Manovski, P., Novara, M., Depuru Mohan, N. K., Geisler, R., Schanz, D., Agocs, J., Godbersen, P., and Schröder, A., "3D Lagrangian particle tracking of a subsonic jet using multi-pulse Shake-The-Box," *Experimental Thermal and Fluid Science*, Vol. 123, 2021, p. 110346. https://doi.org/10.1016/j.expthermflusci.2020.110346, URL https://www.sciencedirect.com/science/article/pii/S089417772030844X.

[47] Bridges, J., and Wernet, M. P., "The NASA subsonic jet particle image velocimetry (PIV) dataset," Tech. rep., 2011.

[48] Novara, M., Schanz, D., Reuther, N., Kähler, C. J., and Schröder, A., "Lagrangian 3D particle tracking in high-speed flows: Shake-The-Box for multi-pulse systems," *Experiments in Fluids*, Vol. 57, No. 8, 2016, p. 128. https://doi.org/10.1007/s00348-016-2216-7, URL https://doi.org/10.1007/s00348-016-2216-7.

[49] Novara, M., Schanz, D., Geisler, R., Gesemann, S., Voss, C., and Schröder, A., "Multi-exposed recordings for 3D Lagrangian particle tracking with Multi-Pulse Shake-The-Box," *Experiments in Fluids*, Vol. 60, No. 3, 2019, p. 44. https://doi.org/10.1007/s00348-019-2692-7, URL https://doi.org/10.1007/s00348-019-2692-7.

[50] Sellappan, P., Alvi, F. S., and Cattafesta, L. N., "Lagrangian and Eulerian measurements in high-speed jets using Multi-Pulse Shake-The-Box and fine scale reconstruction (VIC#)," *Experiments in Fluids*, Vol. 61, No. 7, 2020, p. 157. https://doi.org/10.1007/s00348-020-02993-9, URL https://doi.org/10.1007/s00348-020-02993-9.

[51] Imaichi, K., and Ohmi, K., "Numerical processing of flow-visualization pictures – measurement of two-dimensional vortex flow," *Journal of Fluid Mechanics*, Vol. 129, 1983, p. 283–311. https://doi.org/10.1017/S0022112083000774.

[52] Agüí, J. C., and Jiménez, J., "On the performance of particle tracking," *Journal of Fluid Mechanics*, Vol. 185, 1987, pp. 447–468. URL https://www.cambridge.org/core/journals/journal-of-fluid-mechanics/article/abs/on-the-performance-of-particle-tracking/82D2BC8383289F0EF9430A14DA9C9288.

[53] He, C., Li, S., and Liu, Y., "Data assimilation: new impetus in experimental fluid dynamics," *Experiments in Fluids*, Vol. 66, No. 5, 2025, pp. 1–24. https://doi.org/10.1007/s00348-025-04020-1.

[54] Gesemann, S., Huhn, F., Schanz, D., and Schröder, A., "From Noisy Particle Tracks to Velocity, Acceleration and Pressure Fields using B-splines and Penalties," *18th International Symposium on Applications of Laser and Imaging Techniques to Fluid Mechanics*, Lisbon, Portugal, 2016, pp. 1–17. URL http://ltces.dem.ist.utl.pt/lxlaser/lxlaser2016/finalworks2016/papers/04.5_4_186paper.pdf.

[55] Godbersen, P., Gesemann, S., Schanz, D., and Schröder, A., "FlowFit3: Efficient Data Assimilation Of LPT Measurements," *Proceedings of the International Symposium on the Application of Laser and Imaging Techniques to Fluid Mechanics*, Vol. 21, 2024, pp. 1–14. https://doi.org/10.55037/lxlaser.21st.216, URL https://www.researchgate.net/profile/Andreas-Schroeder-9/publication/382155968_FlowFit3_Efficient_Data_Assimilation_Of_LPT_Measurements/links/66bf38fd145f4d35535f9d4c/FlowFit3-Efficient-Data-Assimilation-Of-LPT-Measurements.pdf.

[56] Schneiders, J. F. G., and Scarano, F., "Dense velocity reconstruction from tomographic PTV with material derivatives," *Experiments in Fluids*, Vol. 57, No. 9, 2016, p. 139. https://doi.org/10.1007/s00348-016-2225-6, URL https://doi.org/10.1007/s00348-016-2225-6.

[57] Jeon, Y. J., Müller, M., and Michaelis, D., "Fine scale reconstruction (VIC#) by implementing additional constraints and coarse-grid approximation into VIC+," *Experiments in Fluids*, Vol. 63, No. 4, 2022, p. 70. https://doi.org/10.1007/s00348-022-03422-9, URL https://doi.org/10.1007/s00348-022-03422-9.

[58] Raissi, M., Perdikaris, P., and Karniadakis, G. E., "Physics-informed neural networks: A deep learning framework for solving forward and inverse problems involving nonlinear partial differential equations," *Journal of Computational Physics*, Vol. 378, 2019, pp. 686–707. https://doi.org/10.1016/j.jcp.2018.10.045, URL https://www.sciencedirect.com/science/article/pii/S0021999118307125.

[59] "On the joint observability of flow fields and particle properties from Lagrangian trajectories: evidence from neural data assimilation," , Oct. 2025. https://doi.org/10.48550/arXiv.2510.00479, URL http://arxiv.org/abs/2510.00479, arXiv:2510.00479 [physics].

[60] Cai, S., Gray, C., and Karniadakis, G. E., "Physics-Informed Neural Networks Enhanced Particle Tracking Velocimetry: An Example for Turbulent Jet Flow," *IEEE Transactions on Instrumentation and Measurement*, Vol. 73, 2024, pp. 1–9. https://doi.org/10.1109/TIM.2024.3398068, URL https://ieeexplore.ieee.org/document/10522764.

[61] Barta, R., Volk, M.-C., Bauer, C., Wagner, C., and Mommert, M., "Temperature and pressure reconstruction in turbulent Rayleigh-B\'enard convection by Lagrangian velocities using PINN," *arXiv preprint arXiv:2505.02580*, 2025.

[62] Zhou, K., Grauer, S., Schanz, D., Godbersen, P., Schröder, A., Rockstroh, T., Jeon, Y., and Wieneke, B., "Benchmarking Data Assimilation Algorithms For 3D Lagrangian Particle Tracking," 2024. https://doi.org/10.55037/lxlaser.21st.229.

[63] Agüera, N., Cafiero, G., Astarita, T., and Discetti, S., "Ensemble 3D PTV for high resolution turbulent statistics," *Measurement Science and Technology*, Vol. 27, No. 12, 2016, p. 124011. https://doi.org/10.1088/0957-0233/27/12/124011, URL https://dx.doi.org/10.1088/0957-0233/27/12/124011.

[64] Mahowald, M., "VLSI analogs of neuronal visual processing: a synthesis of form and function," Ph.D. thesis, California Institute of Technology, Pasadena (CA), 1992. URL https://resolver.caltech.edu/CaltechCSTR:1992.cs-tr-92-15.

[65] Mead, C., "Neuromorphic Engineering: In Memory of Misha Mahowald," *Neural Computation*, Vol. 35, No. 3, 2023, pp. 343–383. https://doi.org/10.1162/neco_a_01553.

[66] Delbrück, T., Linares-Barranco, B., Culurciello, E., and Posch, C., "Activity-driven, event-based vision sensors," *Proceedings of 2010 IEEE International Symposium on Circuits and Systems*, 2010, pp. 2426–2429. https://doi.org/10.1109/ISCAS.2010.5537149.

[67] Lichtsteiner, P., Posch, C., and Delbruck, T., "A 128×128 120 dB 15 μs Latency Asynchronous Temporal Contrast Vision Sensor," *IEEE Journal of Solid-State Circuits*, Vol. 43, No. 2, 2008, pp. 566–576. https://doi.org/10.1109/JSSC.2007.914337.

[68] Finateu, T., Niwa, A., Matolin, D., Tsuchimoto, K., Mascheroni, A., Reynaud, E., Mostafalu, P., Brady, F., Chotard, L., LeGoff, F., Takahashi, H., Wakabayashi, H., Oike, Y., and Posch, C., "5.10 - A 1280×720 Back-Illuminated Stacked Temporal Contrast Event-Based Vision Sensor with 4.86 µm Pixels, 1.066GEPS Readout, Programmable Event-Rate Controller and Compressive Data-Formatting Pipeline," *2020 IEEE International Solid- State Circuits Conference - (ISSCC)*, 2020, pp. 112–114. https://doi.org/10.1109/ISSCC19947.2020.9063149.

[69] Gallego, G., Delbrück, T., Orchard, G., Bartolozzi, C., Taba, B., Censi, A., Leutenegger, S., Davison, A. J., Conradt, J., Daniilidis, K., and Scaramuzza, D., "Event-Based Vision: A Survey," *IEEE Transactions on Pattern Analysis and Machine Intelligence*, Vol. 44, No. 1, 2022, pp. 154–180. https://doi.org/10.1109/TPAMI.2020.3008413, URL https://arxiv.org/pdf/1904.08405.pdf.

[70] Chakravarthi, B., Verma, A. A., Daniilidis, K., Fermuller, C., and Yang, Y., "Recent Event Camera Innovations: A Survey," , 2024. URL https://arxiv.org/abs/2408.13627.

[71] Drazen, D., Lichtsteiner, P., Häfliger, P., Delbrück, T., and Jensen, A., "Toward real-time particle tracking using an event-based dynamic vision sensor," *Experiments in Fluids*, Vol. 51, 2011, pp. 1465–1469. https://doi.org/10.1007/s00348-011-1207-y.

[72] Borer, D., Delbruck, T., and Rösgen, T., "Three-dimensional particle tracking velocimetry using dynamic vision sensors," *Experiments in Fluids*, Vol. 58, 2017, p. 165. https://doi.org/10.1007/s00348-017-2452-5.

[73] Wang, Y., Idoughi, R., and Heidrich, W., "Stereo Event-Based Particle Tracking Velocimetry for 3D Fluid Flow Reconstruction," *Computer Vision - ECCV 2020*, edited by A. Vedaldi, H. Bischof, T. Brox, and J.-M. Frahm, Springer International Publishing, Cham, 2020, pp. 36–53. https://doi.org/10.1007/978-3-030-58526-6_3.

[74] Rusch, A., and Rösgen, T., "TrackAER: Real-time event-based quantitative flow visualization," *Experiments in Fluids*, Vol. 64, 2023, p. 136. https://doi.org/10.1007/s00348-023-03673-0.

[75] Willert, C., and Klinner, J., "Event-based imaging velocimetry: An assessment of event-based cameras for the measurement of fluid flows," *Experiments in Fluids*, Vol. 63, 2022, p. 101. https://doi.org/10.1007/s00348-022-03441-6.

[76] Willert, C., "Event-based imaging velocimetry using pulsed illumination," *Experiments in Fluids*, Vol. 64, 2023, p. 98. https://doi.org/10.1007/s00348-023-03641-8.

[77] Willert, C. E., and Franceschelli, L., "Real-time particle image velocimetry using event-based imaging," *16th International Symposium on Particle Image Velocimetry (ISPIV 2025)*, Tokyo (JP), 2025. URL https://elib.dlr.de/215850/.

[78] Cao, J., Zeng, X., Lyu, Z., Cai, W., Liu, H., and Liu, Y., "Benchmark evaluation of event-based imaging velocimetry using digital micro-mirror device," *Experiments in Fluids*, Vol. 66, No. 4, 2025, pp. 1–17. https://doi.org/10.1007/s00348-025-04003-2.

[79] Maya, L., Fan, L., Durocher, A., Savard, B., and Vena1, P., "An evaluation of event-based cameras for particle image velocimetry," *Experiments in Fluids*, Vol. 66, 2025, p. 204. https://doi.org/10.1007/s00348-025-04127-5.

[80] Schlatter, P., and Örlü, R., "Assessment of direct numerical simulation data of turbulent boundary layers," *Journal of Fluid Mechanics*, Vol. 659, 2010, pp. 116–126. https://doi.org/10.1017/S0022112010003113.

[81] Willert, C., "High-speed particle image velocimetry for the efficient measurement of turbulence statistics," *Experiments in Fluids*, Vol. 56, No. 1, 2015, 17. https://doi.org/10.1007/s00348-014-1892-4.

[82] Westerweel, J., Geelhoed, P., and Lindken, R., "Single-pixel resolution ensemble correlation for micro-PIV applications," *Experiments in fluids*, Vol. 37, No. 3, 2004, pp. 375–384. https://doi.org/10.1007/s00348-004-0826-y.

[83] Oldenziel, G., Sridharan, S., and Westerweel, J., "Measurement of high-Re turbulent pipe flow using single-pixel PIV," *Experiments in Fluids*, Vol. 64, 2023, p. 164. https://doi.org/10.1007/s00348-023-03701-z.

[84] Scharnowski, S., Hain, R., and Kähler, C., "Reynolds stress estimation up to single-pixel resolution using PIV-measurements," *Experiments in Fluids*, Vol. 52, 2012, pp. 985–1002. https://doi.org/10.1007/s00348-011-1184-1.

[85] Willert, C. E., and Klinner, J., "Dynamic wall shear stress measurement using event-based 3D particle tracking," *Experiments in Fluids*, Vol. 66, No. 2, 2025, p. 32. https://doi.org/10.1007/s00348-024-03946-2.

[86] Willert, C., "Event-based particle image velocimetry for high-speed flows," *Measurement Science and Technology*, Vol. 36, No. 7, 2025, p. 075302. https://doi.org/10.1088/1361-6501/ade27a.

[87] Willert, C. E., Franceschelli, L., Amico, E., Raiola, M., Cafiero, G., and Discetti, S., "Real-time event-based particle image velocimetry for active flow control," *Progress in Turbulence XI*, IOP, 2025. Accepted, to appear.

[88] Graca, R., Zhou, S., McReynolds, B., and Delbruck, T., "SciDVS: A Scientific Event Camera with 1.7% Temporal Contrast Sensitivity at 0.7 lux," 2024. https://doi.org/10.1109/ESSERC62670.2024.10719521.

[89] Graca, R., "A Scientific Event Camera: Theory, Design, and Measurements," Ph.D. thesis, Eidgenössische Hochschule Zürich, Zurich (CH), 2024. https://doi.org/10.3929/ethz-b-000683623.

[90] Antipa, N., Kuo, G., Heckel, R., Mildenhall, B., Bostan, E., Ng, R., and Waller, L., "DiffuserCam: lensless single-exposure 3D imaging," *Optica*, Vol. 5, No. 1, 2018, pp. 1–9.

[91] Boominathan, V., Robinson, J. T., Waller, L., and Veeraraghavan, A., "Recent advances in lensless imaging," *Optica*, Vol. 9, No. 1, 2022, pp. 1–16.

[92] Li, S., Gao, Y., Wu, J., Wang, M., Huang, Z., Chen, S., and Cao, L., "Lensless camera: Unraveling the breakthroughs and prospects," *Fundamental Research*, 2024.

[93] Lee, K. C., Bae, J., Baek, N., Jung, J., Park, W., and Lee, S. A., "Design and single-shot fabrication of lensless cameras with arbitrary point spread functions," *Optica*, Vol. 10, No. 1, 2023, pp. 72–80.

[94] Sinha, A., Lee, J., Li, S., and Barbastathis, G., "Lensless computational imaging through deep learning," *Optica*, Vol. 4, No. 9, 2017, pp. 1117–1125.

[95] Eppink, J., and Yao, C.-s., "Lensless particle image velocimetry," *Experiments in Fluids*, Vol. 65, No. 5, 2024, p. 73.

[96] Yanny, K., Monakhova, K., Shuai, R. W., and Waller, L., "Deep learning for fast spatially varying deconvolution," *Optica*, Vol. 9, No. 1, 2022, pp. 96–99.

[97] Cao, R., Divekar, N. S., Nunez, J. K., Upadhyayula, S., and Waller, L., "Neural space–time model for dynamic multi-shot imaging," *Nature Methods*, Vol. 21, No. 12, 2024, pp. 2336–2341.

[98] Adrian, R. J., "Particle-imaging techniques for experimental fluid mechanics," *Annual Review of Fluid Mechanics*, Vol. 23, No. 1, 1991, pp. 261–304. https://doi.org/10.1146/annurev.fl.23.010191.001401, URL https://doi.org/10.1146/annurev.fl.23.010191.001401.

[99] Bohren, C. F., and Huffman, D. R., "Absorption and Scattering by a Sphere," *Absorption and Scattering of Light by Small Particles*, John Wiley & Sons, Ltd, 1998, Chap. 4, pp. 82–129. https://doi.org/10.1002/9783527618156.ch4, URL https://doi.org/10.1002/9783527618156.ch4.

[100] Raffel, M., Braukmann, J. N., Willert, C. E., Giuseppini, L., and Wolf, C. C., "Feasibility Study of In-Line Particle Image Velocimetry," *Experiments in Fluids*, Vol. 65, No. 35, 2024, pp. 1–16. https://doi.org/10.1007/s00348-024-03766-4, URL https://link.springer.com/article/10.1007/s00348-024-03766-4.

[101] Schardin, H., "Die Schlierenverfahren und ihre Anwendungen," *Ergebnisse der exakten Naturwissenschaften*, Vol. 20, 1942, pp. 303–439.

[102] Settles, G. S., *Schlieren and Shadowgraph Techniques*, 1st ed., Springer, Berlin, Heidelberg, 2001. https://doi.org/10.1007/978-3-642-56640-0, URL https://doi.org/10.1007/978-3-642-56640-0.

[103] Raffel, M., Giuseppini, L., Braukmann, J. N., Wolf, C. C., and Willert, C. E., "Feasibility study of in-line PIV techniques for medium size observation areas," *AIAA Sitech (2024)*, AIAA, 2024, pp. 1–14.

[104] Page, W. E., Boyda, M. T., Fahringer, T. W., Weisberger, J. M., Bathel, B. F., Wernet, M., and Heineck, J. T., "Recent Progress and Development of Self-Aligned Focusing Schlieren," *AIAA SciTech 2025 Forum*, 2025. https://doi.org/10.2514/6.2025-1061, paper 1061.

[105] Willert, C. E., and Gharib, M., "Three-dimensional particle imaging with a single camera," *Experiments in Fluids*, Vol. 12, 1992, pp. 353–358. https://doi.org/10.1007/bf00193880.

[106] Beresh, S. J., "Time-Resolved Particle Image Velocimetry," *Measurement Science and Technology*, Vol. 32, No. 10, 2021, p. 102003. https://doi.org/10.1088/1361-6501/ac08c5.

[107] Klinner, J., Hergt, A., Grund, S., and Willert, C. E., "High-Speed PIV of Shock Boundary Layer Interactions in the Transonic Buffet Flow of a Compressor Cascade," *Experiments in Fluids*, Vol. 62, No. 3, 2021, p. 58. https://doi.org/10.1007/s00348-021-03145-3.

[108] Klinner, J., Munoz Lopez, E. J., Hergt, A., and Willert, C. E., "The Unsteady Shock-Boundary Layer Interaction in a Compressor Cascade—Part I: Measurements With Time-Resolved Particle Image Velocimetry," *ASME Journal of Turbomachinery*, Vol. 147, No. 9, 2025, p. 091001. https://doi.org/10.1115/1.4067467.

[109] Towne, A., Schmidt, O. T., and Colonius, T., "Spectral Proper Orthogonal Decomposition and its Relationship to Dynamic Mode Decomposition and Resolvent Analysis," *Journal of Fluid Mechanics*, Vol. 847, 2018, pp. 821–867. https://doi.org/10.1017/jfm.2018.283.

[110] Schmidt, O. T., and Colonius, T., "Guide to Spectral Proper Orthogonal Decomposition," *AIAA Journal*, Vol. 58, No. 3, 2020, pp. 1023–1033. https://doi.org/10.2514/1.j058809.

[111] Thurow, B., Jiang, N., and Lempert, W., "Review of Ultra-High Repetition Rate Laser Diagnostics for Fluid Dynamic Measurements," *Measurement Science and Technology*, Vol. 24, No. 1, 2013, p. 012002.

[112] Slipchenko, M. N., Meyer, T. R., and Roy, S., "Advances in Burst-Mode Laser Diagnostics for Reacting and Nonreacting Flows," *Proceedings of the Combustion Institute*, Vol. 38, No. 1, 2021, pp. 1533–1560. https://doi.org/10.1016/j.proci.2020.07.024.

[113] Beresh, S. J., Wagner, J. L., Casper, K. M., DeMauro, E. P., Henfling, J. F., and Spillers, R. W., "Spatial Distribution of Resonance in the Velocity Field for Transonic Flow over a Rectangular Cavity," *AIAA Journal*, Vol. 55, No. 12, 2017, pp. 4203–4218. https://doi.org/10.2514/1.j056106.

[114] Beresh, S., Kearney, S., Wagner, J., Guildenbecher, D., Henfling, J., Spillers, R., Pruett, B., Jiang, N., Slipchenko, M., Mance, J., and Roy, S., "Pulse-Burst PIV in a High-Speed Wind Tunnel," *Measurement Science and Technology*, Vol. 26, No. 9, 2015, p. 095305. https://doi.org/10.1088/0957-0233/26/9/095305.

[115] Wagner, J. L., Beresh, S. J., Casper, K. M., DeMauro, E. P., and Arunajatesan, S., "Resonance Dynamics in Compressible Cavity Flows using Time-Resolved Velocity and Surface Pressure Fields," *Journal of Fluid Mechanics*, Vol. 830, 2017, pp. 494–527. https://doi.org/10.1017/jfm.2017.606.

[116] Beresh, S. J., Henfling, J. F., and Spillers, R. W., "Time-Resolved Planar Velocimetry of the Supersonic Wake of a Wall-Mounted Hemisphere," *AIAA Journal*, Vol. 57, No. 4, 2019, pp. 1383–1399. https://doi.org/10.2514/1.j057814.

[117] Vanstone, L., and Clemens, N. T., "Unsteadiness Mechanisms of a Swept Compression-Ramp Shock / Boundary Layer Interaction at Mach 2," *AIAA SciTech Forum*, AIAA, 2019. https://doi.org/10.2514/6.2019-0095, aIAA Paper 2019-0095.

[118] Vanstone, L., and Clemens, N. T., "Proper Orthogonal Decomposition Analysis of Swept-Ramp Shock-Wave/Boundary-Layer Unsteadiness at Mach 2," *AIAA Journal*, Vol. 57, No. 8, 2019, pp. 3395–3409. https://doi.org/10.2514/1.j057874.

[119] Journell, C. L., Gejji, R. M., Walters, I. V., Lemcherfi, A. I., Slabaugh, C. D., and Stout, J. B., "High-Speed Diagnostics in a Natural Gas-Air Rotating Detonation Engine," *Journal of Propulsion and Power*, Vol. 36, No. 4, 2020, pp. 498–507. https://doi.org/10.2514/1.b37740.

[120] Gomez, M., Lauriola, D. K., Slipchenko, M. N., Roy, S., Son, S. F., and Meyer, T. R., "Spatiotemporally Resolved 5-MHz Visualization and Particle Image Velocimetry in Early Time Multiphase Blasts," *Optics and Lasers in Engineering*, Vol. 161, 2023, p. 107351. https://doi.org/10.1016/j.optlaseng.2022.107351.

[121] Wagner, J. L., DeMauro, E. P., Casper, K. M., Beresh, S. J., Lynch, K. P., and Pruett, B. O., "Pulse-Burst PIV of an Impulsively Started Cylinder in a Shock Tube for Re > 10^5," *Experiments in Fluids*, Vol. 59, No. 6, 2018, p. 106.

[122] DeMauro, E. P., Wagner, J. L., Beresh, S. J., and Farias, P. A., "Unsteady Drag Following Shock Wave Impingement on a Dense Particle Curtain Measured using Pulse-Burst PIV," *Physical Review Fluids*, Vol. 2, No. 6, 2017, p. 064301. https://doi.org/10.1103/physrevfluids.2.064301.

[123] Carter, J., Pathikonda, G., Jiang, N., Felver, J. F., Roy, S., and Ranjan, D., "Time-Resolved Measurements of Turbulent Mixing in Shock-Driven Variable-Density Flows," *Scientific Reports*, Vol. 9, 2019, p. 20315. https://doi.org/10.1038/s41598-019-56736-w.

[124] Pathikonda, G., Petter, S. J., Wall, I. E., and Ranjan, D., "Temporal Evolution of Scalar Modes in Richtmyer–Meshkov Instability of Inclined Interface using High-Speed PIV and PLIF Measurements at 60 kHz," *Measurement Science and Technology*, Vol. 33, No. 10, 2022, p. 105206. https://doi.org/10.1088/1361-6501/ac7ccb.

[125] Beresh, S. J., Henfling, J. F., Spillers, R. W., and Spitzer, S. M., "'Postage-Stamp PIV': Small Velocity Fields at 400 kHz for Turbulence Spectra Measurements," *Measurement Science and Technology*, Vol. 29, No. 3, 2018, p. 034011. https://doi.org/10.1088/1361-6501/aa9f79.

[126] Beresh, S. J., Spillers, R. W., Soehnel, M. M., and Spitzer, S. M., "Extending the Frequency Limits of 'Postage-Stamp PIV' to MHz Rates," *AIAA SciTech Forum*, AIAA, 2020. https://doi.org/10.2514/6.2020-1018, aIAA Paper 2020-1018.

[127] Beresh, S. J., Neal, D. R., and Sciacchitano, A., "Validation of Multi-Frame PIV Image Interrogation Algorithms in the Spectral Domain," *AIAA SciTech Forum*, AIAA, 2021. https://doi.org/10.2514/6.2021-0019, aIAA Paper 2021-19.

[128] Manovski, P., Rowin, W. A., Ng, H., Gulotta, P., Giacobello, M., de Silva, C., Hutchings, N., and Marusic, I., "The Spectral Response of Time-Resolved PIV in a Turbulent Boundary Layer," *Experiments in Fluids*, Vol. 66, No. 7, 2025, p. 134. https://doi.org/10.21203/rs.3.rs-5698396/v1.

[129] Willert, C. E., "'Profile PIV' – More than Just an Optical Hotwire, New Potentials of PIV in Boundary Layer Research," *18th International Symposium on Flow Visualization*, Zurich, Switzerland, 2018.

[130] Geschwindner, C., Westrup, K., Dreizler, A., and Böhm, B., "Ultra-High-Speed Time-Resolved PIV of Turbulent Flows using a Continuously Pulsing Fiber Laser," *Experiments in Fluids*, Vol. 63, No. 4, 2022, p. 75. https://doi.org/10.1007/s00348-022-03424-7.

[131] Samimy, M., and Wernet, M. P., "Review of Planar Multiple-Component Velocimetry in High-Speed Flows," *AIAA Journal*, Vol. 38, No. 4, 2000, pp. 553–574. https://doi.org/10.2514/3.14446.

[132] Scarano, F., "Overview of PIV in Supersonic Flows," *Particle Image Velocimetry, Topics in Applied Physics*, Vol. 112, Springer, Berlin, Heidelberg, 2007. https://doi.org/10.1007/978-3-540-73528-1_24.

[133] Danehy, P. M., Weisberger, J., Johansen, C., Reese, D., Fahringer, T., Parziale, N., Dedic, C., Estevadeordal, J., and Cruden, B., "Non-Intrusive Measurement Techniques for Flow Characterization of Hypersonic Wind Tunnels," *NATO Meeting STO-VKI-LS on Flow Characterization and Modeling of Hypersonic Wind Tunnels*, Sint-Genesius-Rode, Belgium, 2018.

[134] Raffel, M., Willert, C., Scarano, F., Kähler, C. J., Wereley, S., and Kompenhans, J., *Particle Image Velocimetry: A Practical Guide*, Springer, 2018. https://doi.org/10.1007/978-3-319-68852-7.

[135] Smith, B., and Neal, D., "Particle Image Velocimetry," *Handbook of Fluid Dynamics, 2nd ed.*, edited by R. W. Johnson, CRC Press, 2016, pp. 48–1. https://doi.org/10.1201/b19031-55.

[136] Samimy, M., and Lele, S., "Motion of Particles with Inertia in a Compressible Free Shear Layer," *Physics of Fluids A*, Vol. 3, No. 8, 1991, pp. 1915–1923. https://doi.org/10.1063/1.857921.

[137] Melling, A., "Tracer Particles and Seeding for Particle Image Velocimetry," *Measurement Science and Technology*, Vol. 8, No. 12, 1997, pp. 1406–1416. https://doi.org/10.1088/0957-0233/8/12/005.

[138] Ragni, D., Schrijer, F., van Oudheusden, B., and Scarano, F., "Particle Tracer Response across Shocks Measured by PIV," *Experiments in Fluids*, Vol. 50, No. 1, 2011, pp. 53–64.

[139] Williams, O., Nguyen, T., Schreyer, A., and Smits, A., "Particle Response Analysis for Particle Image Velocimetry in Supersonic Flows," *Physics of Fluids*, Vol. 27, No. 7, 2015, p. 076101. https://doi.org/10.1063/1.4922865.

[140] Kähler, C., Sammler, B., and Kompenhans, J., "Generation and Control of Tracer Particle for Optical Flow Investigation in Air," *Experiments in Fluids*, Vol. 33, No. 6, 2002, pp. 736–742. https://doi.org/10.1007/978-3-642-18795-7_30.

[141] Casper, M., Stephan, S., Scholz, P., and Radespiel, R., "Qualification of Oil-Based Tracer Particles for Heated Ludwieg Tubes," *Experiments in Fluids*, Vol. 55, No. 6, 2014, p. 1753. https://doi.org/10.1007/s00348-014-1753-1.

[142] Ghaemi, S., Schmidt-Ott, A., and Scarano, F., "Nanostructured Tracers for Laser-Based Diagnostics in High-Speed Flows," *Measurement Science and Technology*, Vol. 21, No. 10, 2010, p. 105403. https://doi.org/10.1088/0957-0233/21/10/105403.

[143] Zhao, Y., Yi, S., Tian, L., and Cheng, Z., "Supersonic Flow Imaging via Nanoparticles," *Science in China Series E: Technological Sciences*, Vol. 52, 2009, pp. 3640–3648. https://doi.org/10.1007/s11431-009-0281-3.

[144] Chen, F., Liu, H., Yang, Z., and Hu, H., "Tracking Characteristics of Tracer Particles for PIV Measurements in Supersonic Flows," *Chinese Journal of Aeronautics*, Vol. 30, No. 2, 2017, pp. 577–585. https://doi.org/10.1016/j.cja.2016.12.033.

[145] Zhu, Y., Zhang, C., Chen, X., Yuan, H., Wu, J., Chen, S., Lee, C., and Gad-el Hak, M., "Transition in Hypersonic Boundary Layers: Role of Dilatational Waves," *AIAA Journal*, Vol. 54, No. 10, 2016, pp. 3039–3049. https://doi.org/10.2514/1.j054702.

[146] Ding, H., Yi, S., Ouyang, T., and Zhao, Y., "Research on Velocity Measurements of the Hypersonic Turbulent Boundary Layer Based on the Nano-Tracer-Based Planar Laser Scattering Technique," *Measurement Science and Technology*, Vol. 31, No. 8, 2020, p. 085302. https://doi.org/10.1088/1361-6501/ab7f77.

[147] Zhu, Y., Zhu, W., Gu, D., Lee, C., and Smith, C., "Transitional Flow Structures in Heated Hypersonic Boundary Layers," *Physics of Fluids*, Vol. 34, No. 5, 2022, p. 054144. https://doi.org/10.1063/5.0091192.

[148] Humphreys, W. J., Rallo, R., Hunter, W. J., Bartram, S., and Blackshire, J., "Application of Particle Image Velocimetry to Mach 6 Flows," *5th International Conference of Laser Anemometry, Advances and Applications*, Veldhoven, The Netherlands, 1993.

[149] Havermann, M., Haertig, J., Rey, C., and George, A., "Application of Particle Image Velocimetry to High-Speed Supersonic Flows in a Shock Tunnel," *11th International Symposium on Applications of Laser Techniques to Fluid Mechanics*, Lisbon, Portugal, 2002.

[150] Schrijer, F., Scarano, F., and van Oudheusden, B., "Application of PIV in a Mach 7 Double-Ramp Flow," *Experiments in Fluids*, Vol. 41, No. 2, 2006, pp. 353–363. https://doi.org/10.1007/s00348-006-0140-y.

[151] Kirmse, T., Agocs, J., Schröder, A., Martinez Schramm, J., Karl, S., and Hannemann, K., "Application of Particle Image Velocimetry and the Background-Oriented Schlieren Technique in the High-Enthalpy Shock Tunnel Göttingen," *Shock Waves*, Vol. 21, No. 3, 2011, pp. 233–241. https://doi.org/10.1007/s00193-011-0314-2.

[152] Sahoo, D., Ringuette, M., and Smits, A., "Experimental Investigation of a Hypersonic Turbulent Boundary Layer," *AIAA Paper 2009-780*, 2009. https://doi.org/10.2514/6.2009-780.

[153] Williams, O., Sahoo, D., Baumgartner, M., and Smits, A., "Experiments on the Structure and Scaling of Hypersonic Turbulent Boundary Layers," *Journal of Fluid Mechanics*, Vol. 834, 2018, pp. 237–270.

[154] Schreyer, A., Sahoo, D., Williams, O., and Smits, A., "Experimental Investigation of Two Hypersonic Shock/Turbulent Boundary-Layer Interactions," *AIAA Journal*, Vol. 56, No. 12, 2018, pp. 4830–4844. https://doi.org/10.2514/1.j057342.

[155] Neeb, D., Saile, D., and Gülhan, A., "Experiments on a Smooth Wall Hypersonic Boundary Layer at Mach 6," *Experiments in Fluids*, Vol. 59, No. 4, 2018, p. 68. https://doi.org/10.1007/s00348-018-2518-z.

[156] Tuttle, S., Carter, C., and Hsu, K., "Particle Image Velocimetry in a Nonreacting and Reacting High-Speed Cavity," *Journal of Propulsion and Power*, Vol. 30, No. 3, 2014, pp. 576–591. https://doi.org/10.2514/1.b34974.

[157] Rice, B., Goyne, C., and McDaniel, J., "Seeding Bias in Particle Image Velocimetry Applied to Dual-Mode Scramjet," *Journal of Propulsion and Power*, Vol. 31, No. 5, 2015, pp. 1393–1403. https://doi.org/10.2514/1.b35443.

[158] Bauknecht, A., Merz, C., Raffel, M., Landolt, A., and Meier, A., "Blade-tip Vortex Detection in Maneuvering Flight using the Background-Oriented Schlieren Technique," *Journal of Aircraft*, Vol. 51, No. 6, 2014, pp. 2005–2014. https://doi.org/10.2514/1.C032672.

[159] Raffel, M., "Background-Oriented Schlieren (BOS) Techniques," *Experiments in Fluids*, Vol. 56, No. 3, 2015, p. 60. https://doi.org/10.1007/s00348-015-1927-5.

[160] Danehy, P., Burns, R., Reese, D., Retter, J., and Kearney, S., "FLEET Velocimetry for Aerodynamics," *Annual Review of Fluid Mechanics*, Vol. 54, 2022, pp. 525–553. https://doi.org/10.1146/annurev-fluid-032321-025544.

[161] Dogariu, L., Dogariu, A., Miles, R., Smith, M., and Marineau, E., "Femtosecond Laser Electronic Excitation Tagging Velocimetry in a Large-Scale Hypersonic Facility," *AIAA Journal*, Vol. 57, No. 11, 2019, pp. 4725–4737. https://doi.org/10.2514/1.j057759.

[162] Dogariu, A., Dogariu, L., Smith, M., MacManamen, B., Lafferty, J., and Miles, R., "Velocity and Temperature Measurements in Mach 18 Nitrogen Flow at Tunnel 9," *AIAA Paper 2021-0020*, 2021. https://doi.org/10.2514/6.2021-0020.

[163] Senior, W., Pehrson, J., Bhakta, R., de Zetter, M., Spillers, R., Beresh, S., and Richardson, D., "FLEET Velocimetry of Hypersonic Flow Separation," *AIAA Science and Technology Forum*, 2026. To be presented.

[164] Parziale, N., Smith, M., and Marineau, E., "Krypton Tagging Velocimetry of an Underexpanded Jet," *Applied Optics*, Vol. 54, No. 16, 2015, pp. 5094–5101. https://doi.org/10.1364/ao.54.005094.

[165] Mustafa, M., Parziale, N., Smith, M., and Marineau, E., "Nonintrusive Freestream Velocity Measurement in a Large-Scale Hypersonic Wind Tunnel," *AIAA Journal*, Vol. 55, No. 10, 2017, pp. 3611–3616. https://doi.org/10.2514/1.j056177.

[166] Jiang, N., Hsu, P., Grib, S., Slipchenko, M., Shekhtman, D., Parziale, N., Smith, M., Spicer, A., and Roy, S., "Mach 18 Flow Velocimetry with 100-kHz KTV and PLEET in AEDC Tunnel 9," *Applied Optics*, Vol. 62, No. 6, 2023, pp. A25–A30. https://doi.org/10.1364/ao.477203.

[167] Jans, E., Lynch, K., Daniel, K., and Kearney, S., "Nitric Oxide Molecular Tagging Velocimetry of a Free-Flight Model in a Reflected Shock Tunnel," *Optics Letters*, Vol. 50, No. 6, 2025, pp. 1839–1842. https://doi.org/10.1364/ol.557444.

[168] Leonov, B., Moran, A., North, S., and Miles, R., "Burst-Mode Velocimetry of Hypersonic Flow by Nitric Oxide Ionization Induced Flow Tagging and Imaging," *Optics Letters*, Vol. 49, No. 3, 2024, pp. 426–429. https://doi.org/10.1364/ol.503786.

[169] Arroyo, P., and Greated, C. A., "Stereoscopic particle image velocimetry," *Measurement Science and Technology*, Vol. 2, 1991, p. 1181. https://doi.org/10.1088/0957-0233/2/12/012.

[170] Nakagawa, M., Kallweit, S., Michaux, F., and Hojo, T., "Typical Velocity Fields and Vortical Structures around a Formula One Car, based on Experimental Investigations using Particle Image Velocimetry," *SAE International Journal of Passenger Cars - Mechanical Systems*, Vol. 9, No. 2, 2016, p. 754–771. https://doi.org/10.4271/2016-01-1611.

[171] Elsinga, G. E., Scarano, F., Wieneke, B., and Van Oudheusden, B. W., "Tomographic particle image velocimetry," *Experiments in Fluids*, Vol. 41, No. 6, 2006, p. 933–947. https://doi.org/10.1007/s00348-006-0212-z.

[172] Bosbach, J., Kühn, M., and Wagner, C., "Large scale particle image velocimetry with helium filled soap bubbles," *Experiments in Fluids*, Vol. 46, No. 3, 2009, p. 539–547. https://doi.org/10.1007/s00348-008-0579-0.

[173] Wieneke, B., "Iterative reconstruction of volumetric particle distribution," *Measurement Science and Technology*, Vol. 24, No. 2, 2013. https://doi.org/10.1088/0957-0233/24/2/024008.

[174] Schanz, D., Gesemann, S., and Schröder, A., "Shake-The-Box: Lagrangian particle tracking at high particle image densities," *Experiments in Fluids*, Vol. 57, No. 5, 2016. https://doi.org/10.1007/s00348-016-2157-1.

[175] Hysa, I., Tuinstra, M., Sciacchitano, A., and Scarano, F., "A multi-directional redundant 3D-PIV system for ship deck wind interactions," Tech. rep., 2023.

[176] Schneiders, J. F. G., Scarano, F., Jux, C., and Sciacchitano, A., "Coaxial volumetric velocimetry," *Measurement Science and Technology*, Vol. 29, No. 6, 2018. https://doi.org/10.1088/1361-6501/aab07d.

[177] Jux, C., Sciacchitano, A., Schneiders, J. F. G., and Scarano, F., "Robotic volumetric PIV of a full-scale cyclist," *Experiments in Fluids*, Vol. 59, No. 4, 2018. https://doi.org/10.1007/s00348-018-2524-1.

[178] Wieneke, B., and Rockstroh, T., "Lagrangian particle tracking in the presence of obstructing objects," *Measurement Science and Technology*, 2024. https://doi.org/10.1088/1361-6501/ad289d.

[179] Hendriksen, L. A., Sciacchitano, A., and Scarano, F., "Object registration techniques for 3D particle tracking," *Measurement Science and Technology*, Vol. 35, No. 12, 2024. https://doi.org/10.1088/1361-6501/ad715c.

[180] Elsinga, G. E., Westerweel, J., Scarano, F., and Novara, M., "On the velocity of ghost particles and the bias errors in Tomographic-PIV," *Experiments in Fluids*, Vol. 50, No. 4, 2011, p. 825–838. https://doi.org/10.1007/s00348-010-0930-0.

[181] Novara, M., Schanz, D., and Schröder, A., "Two-Pulse 3D particle tracking with Shake-The-Box," *Experiments in Fluids*, Vol. 64, No. 5, 2023. https://doi.org/10.1007/s00348-023-03634-7.

[182] Dawson-Howe, K. M., and Vernon, D., "Simple Pinhole Camera Calibration," Tech. rep., 1994.

[183] Terra, W., Brown, C., Vloemans, S., van der Waals, M., Sciacchitano, A., Burton, D., Thompson, M. C., and Huysmans, T., "A Generic Cyclist Model for aerodynamic investigation: Design, geometry & first aerodynamic analysis of a male time-trial and sprint model," *Journal of Wind Engineering and Industrial Aerodynamics*, Vol. 252, 2024. https://doi.org/10.1016/j.jweia.2024.105829.

[184] Agüera, N., Cafiero, G., Astarita, T., and Discetti, S., "Ensemble 3D PTV for high resolution turbulent statistics," *Measurement Science and Technology*, Vol. 27, No. 12, 2016. https://doi.org/10.1088/0957-0233/27/12/124011.